eman ta zabal zazu

Universidad del País Vasco
Euskal Herriko Unibertsitatea

EARLY-STAGE DETECTION OF MEMBRANE FOULING

ILIANE RAFANIELLO ALONSO

2022

Para ti Abuelo,

que siempre estuviste y seguirás estando.

Gracias por haber sido un ejemplo inmejorable

de fortaleza, disciplina, optimismo y amor.

TABLE OF CONTENTS

RESUMEN

Actualmente uno de los mayores retos a los que nuestra sociedad se enfrenta es la creciente escasez de agua. De acuerdo con estudios recientes, a día de hoy dos tercios de la población mundial vive en condiciones de escasez de agua al menos durante un mes al año. Además, la cantidad de agua potable disponible en el planeta está fuertemente limitada y distribuida muy irregularmente. Por lo tanto, es fundamental producir agua potable donde se necesita de forma eficiente mediante tecnologías de desalinización. El proceso de desalación más utilizado en todo el mundo es la ósmosis inversa (OI). Aunque la OI es un proceso eficiente y de gran capacidad de producción y bajo coste en comparación con la desalinización térmica, uno de los mayores problemas aún sin resolver es el ensuciamiento de membranas o "fouling". El "fouling" sucede cuando los compuestos presentes en el agua a tratar interaccionan con la superficie de la membrana y se adsorben de forma irreversible. En consecuencia, el flujo de agua limpia filtrada disminuye considerablemente y la eficiencia del proceso de filtración se ve fuertemente afectada.

Aunque el “fouling” no se puede evitar por completo, por un lado, se intenta disminuir la adsorción de moléculas mediante modificaciones químicas en la superficie de las membranas. Sin embargo, esta estrategia a menudo se basa en un enfoque de prueba y error. Por lo tanto, es importante utilizar técnicas que permitan caracterizar las interacciones entre las membranas modificadas y los compuestos ensuciantes a fin de tener una comprensión sistemática y mejorada de los fenómenos que subyacen al ensuciamiento de membranas.

Por otro lado, en las plantas de desalinización donde el “fouling” es problemático, la atención se centra en optimizar los intervalos de limpieza de la membrana para prolongar la vida útil de la misma y reducir los tiempos de inactividad del proceso y los costes de limpieza. Las entrevistas realizadas con algunas de las principales empresas desaladoras españolas que operan en todo el mundo revelaron que hasta el momento, los operadores carecen de un método lo suficientemente sensible para detectar el ensuciamiento de la membrana en una etapa temprana que evitaría tener caídas significativas en el flujo de agua y permitiría optimizar las condiciones operativas del proceso, como los protocolos de limpieza. Se han propuesto varios métodos para la detección del ensuciamiento de membranas, pero hasta el momento ninguno ha demostrado ser lo suficientemente sensible para detectarlo de forma anticipada y poder actuar en consecuencia.

El objetivo de este trabajo es por lo tanto investigar si las limitaciones de los métodos convencionales se pueden superar por

combinar dos técnicas sensibles a fenómenos de superficie: la microbalanza de cristal de cuarzo con monitorización de la disipación (QCM-D) y la resonancia de plasmones superficiales multi-paramétrica (MP-SPR).

Se realizaron estudios de monitorización en tiempo real de la adsorción de diferentes ensuciantes en distintos filmes de poliamida y los datos obtenidos se correlacionaron con un sistema independiente de filtración a fin de probar la viabilidad y la complementariedad de las dos técnicas (Capítulos 3 y 4). Se pudo demostrar con éxito que la combinación QCM-D/MP-SPR permite caracterizar la acumulación de incluso las primeras capas de "fouling" a nivel nanométrico y por lo tanto, posee una sensibilidad lo suficientemente grande como para anticipar la necesidad de limpiar las membranas antes de que el flujo de agua del permeado disminuya.

Los métodos además permitieron testar diferentes estrategias de limpieza de membranas de forma eficiente tanto en términos de tiempo como de material (Capítulo 5) confirmando que esta combinación de técnicas puede ser una herramienta muy poderosa para realizar un barrido rápido de la eficiencia de los protocolos de limpieza. Posteriormente, y como estudio de validación en un entorno industrialmente relevante, se implementó un dispositivo de monitorización basado en el QCM-D en una planta desaladora industrial a escala piloto. Los resultados se presentan en el Capítulo 6, donde se analiza críticamente el potencial del nuevo dispositivo para aumentar la eficiencia del proceso y mitigar el ensuciamiento de la membrana.

Finalmente, el Capítulo 7 proporciona una hoja de ruta hacia el mercado para el dispositivo de monitorización basado en QCM-D/MP-SPR que incluye comentarios de los operadores de plantas de desalinización sobre los requisitos del sistema y las oportunidades de mercado.

ABSTRACT

Nowadays one of the biggest challenges that our society faces is the increasing water scarcity. In accordance with recent studies, today two thirds of global population live under water scarcity conditions for at least one month per year. In addition, the amount of available freshwater in the world is strongly limited and distributed very irregularly. Therefore, drinking water needs to be produced by desalination technologies in an efficient way where needed. The most applied desalination process worldwide is reverse osmosis (RO). Although RO is an efficient process which a large production capacity and low cost compared to thermal desalination processes, one of the biggest problems still unresolved is membrane fouling. Fouling occurs when compounds present in the water to be treated interact with the membrane surface and adsorb in an irreversible way. Consequently, the filtered clean water flux decreases considerably and process efficiency is strongly affected.

Although fouling cannot be avoided completely, attempts are being made on one hand to modify the membrane surface chemically in order to minimize adsorption of molecules. However, this strategy is often based on a trial-and-error approach. Therefore, it is important to use techniques that allow characterizing interactions between modified membranes and foulants such as to have a better and systematic understanding of the phenomena that underlie fouling.

On the other hand, in desalination plants suffering from fouling the focus lies on optimizing membrane cleaning intervals in order to lengthen membrane lifetime and reducing process downtimes and cleaning-costs. Interviews with some of the major Spanish desalination companies operating worldwide revealed that until today operators lack a method sufficiently sensitive for detecting membrane fouling at an early-stage which would avoid significant drops in water flux and permit optimizing process operating conditions such as membrane cleaning protocols. Several methods have been proposed for membrane fouling detection but until today none has proven to be sensitive enough to handle membrane fouling in an anticipative way.

The aim of this work was therefore to investigate whether the limitations of conventional methods can be overcome by combining two advanced surface-sensitive techniques: quartz crystal microbalance with dissipation monitoring (QCM-D) and multi-parameter surface plasmon resonance (MP-SPR).

Real-time monitoring of adsorption of different foulants on different polyamide (PA) films was studied and correlated with an independent filtration system in order to prove the feasibility and complementarity of both techniques (Chapter 3 and 4). It could successfully be demonstrated that QCM-D/MP-SPR enables characterizing the build-up of even the very first fouling layers at the nanoscale and therefore possessed a sensitivity high enough such as to anticipate the need of membrane cleaning before the water permeate flux decreased.

QCM-D/MP-SPR furthermore allowed to test different membrane cleaning strategies in a time-efficient and material-extensive manner (Chapter 5) confirming that the combination of both methods could be a powerful tool for a fast screening of membrane cleaning protocols. Subsequently, and as a validation study in an industrially relevant environment, a QCM-D based monitoring device was implemented in an industrial pilot-scale desalination plant. The results are presented in Chapter 6 where the potential of the new device to increase the process efficiency and mitigate membrane fouling is critically discussed. Finally, Chapter 7 provides a roadmap to the market for the QCM-D/MP-SPR-based monitoring device including feedback from desalination plant operators on system requirements, and market opportunities.

CHAPTER 1

INTRODUCTION

1.1. Desalination for drinking water production

Water is an essential element for human welfare and development. Water scarcity is therefore nowadays one of the biggest challenges that our society faces. Water scarcity may be interpreted in two different terms: economic water scarcity and physical water scarcity. Economic water scarcity occurs in countries where there is insufficient water infrastructure to ensure water access and it is commonly present in countries of Africa and some regions of South America and South Asia [1]. Those countries suffering from economic water scarcity strongly need external investment to develop technologies that could grant people access to water. On the other hand, physical water scarcity exists in arid regions or where the water withdrawal is very high. The degree of water withdrawal related to water resources, expressed as the exploitation index, provides information about which countries are prone

to suffering from water stress because they use more water than there is available from natural resources [2]. An index above 20% is considered a warning level (Figure 1.1). Physical water stress often occurs in Australia, Central Asia, Middle East and North and Southern Africa but also Central and Southern Europe [3].

Today around 4.000 millions of people (two thirds of global population) live under physical water scarcity conditions for at least one month per year, and 500 millions experience severe water stress all year round [4]. In comparison, nowadays 1600 millions of people (a quarter of the world´s population) live economic water shortage [5].

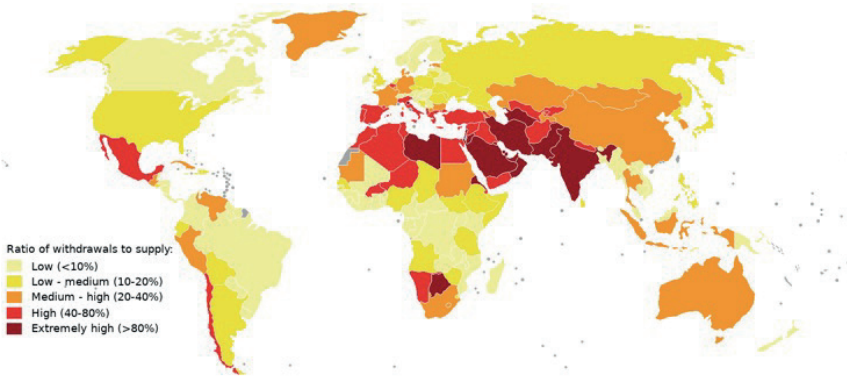

Figure 1.1. Water withdrawals as a percentage of the total available water [3]. Different colors represent a different water withdrawal index. An index above 20% is considered medium-high level of water stress (orange).

The growth of the global population together with the climate change are inducing several hydrological alterations that make a sustainable management of water resources difficult [6]. Many regions of the world are under pressure regarding the availability, quality and quantity of water [7].

Over the past 100 years global water use has increased by a factor of six and continues to grow gradually at a rate of about 1% per year as a result of increasing population, economic development and consumption patterns [8]. Furthermore, the world's amount of freshwater is limited and distributed very irregularly (Figure 1.2). The quality of this freshwater is becoming poorer day by day as a result of a decreased self-purifying capacity due to the increase in population and its associated consequences. As the world population is expected to increase from 7.7 billion of people in 2017 to 9.4-10.2 billion in 2050 [9,10], this growth can exacerbate the pollution of freshwater resources due to an increased municipal and industrial wastewater discharge and the intensification of the agriculture [11].

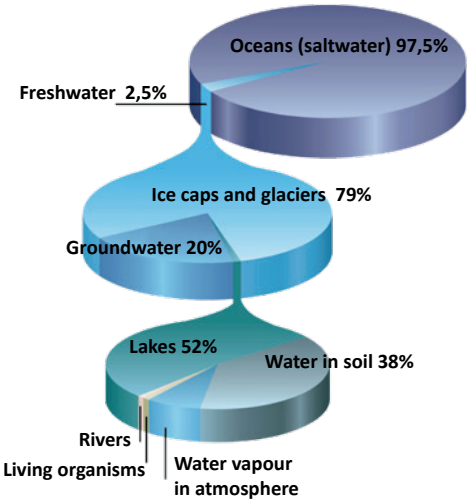

Figure 1.2. Water distribution on the earth. The amount of freshwater is very limited being a 2.5% of the total. This percentage is distributed very irregularly which consequently makes its access difficult.

Thus, there is a strong need to employ technologies that are capable of supplying drinking water reliably and with high quality. Currently, the most viable solution is to produce drinking water by desalination technologies. Desalination reduces the concentration of salts or ions in water from around 35.000 ppm to 500 ppm according to the limit set by the World´s Health Organization [12]. Desalination of seawater can be done either by thermal or membrane-based processes. Thermal desalination separates salts from water through evaporation and condensation whilst membrane-based desalination uses a semipermeable membrane from which the water diffuses and the salts are retained on the feed side [13]. Several thermal processes such as multi-stage flash distillation (MSFD), multi-effect distillation (MED) or vapor compression distillation (VCD) have been widely applied in areas where water salinity is higher than 35.000 ppm such as in the Caribbean or the Middle East [14]. However, membrane-based desalination processes such as reverse osmosis (RO) are becoming more popular in those regions due to their lower energy costs and lower environmental footprint. Table 1.1 reports a comparison between these two methods in terms of energy consumption and produced water cost considering large-scale plants.

Table 1.1. Differences in production capacity, energy consumption and economics between thermal and membrane-based desalination processes [15,16].

Desalination process	Production capacity [m^3/d]	Energy consumption [$kW\ h/m^3$]	Water cost [$US\$/m^3$]
Distillation	10.000-35.000	650	0,52-1,75
Reverse Osmosis	0,1-395.000	3,7-8	0,45-0,66

In 1957, Reid and Breton prepared the first hand-cast thin symmetric cellulose acetate (CA) membrane. This CA membrane was able to retain 98% of salts but its permeability was very low (< 10 ml/m2·h) [17]. Years later, Loeb-Sourirajan developed the first asymmetric CA RO membrane which enabled the desalination of water due to a considerable improvement in the permeate flux [18]. From this discovery onwards, research focused on improving the CA membrane transport properties and manufacturing such as to move to an industrial implementation [19]. CA membranes remained the best membrane option until 1969. Their main disadvantage was that the acetate groups of CA membranes were susceptible to hydrolysis under acidic and alkaline conditions, thus limiting their efficient use in an RO process [20]. There was therefore existed a strong need to develop new membrane materials with better chemical stability. Since then, considerable progress has been made in the synthesis and fabrication of RO membranes with improved permeability and selectivity [19]. Nowadays thin-film composite polyamide (PA-TFC) membranes are the most prevalent membrane types on the RO membrane market [21].

PA-TFC membranes are usually composed of three layers: a net based on polyester which allows mechanical stability (120-150 µm thick), a microporous substrate usually composed of polysulfonic polymers (40 µm thick) and a polyamide selective layer of about 0,2 µm thick [22]. The polyester macroporous phase alone cannot provide sufficient support to the ultra-thin PA selective layer against pressure because it is too porous. Therefore, a microporous intermediate layer is needed.

Nowadays, 80% of the total desalination plants in the world are based on reverse osmosis (RO) [16]. There are 15.906 operational desalination plants with a production capacity of 95,37 millions m^3/day [23]. RO is applied worldwide but its presence is dominant in the Middle East and North Africa (Table 1.2).

Table 1.2. Top ten countries employing desalination of seawater [13].

Rank	Country	Production capacity [millions m^3/d]	Market share [%]
1	Saudi Arabia	9,9	16,5
2	USA	8,4	14,0
3	UAE	7,5	12,5
4	Spain	5,3	8,9
5	Kuwait	2,5	4,2
6	China	2,4	4,0
7	Japan	1,6	2,6
8	Qatar	1,4	2,4
9	Algeria	1,4	2,3
10	Australia	1,2	2,0

However, despite the potential economic advantages that RO offers, one of its biggest challenges is membrane fouling. During the RO process, organic and/or biological matter present in the feed water adsorb on the membrane surface due to molecular interactions generating in this way what is known as fouling or biofouling, respectively [24]. As a consequence, the water permeate flux decreases dramatically and the process efficiency is strongly affected. Apart from strongly reducing productivity and quality of the permeate, membrane fouling also increases operational costs due to an increased energy demand, additional pretreatment, fouling removal by membrane cleaning and reduced membrane lifetime [25].

1.2. Fouling mechanisms

Membrane fouling involves several complex chemical and physical interactions between the foulants present in the feed water and the membrane surface [26]. The development of fouling layers varies depending on different factors such as the membrane material properties (hydrophobicity or charge), the chemical nature of foulants and the hydrodynamic conditions of the process (cross-flow velocity or flux) [25]. Fouling mechanisms of in low pressure membrane processes such as microfiltration (MF) and ultrafiltration (UF) are different from

those of high pressure membrane processes (operating above 10 bar) such as reverse osmosis (RO) and nanofiltration (NF). While pore adsorption and clogging are more frequent in MF and UF membranes [27], surface or external fouling is predominant in RO and NF membranes due to the absence or small diameter, respectively, of pores as they are dense membranes [16].

Membrane fouling is strongly connected to the development of concentration polarization (CP) which is a phenomenon occurring at the membrane surface due to the accumulation of solutes [16,28,29]. The most common approach to explain CP is the so-called Boundary Layer Film Model. This model assumes that a thin layer of unmixed fluid with a certain thickness exits between the membrane surface and the well-mixed bulk fluid. The velocity profile of a fluid flowing over a static surface - which in this case is the RO membrane - is parabolic because the friction at the fluid-membrane surface reduces the fluid velocity next to the membrane to practically zero.

It is in this fluid-membrane interface that a stagnant hydrodynamic boundary layer is generated where mixing occurs solely by diffusion (Figure 1.3). Concentration gradients due to concentration polarization are assumed to be confined to this hydrodynamic boundary layer [30].

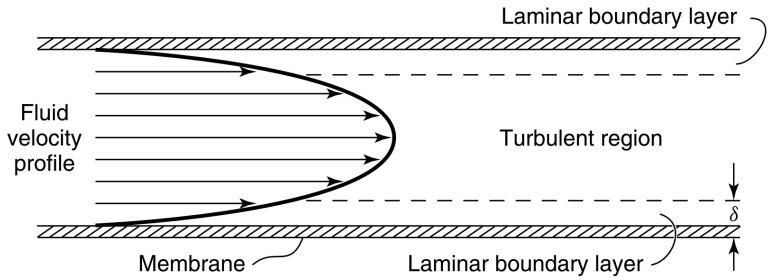

Figure 1.3. Schematic representation of the hydrodynamics in a RO membrane module. The water flow velocity through the RO module is not uniform and it is reduced to essentially zero near to membrane surface creating a hydrodynamic boundary layer where concentration polarization occurs [30].

During RO membrane filtration there is a convective flow of solutes from the well-mixed bulk of the feed side towards the hydrodynamic boundary layer adjacent to the membrane surface [26]. Since the RO membrane is semipermeable and selective to water molecules, salts are rejected and accumulated inside this hydrodynamic boundary layer. As a consequence, there is an enrichment of salts near the membrane surface and therefore the relative concentration of salts increases forming a concentration boundary layer [31]. The movement of molecules inside this concentration boundary layer occurs by diffusion. Thus, the back-diffusion of salts arises from the concentration boundary layer to the bulk due to the existing concentration gradient. However, the convection predominates against the diffusion and accumulation of solutes occurs on the concentration boundary layer (Figure 1.4).

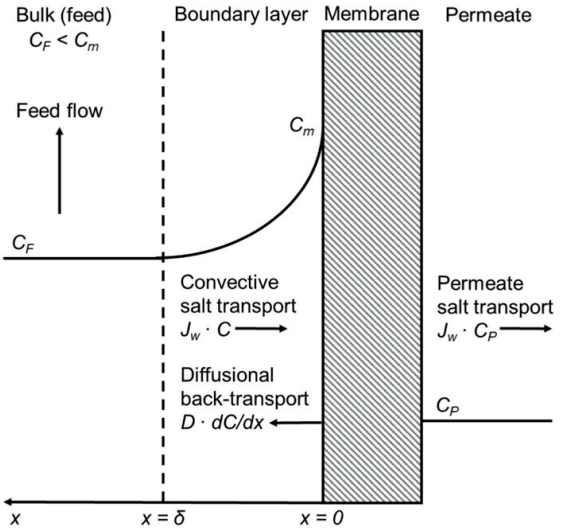

Figure 1.4. Schematic representation of concentration polarization occurring inside the hydrodynamic boundary layer. The diffusional back-transport of solutes from the boundary layer to the bulk is slower than the convective transport of solutes from the bulk into the boundary layer and solutes accumulate in the boundary layer [30].

The main adverse effect of this phenomenon is that the permeate flux decreases because the osmotic pressure that needs to be overcome increases in the boundary layer [32]. On the other hand, salt rejection of the membrane decreases due to the accumulation of salts on the membrane surface. As water does not only contain salt molecules but also foulants, these molecules can establish interactions with the membrane surface causing either reversible or irreversible membrane fouling and forming with time more organised or structured layers which is known as a cake layer [33,34]. The

fouling layers formed hinder the back-diffusion of salts from the boundary layer to the bulk and therefore enhance the CP effect and its associated flux decline. This phenomenon is known as a cake-enhanced concentration polarization (CECP) or cake-enhanced osmotic pressure (CEOP) [35]. Fouling can be both reversible and irreversible. Thus, depending on the reversibility of the fouling layer, the strategy to remove it follow will vary: either increase the hydrodynamics in order to detach reversibly adsorbed foulants or resort to chemical cleaning of the membrane in case of irreversibly adsorbed foulants.

1.3. Types of fouling

Membrane fouling can be categorized in different ways depending on the nature of foulants and the source of water [36,37]. It should be taken into account that the classification of foulants is just a way of getting a clear spectrum about which types of molecules can cause membrane fouling. A real-world filtration process will process water that most probably contains mixtures of potential foulants thus leading to both competitive interactions with the membrane surface and foulant-foulant interactions which might even undergo synergic effects [38]. This renders membrane fouling far more complex than what a simple categorization of foulants might suggest.

1.3.1. Particulate/colloidal fouling

Colloids are fine suspended particles with a size ranging from few nanometres to micrometres [26]. Colloids can be classified according to their size or their chemical composition. Typically, they are classified as settleable solids (> 100 µm), supra-colloidal solids (1 µm to 100 µm), colloidal solids (0,001 µm to 1µm) and dissolved solids (< 0,001 µm) [39]. Colloids can be either organic or inorganic compounds. The most usual inorganic particles are iron oxides/hydroxides, aluminium silicate clays, silica and silt [25]. Some macromolecules such as polysaccharides, proteins and natural organic matter are considered organic colloids [40]. Membrane fouling caused by colloids depends on different parameters such as the colloids size, shape, charge and colloid-colloid interactions [41]. Unfortunately, colloidal solids escape pre-treatments procedures because of their size but there are sufficiently large to be retained at the membrane surface causing inexorable fouling. Small size colloids are principally responsible for this type of fouling [39]. Larger colloids are less problematic because of the hydrodynamic lift effect owing to the cross-flow velocity profile near the membrane surface [42].

1.3.2. Organic fouling

Organic compounds are very difficult to remove from feedwater in pre-treatment steps. Organic foulants frequently comprise humic substances, polysaccharides, proteins, lipids, nucleic acids, amino

acids, organic acids and cell fragments [25]. Organic foulants can be classified in many different ways but the most habitual classification is made considering the source of the filtrated water. This type of foulants are mainly categorized in three different groups [42,43]: 1) natural organic matter (NOM); 2) algae organic matter (AOM) and 3) wastewater effluent organic matter (EfOM). The most representative organic foulants are humic substances, polysaccharides such as sodium alginate and proteins. Both humic compounds and alginates can complex with some cations such as Ca2+ forming gel-type structures and thus aggravating the generated fouling layers [44,45].

1.3.3. Biofouling

Biofouling involves the deposition of bacterial cells and different microorganisms such as fungi and microalgae [36]. A gel-type biofilm is formed due to the adhesion and growth of bacteria on the membrane surface. A biofilm is thus composed not only of the adsorbed microorganism but of the extracellular polymeric substances (EPS) segregated by those microorganisms which at the same time serves as a conditioning layer for further biofouling development [46].

1.3.4. Scaling

Scaling occurs when inorganic compounds present in the feed water form mineral precipitates on the membrane surface [47].

During a RO process, there is an enrichment of salts near the membrane surface as their concentration continuously increases due to the hindered back-diffusion from the hydrodynamic boundary layer to the bulk solution. Salt concentration within the boundary layer usually increases between 4-10 times depending on the salt-rejection efficiency of the membrane and the operating conditions of the process [46]. Therefore, a supersaturation is reached and when the salts exceed their solubility limit, they crystallize and precipitate on the membrane surface [48]. Some typical compounds forming scaling are: calcium carbonate, calcium sulphate, calcium phosphate, barium sulphate and silicates [49]. Scaling is commonly called “inorganic fouling” and classified as one type of fouling. However, it should be stressed that it does not occur due to a chemical interaction with the membrane surface but rather due to a physical phenomenon.

All in all, although classifying different types of foulants based on their nature or chemical structure could be useful in order to understand their potential to foul the membrane on a real filtration process, it is essential to understand that membrane fouling is a very complex phenomenon made up of a wide variety of compounds. These do not only establish chemical interactions with the membrane but usually create foulant-foulant interactions, thus generating highly complex fouling layers [50,51].

1.4. How to deal with membrane fouling

Membrane fouling is a phenomenon which until today cannot be completely avoided. Attempts are therefore being made to at least minimize the degree of fouling. One strategy is to modify the membrane surface chemically [52]. Different approaches have been studied for this purpose, for example grafting of hydrophilic polymeric chains onto the RO membrane surface in order to minimize the undesired adsorption of molecules [53] or application of a coating layer composed of a neutral and charged hydrophilic polymeric material such as polyvinyl alcohol (PVA) onto the RO membrane surface [54]. In fact, some membrane manufacturers such as Filmtec and Hydranautics applied a PVA coating in some of their commercial RO membranes [55].

The problem with those strategies is that there is low control over the efficiency of the chemical modification because it seems to be difficult to get a homogeneous coating on the top of the membrane surface [53]. One way to circumvent this problem is to modify the respective monomers prior to polymerization [56]. In any case, chemical modifications of the membrane surface are often based on a trial-and-error approach and therefore require intensive and time-consuming screening of whether the modifications have been efficient or not. In this context, accurate, fast, and non-invasive techniques would be desirable in order to verify the efficiency of the adopted anti-fouling strategy in a time-efficient and material-extensive manner.

Another strategy to minimize the detrimental effects of fouling is its early-stage detection which enables adapting an optimal process operating and cleaning strategy. Unfortunately, current monitoring techniques neither reach the necessary efficiency nor sensitivity for detecting phenomena below a certain detection threshold (Figure 1.5). As a result, membrane fouling is detected when it is already quite developed resulting on elevated cleaning and process costs. Thus, there is a need for developing techniques that could allow detecting fouling at an early stage and as such in an anticipative way.

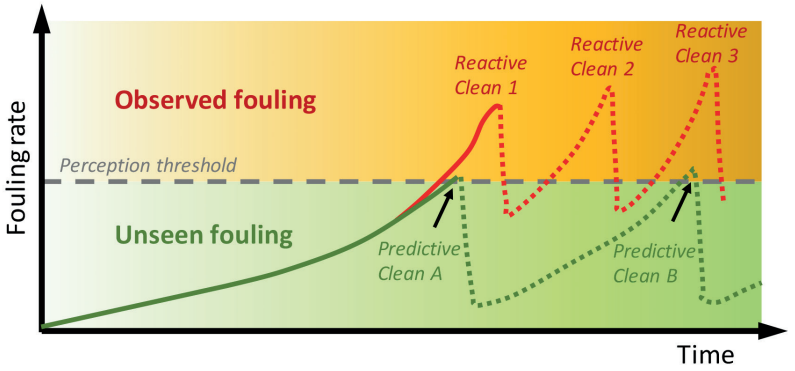

Figure 1.5. Limited ability to detect fouling in industry (above the perception threshold): Membrane cleaning intervals are more frequent due to their lack of efficiency. The monitoring method should performance in the desired range and currently imperceptible from the operator's point of view: consequently, the cleaning intervals are prolonged in time because they are more efficient (under the perception threshold). The figure was adapted from reference [57].

1.5. Outline

This thesis presents an approach to overcoming the limitations of conventional fouling monitoring methods by combining two advanced surface-sensitive techniques for monitoring membrane fouling: quartz crystal microbalance with dissipation monitoring (QCM-D) and multi-parameter surface plasmon resonance (MP-SPR).

It will be shown that these non-invasive techniques are both highly feasible for characterizing the build-up of the very first fouling layers at the nanoscale, and that they possess a high potential of significantly accelerating the screening of the efficiency of both membrane modifications as well as that of commonly applied membrane cleaning protocols (Chapters 3, 4 and 5).

The final aim of this thesis is to demonstrate that this combination of techniques is a disruptive monitoring system capable of detecting membrane fouling at an early-stage, and thus providing operators of desalination plants with a monitoring tool of an unprecedented sensitivity (Chapter 6 and 7).

1.6. References

[1] D. Molden, Water for Food Water for Life, Routledge, 2013. https://doi.org/10.4324/9781849773799.

[2] D. Vanham, A.Y. Hoekstra, Y. Wada, F. Bouraoui, A. de Roo, M.M. Mekonnen, W.J. van de Bund, O. Batelaan, P. Pavelic, W.G.M. Bastiaanssen, M. Kummu, J. Rockström, J. Liu, B. Bisselink, P. Ronco, A. Pistocchi, G. Bidoglio, Physical water scarcity metrics for monitoring progress towards SDG target 6.4: An evaluation of indicator 6.4.2 "Level of water stress," Sci. Total Environ. 613–614 (2018) 218–232. https://doi.org/10.1016/j.scitotenv.2017.09.056.

[3] T. Luo, R. Young, P. Reig., Aqueduct Projected Water Stress Country Rankings. Technical Note. Washington, D.C.: World Resources Institute, (2015) 1–16.

[4] M.M. Mekonnen, A.Y. Hoekstra, Sustainability: Four billion people facing severe water scarcity, Sci. Adv. 2 (2016) 1–7. https://doi.org/10.1126/sciadv.1500323.

[5] A.C. Clark, Message from the chair, Eng. Des. Graph. J. 76 (2012).

[6] T. Distefano, S. Kelly, Are we in deep water? Water scarcity and its limits to economic growth, Ecol. Econ. 142 (2017) 130–147. https://doi.org/10.1016/j.ecolecon.2017.06.019.

[7] N. Ferri, United nations general assembly, Int. J. Mar. Coast. Law. 25 (2010) 271–287. https://doi.org/10.1163/157180910X12665776638740.

[8] T. United, N. World, W. Development, WATER AND, n.d.

[9] A. Panagopoulos, K.-J. Haralambous, M. Loizidou, Desalination brine disposal methods and treatment technologies - A review, Sci. Total Environ. 693 (2019) 133545. https://doi.org/10.1016/j.scitotenv.2019.07.351.

[10] R. Lee, The outlook for population growth, Science (80-.). 333 (2011) 569–573. https://doi.org/10.1126/science.1208859.

[11] P. Greve, T. Kahil, J. Mochizuki, T. Schinko, Y. Satoh, P. Burek, G. Fischer, S. Tramberend, R. Burtscher, S. Langan, Y. Wada, Global assessment of water challenges under uncertainty in water scarcity projections, Nat. Sustain. 1 (2018) 486–494. https://doi.org/10.1038/s41893-018-0134-9.

[12] N.C. Darre, G.S. Toor, Desalination of Water : a Review, (2018) 104–111.

[13] M. Nair, D. Kumar, Water desalination and challenges: The Middle East perspective: A review, Desalin. Water Treat. 51 (2013) 2030–2040. https://doi.org/10.1080/19443994.2013.734483.

[14] P. Xu, A.P. Robertson, M. Reinhard, T.Y. Cath, Critical Review of Desalination Concentrate Management, Treatment and Beneficial Use, (2013). https://doi.org/10.1089/ees.2012.0348.

[15] A. Al-Karaghouli, L.L. Kazmerski, Energy consumption and water production cost of conventional and renewable-energy-powered desalination processes, Renew. Sustain. Energy Rev. 24 (2013) 343–356. https://doi.org/10.1016/j.rser.2012.12.064.

[16] L.F. Greenlee, D.F. Lawler, B.D. Freeman, B. Marrot, P. Moulin, Reverse osmosis desalination: Water sources, technology, and today's challenges, Water Res. 43 (2009) 2317–2348. https://doi.org/10.1016/j.watres.2009.03.010.

[17] C.E. Reid, E.J. Breton, Water and ion flow across cellulosic membranes, J. Appl. Polym. Sci. 1 (1959) 133–143. https://doi.org/10.1002/app.1959.070010202.

[18] S. Loeb, S. Sourirajan, Sea Water Demineralization by Means of an Osmotic Membrane. In Saline Water Conversion-II Chapter 9, Adv. Chem. ACS. 38 (1963) 117–132. https://doi.org/10.1021/ba-1963-0038.

[19] K.P. Lee, T.C. Arnot, D. Mattia, A review of reverse osmosis membrane materials for desalination-Development to date and future potential, J. Memb. Sci. 370 (2011) 1–22. https://doi.org/10.1016/j.memsci.2010.12.036.

[20] K.J. Edgar, C.M. Buchanan, J.S. Debenham, P.A. Rundquist, B.D. Seiler, M.C. Shelton, D. Tindall, Advances in cellulose ester performance and applicaton. pdf.crdownload, Prog. Polym. Sci. 26 (2001) 1605–1688.

[21] N. Misdan, W.J. Lau, A.F. Ismail, Seawater Reverse Osmosis (SWRO) desalination by thin-film composite membrane-Current development, challenges and future prospects, Desalination. 287 (2012) 228–237. https://doi.org/10.1016/j.desal.2011.11.001.

[22] P.S. Singh, S. V. Joshi, J.J. Trivedi, C. V. Devmurari, A.P. Rao, P.K. Ghosh, Probing the structural variations of thin film composite RO membranes obtained by coating polyamide over polysulfone membranes of different pore dimensions, J. Memb. Sci. 278 (2006) 19–25. https://doi.org/10.1016/j.memsci.2005.10.039.

[23] E. Jones, M. Qadir, M.T.H. van Vliet, V. Smakhtin, S. Kang, The state of desalination and brine production: A global outlook, Sci. Total Environ. 657 (2019) 1343–1356. https://doi.org/10.1016/j.scitotenv.2018.12.076.

[24] M. Barger, R.P. Carnahan, Fouling prediction in reverse osmosis processes, Inst. Chem. Eng. Symp. Ser. 3 (1991) 3–33.

[25] S. Jiang, Y. Li, B.P. Ladewig, A review of reverse osmosis membrane fouling and control strategies, Sci. Total Environ. 595 (2017) 567–583. https://doi.org/10.1016/j.scitotenv.2017.03.235.

[26] M. Qasim, M. Badrelzaman, N.N. Darwish, N.A. Darwish, N. Hilal, Reverse osmosis desalination: A state-of-the-art review, Desalination. 459 (2019) 59–104. https://doi.org/10.1016/j.desal.2019.02.008.

[27] P. Bacchin, A. Marty, P. Duru, M. Meireles, P. Aimar, Colloidal surface interactions and membrane fouling: Investigations at pore scale, Adv. Colloid Interface Sci. 164 (2011) 2–11. https://doi.org/10.1016/j.cis.2010.10.005.

[28] P. Bacchin, P. Aimar, Critical fouling conditions induced by colloidal surface interaction: From causes to consequences, Desalination. 175 (2005) 21–27. https://doi.org/10.1016/j.desal.2004.09.020.

[29] A. Pervov, The influence of hydrodynamic factors, membrane surface properties and channel geometries on membrane performance and fouling mechanisms, MATEC Web Conf. 86 (2016). https://doi.org/10.1051/matecconf/20168603006.

[30] R.W. Baker, Membrane technologies and applications, 2011. https://doi.org/10.1201/b11416.

[31] C. Fritzmann, J. Löwenberg, T. Wintgens, T. Melin, State-of-the-art of reverse osmosis desalination, Desalination. 216 (2007) 1–76. https://doi.org/10.1016/j.desal.2006.12.009.

[32] I. Sutzkover, D. Hasson, R. Semiat, Simple technique for measuring the concentration polarization level in a reverse osmosis system, Desalination. 131 (2000) 117–127. https://doi.org/10.1016/S0011-9164(00)90012-2.

[33] C. Park, Y.H. Lee, S. Lee, S. Hong, Effect of cake layer structure on colloidal fouling in reverse osmosis membranes, Desalination. 220 (2008) 335–344. https://doi.org/10.1016/j.desal.2007.01.038.

[34] F. Pignon, A. Magnin, J.M. Piau, B. Cabane, P. Aimar, M. Meireles, P. Lindner, Structural characterisation of deposits formed during frontal filtration, J. Memb. Sci. 174 (2000) 189–204. https://doi.org/10.1016/S0376-7388(00)00394-X.

[35] E.M.V. Hoek, M. Elimelech, Cake-Enhanced Concentration Polarization: A New Fouling Mechanism for Salt-Rejecting Membranes, Environ. Sci. Technol. 37 (2003) 5581–5588. https://doi.org/10.1021/es0262636.

[36] Q. She, R. Wang, A.G. Fane, C.Y. Tang, Membrane fouling in osmotically driven membrane processes: A review, J. Memb. Sci. 499 (2016) 201–233. https://doi.org/10.1016/j.memsci.2015.10.040.

[37] I. Ibrar, O. Naji, A. Sharif, A. Malekizadeh, A. Alhawari, A.A. Alanezi, A. Altaee, A review of fouling mechanisms, control strategies and real-time fouling monitoring techniques in forward osmosis, Water (Switzerland). 11 (2019). https://doi.org/10.3390/w11040695.

[38] V. Aimar, P., Meireles, M., Bacchin, P., Sanchez, Fouling and concentration polarization in ultrafiltration and microfiltration., in: João G. Crespo, Karl W. Böddeker. Membr. Process. Sep. Purification, Springer., 1994: pp. 27–57.

[39] S.G. Yiantsios, D. Sioutopoulos, A.J. Karabelas, Colloidal fouling of RO membranes : an overview of key issues and efforts to develop improved prediction techniques, 183 (2005) 257–272. https://doi.org/10.1016/j.desal.2005.02.052.

[40] C.Y. Tang, T.H. Chong, A.G. Fane, Colloidal interactions and fouling of NF and RO membranes: A review, Adv. Colloid Interface Sci. 164 (2011) 126–143. https://doi.org/10.1016/j.cis.2010.10.007.

[41] J. Buffle, K.J. Wilkinson, S. Stoll, M. Filella, J. Zhang, A generalized description of aquatic colloidal interactions: The three- culloidal component approach, Environ. Sci. Technol. 32 (1998) 2887–2899. https://doi.org/10.1021/es980217h.

[42] L.N. Sim, T.H. Chong, A.H. Taheri, W.B. Krantz, A.G. Fane, S.T. V Sim, A review of fouling indices and monitoring techniques for reverse osmosis, Desalination. 434 (2018) 169–188. https://doi.org/10.1016/j.desal.2017.12.009.

[43] G. Amy, Fundamental understanding of organic matter fouling of membranes, Desalination. 231 (2008) 44–51. https://doi.org/10.1016/j.desal.2007.11.037.

[44] K. Katsoufidou, S.G. Yiantsios, A.J. Karabelas, A study of ultrafiltration membrane fouling by humic acids and flux recovery by backwashing: Experiments and modeling, J. Memb. Sci. 266 (2005) 40–50. https://doi.org/10.1016/j.memsci.2005.05.009.

[45] H.C. Kim, B.A. Dempsey, Membrane fouling due to alginate, SMP, EfOM, humic acid, and NOM, J. Memb. Sci. 428 (2013) 190–197. https://doi.org/10.1016/j.memsci.2012.11.004.

[46] L.N. Sim, T.H. Chong, A.H. Taheri, S.T.V. Sim, L. Lai, W.B. Krantz, A.G. Fane, A review of fouling indices and monitoring techniques for reverse osmosis, Desalination. 434 (2018) 169–188. https://doi.org/10.1016/j.desal.2017.12.009.

[47] A. Antony, J.H. Low, S. Gray, A.E. Childress, P. Le-Clech, G. Leslie, Scale formation and control in high pressure membrane water treatment systems: A review, J. Memb. Sci. 383 (2011) 1–16. https://doi.org/10.1016/j.memsci.2011.08.054.

[48] C.A.C. Van De L, J.A.M. Van Paassen, J.C. Schippers, Monitoring scaling in nanofiltration and reverse osmosis membrane systems, 132 (2000) 101–108.

[49] A. Antony, J. How, S. Gray, A.E. Childress, P. Le-clech, G. Leslie, Scale formation and control in high pressure membrane water treatment systems : A review, J. Memb. Sci. 383 (2011) 1–16. https://doi.org/10.1016/j.memsci.2011.08.054.

[50] W.S. Ang, A. Tiraferri, K.L. Chen, M. Elimelech, Fouling and cleaning of RO membranes fouled by mixtures of organic foulants simulating wastewater effluent, J. Memb. Sci. 376 (2011) 196–206. https://doi.org/10.1016/j.memsci.2011.04.020.

[51] H. Xu, K. Xiao, X. Wang, S. Liang, C. Wei, X. Wen, X. Huang, Outlining the Roles of Membrane-Foulant and Foulant-Foulant Interactions in Organic Fouling During Microfiltration and Ultrafiltration: A Mini-Review, Front. Chem. 8 (2020) 1–14. https://doi.org/10.3389/fchem.2020.00417.

[52] G. dong Kang, Y. ming Cao, Development of antifouling reverse osmosis membranes for water treatment: A review, Water Res. 46 (2012) 584–600. https://doi.org/10.1016/j.watres.2011.11.041.

[53] F. Poncin-Epaillard, T. Vrlinic, D. Debarnot, M. Mozetic, A. Coudreuse, G. Legeay, B. El Moualij, W. Zorzi, Surface Treatment of Polymeric Materials Controlling the Adhesion of Biomolecules, J. Funct. Biomater. 3 (2012) 528–543. https://doi.org/10.3390/jfb3030528.

[54] J. Nikkola, X. Liu, Y. Li, M. Raulio, H.L. Alakomi, J. Wei, C.Y. Tang, Surface modification of thin film composite RO membrane for enhanced anti-biofouling performance, J. Memb. Sci. 444 (2013) 192–200. https://doi.org/10.1016/j.memsci.2013.05.032.

[55] R.R. Choudhury, J.M. Gohil, S. Mohanty, S.K. Nayak, Antifouling, fouling release and antimicrobial materials for surface modification of reverse osmosis and nanofiltration membranes, J. Mater. Chem. A. 6 (2018) 313–333. https://doi.org/10.1039/c7ta08627j.

[56] S. Molina, P. Carretero, S.B. Teli, J.G. De la Campa, Á.E. Lozano, J. De Abajo, Hydrophilic porous asymmetric ultrafiltration membranes of aramid-g-PEO copolymers, J. Memb. Sci. 454 (2014) 233–242. https://doi.org/10.1016/j.memsci.2013.11.025.

[57] H. Min, F. Zhou, S. Jui, T. Wang, X. Chen, White Paper White Paper, Distribution. (2004) 1–23. http://classtap.pbworks.com/f/SkillSoft+-+Blended+E-learning.pdf.

CHAPTER 2

MATERIALS AND METHODS

2.1. Membrane model polymers

All the experiments carried out throughout this thesis were accomplished using two different types of polyamides as a membrane polymer model. The first batch of polyamides was synthesized and kindly provided by the Institute of Polymer Science and Technology (CSIC, Madrid). The second polymer used was commercial. The aim was to mimic the selective layer of a polyamide-based thin-film composite (PA-TFC) RO membrane on the sensors used for all the measurements.

2.1.1. Polyamides modified with polyethylene glycol (PA-PEG)

Polyamides (PA) with different degrees of polyethylene glycol (PEG) were prepared according to a procedure described by Molina et al. [1] and kindly provided by Prof. Javier de Abajo

(CSIC, Madrid). Figure 2.1 illustrates the general structure of the resulting PA-PEG copolymer. The modification of the PA was carried out by introducing 12 units of ethylene oxide (EO) to the side chains (unit "x" in Figure 2.1). The sum of the units x and y is 1, which means that at "100%" of PEG modification the polymer will in fact be composed of only "x" units.

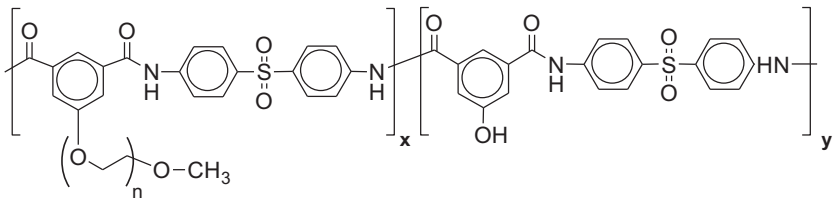

Figure 2.1. General structure of the PA-PEG polymer; the x-unit bears the PEG modification while the y-unit remains unmodified.

Studies presented on Chapter 3 were conducted using these polymers. Data shown in Chapters 5 and 6 were obtained using the unmodified PA-PEG0 polymer.

2.1.2. NOMEX based commercial polyamide (c-PA)

Commercially available Poly[N,N'-(1,3-phenylene)isophthalamide] aromatic polyamide based on NOMEX structure was used (Sigma-Aldrich, CAS number 68-12-2). Figure 2.2 depicts its chemical structure. The chemical structure of this polyamide is similar to the selective layer of RO membranes used in desalina-

tion. Thus, it was selected as an industrial membrane model for performing fouling experiments reflected in Chapter 4.

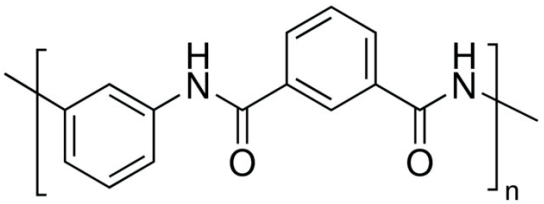

Figure 2.2. Chemical structure of the Poly[N,N´-(1,3-phenylene)isoftalamide].

2.2 Representative organic fouling model system

The model foulant selected to simulate organic fouling caused by proteins was bovine serum albumin (BSA). BSA (Sigma-Aldrich, CAS number 9048-46-8) was received in a powder form, and a stock solution of 1000 ppm was prepared by dissolving it in a phosphate buffered saline solution (PBS, Sigma-Aldrich). The pH was adjusted to 8.0 such as to be above the isoelectric point of BSA (pH of 4.7). This solution was used for studies presented in Chapter 3.

Experiments described in Chapter 4 were carried out using different solutions of BSA of increasing concentrations: 1, 5, 10, 30, 50, 100, 200, 500 and 1000 ppm. All the solutions were prepared in PBS buffer.

On the other hand, sodium alginate (ALG, Sigma Aldrich, CAS number 9005-38-3) and humic acid (HA, Sigma Aldrich, CAS

number 68131-04-4) were used in Chapter 4 and 5 with the aim to study the fouling caused by natural organic matter (NOM) typically present in water. These compounds were received in a powder form and different stock solutions were prepared (2, 20, 200 and 2000 ppm) in ultra-pure water and PBS buffer.

For studies performed in Chapter 6, Casein (CAS) from bovine milk (Sigma-Aldrich, CAS number 9000-71-9) was employed as a protein model foulant due to its low cost compared to BSA. CAS was received in a powder form, and a stock solution of 100 ppm in ultra-pure water was prepared.

2.3. Membrane cleaning agents

Three different cleaning protocols were tested to study if, and how they removed organic fouling from the PA sensor surface. Cleaning agents comprised a commercial and a custom-made alkaline solution as well as a commercial enzymatic solution. Both the commercial enzymatic ("CES") and the commercial alkaline ("CAS1") solutions were provided by OTARI Ingeniería del agua S.L. (Irún, Spain).

The commercial CAS1 alkaline solution was a high pH (11-12) solution employed for organic fouling removal. It included pyro-phosphates which are to control both scale formation and the final pH of the solution, apart from acting as a dispersing agent. CAS1 was used as received according to the recommendations of the manufacturer (OTARI).

The custom-made alkaline solution (“AS2”) was a mixture of 0.1% (w) sodium hydroxide (NaOH) and 0.03% (w) sodium dodecyl sulfate (SDS). This solution was prepared according to a protocol published by Hydranautics, USA [2].

2.4. Solvents

N,N-Dimethylformamide (DMF, Scharlab, CAS number 68-12-2), N-N-Dimethylacetamide (DMAc, Sigma Aldrich, CAS 127-19-5), Dichloromethane (DCM, Scharlab, CAS number 75-09-2), Ethanol (EtOH, Sigma Aldrich, CAS number 64-17-5), Ammonium Hydroxide (NH4OH, Sigma Aldrich, CAS number 1336-21-6), Hydrogen Peroxide (H202, Sigma Aldrich, CAS number 7722-84-1) were used as solvents for polymer solutions and cleaning the sensors. All the solvents were reagent grade purchased from Sigma Aldrich and they were used as a received without further purification steps. Ultra-pure water (18Ω) was employed from the Ultra Clear TWF with El-Ion CEDI electro deionization system from Inycom, Spain.

2.5. Ultra-thin PA film formation on QCM-D/MP-SPR sensors by spin-coating

In order to study interactions between different foulants and polyamides, the polymer solutions were cast on both QCM-D and MP-SPR gold sensors by spin-coating. Spin-coating was employed as a first approach as it is an easy and quick method to crea-

te ultra-thin films. As a consequence, one of the concerns of this work was to see how reproducible the deposition was and in how many possible variations could possibly affect the reliability of the measurements.

All PA-PEG polyamides were initially dissolved in DMAc obtaining solutions of 3% (wt/wt). However, it was not possible to get a satisfactory deposition by spin-coating due to the low volatility of the solvent. Therefore, DCM was added as a more volatile co-solvent obtaining mixtures of 1:2 DMAc-DCM. On the other hand, the commercial polyamide (C-PA) was dissolved in a 1:1 mixture of DMF and LiCl obtaining a concentration of 1% (wt/wt). In order to improve the solubility of the polymer into de solvent the vial was heated up to 100 °C for 20 minutes.

The final solutions of all the polymers were filtered using a polytetrafluoroethylene (PTFE) filter of 0,45 µm of pore size (Whatman, CAT number 6784-1304), so that possible dispersed particle aggregates were removed.

Both QCM-D and MP-SPR gold sensors were cleaned before PA film deposition according to a cleaning procedure established by the manufacturer (Biolin Scientific, Sweden):

- Immerse the sensors in ethanol and place in an ultrasound bath (Farfield Aries 101, Fisher) for 15 minutes.
- Dry the sensors with nitrogen gas and introduce them in the UV/ozone cleaner (ProcleanerTM Plus, Bioforce Nanoscience) for 10 minutes in order to eliminate organic contaminants.

- Heat 10 ml of a 5:1:1 mixture of ultrapure water, ammonia (25%) and hydrogen peroxide (30%), respectively, to 75-90°C.
- Place the sensor in the heated solution for 5 minutes.
- Rinse with ultrapure water. It is important that the surfaces are kept wet after ammonium-peroxide immersion until they are rinsed with water.
- Dry with nitrogen gas.
- Rinse with 99% of ethanol.
- Dry with nitrogen gas.

After the cleaning procedure, the sensor was placed onto the spin-coater (SCC-200, Novocontrol Technologies, Germany) and held in place by a vacuum pump (KNF Laboport). Then, 2 µl of the polymer solution were deposited onto the sensor surface using a micropipette (Eppendorf Research Plus) and the spinning initiated immediately afterwards using the following program:

1. 10 seconds to reach a velocity of 20 rps followed by 20 seconds at 20 rps.
2. 10 seconds to reach a velocity of 25 rps followed by 20 seconds at 25 rps.

By the end of the program, the solvent had visibly evaporated from the sensor surface which apparently was covered evenly

with the thin polyamide film (Figure 2.3). PA deposition was optimized such as to warrant surface coverage of the sensor and avoid possible pinholes.

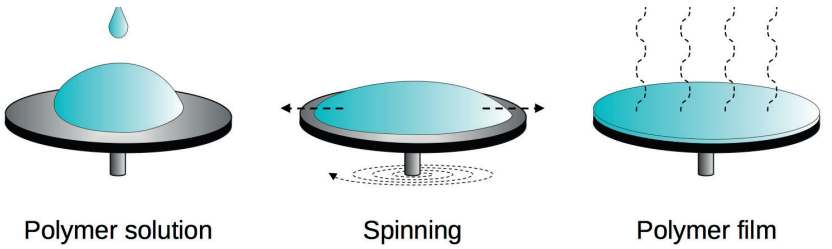

Figure 2.3. Schematic representation of the ultra-thin PA film formation by spin-coating.

2.6. Characterization of the PA-films

2.6.1. Atomic Force Microscopy (AFM)

The surface topography of the ultra-thin PA films was examined by AFM in both air (Nano Observer Solutions, CSInstrument, France) in tapping-mode and PBS buffer conditions (Ultra Speed, JPK Instruments, Germany) in QI (quantitative imaging) mode. Samples were prepared by casting polyamides on QCM-D sensor surfaces as described in Section 2.5. After polyamide film formation, the sensors were kept under vacuum for 12 hours prior to AFM measurements. For each sensor, four different regions of the PA surface were investigated in order to get a better understanding of the homogeneity of the polyamide film surface.

Roughness values were obtained for each polyamide with each roughness value being an average of ten different points of the same AFM image.

The software used expresses the roughness in two different ways: as an arithmetic average roughness (Ra, Equation 2.1) and as a root mean square roughness (Rms or Rq, Equation 2.2).

$$Ra = \sqrt{\frac{1}{n}} \cdot \sum_{i=1}^{n} |y_i| \qquad \textbf{Equation 2.1}$$

$$Rq = \sqrt{\frac{1}{n}} \cdot \sum_{i=1}^{n} {y_i}^2 \qquad \textbf{Equation 2.2}$$

Being n: number of samples measured; yi: height measured.

2.6.2. Water contact angle (CA)

Samples were prepared as described in Section 2.5. After PA film formation, the sensors were kept under vacuum for 12 hours prior to the water CA measurement. Measurements were performed using the OCA 20 Instrument (Dataphysics). The volume of the water drop deposited onto polyamide films was 10 µL. Replicas were made with the sensors being dried under vacuum for 12 hours in between measurements.

2.6.3. X-ray photoelectron spectroscopy (XPS)

XPS measurements were conducted in order to characterize the surface chemistry of the polyamide films. The experiments were carried out at the general X-ray facility UPV/EHU (SGIKER) using a SPECS system (Berlin, Germany) equipped with a Phoibos 150-1D-DLD analyzer and using a monochromatic radiation Al Kα (1486.7 eV). The spectra were analyzed trough CasaXPS 2.3.16 software. According to the SGIKER/X-ray facility, the penetration depth of the electron beam was about 10 nm.

The atoms considered for the experiments were carbon, oxygen, nitrogen and sulfur. The percentage of each atom was calculated as a relative percentage. Samples were prepared as described in Section 2.5. After the PA-film formation, all the sensors were dried prior to XPS measurement in order to remove solvent residues.

An initial analysis of the elements present was carried out (wide scan: step energy 1 eV, dwell time 0.1 s, pass energy 80 eV) and a detailed analysis of the elements present (detail scan: step energy 0.1 eV, dwell time 0.1 s, pass energy 30 eV) with an electron exit angle of 90° was performed.

2.7. Fouling and chemical cleaning measurements (Chapters 3 to 5)

All fouling (Chapter 3 and 4) and cleaning experiments (Chapter 5) were conducted using both quartz crystal microbalance with dissipation monitoring (QCM-D) and multi-parameter surface plasmon resonance (MP-SPR). The experimental setup and data

acquisition software used is described in the following sections together with the experimental procedures for each method.

2.7.1. Quartz Crystal Microbalance with Dissipation monitoring (QCM-D)

2.7.1.1. The QCM-D System

Adsorption of foulants on polyamides was studied using a system E4 (Q-Sense Analyzer, Biolin-Scientific, Sweden). Figure 2.4 depicts all the elements from which the QCM-D setup comprised. Four identical flow modules each containing a sensor crystal were the core of the measurement system and connected in parallel to the electronics. Data were recorded using the data acquisition software provided by the supplier (QSoft 101, Biolin-Scientific, Sweden) and processed by the QTools software (Biolin-Scientific, Sweden). Layer thicknesses of the polyamide films were calculated from raw data acquired by the QSoft software.

Figure 2.4. QCM-D experimental set-up adapted from [3].

2.7.1.2. QCM-D sensors

Polyamides were deposited onto gold-coated QCM-D sensors (QSX 301, Biolin Scientific, Sweden) as described in Section 2.5. QCM-D sensors consist of a piezoelectric quartz crystal of 14 mm in total diameter covered on both sides by two gold electrodes (Figure 2.5). The polymer was deposited onto the sensing side (active electrode) keeping the counter electrode as clean as possible in order to avoid disturbing the electrical signal. The effective sensor area was of 1 cm^2.

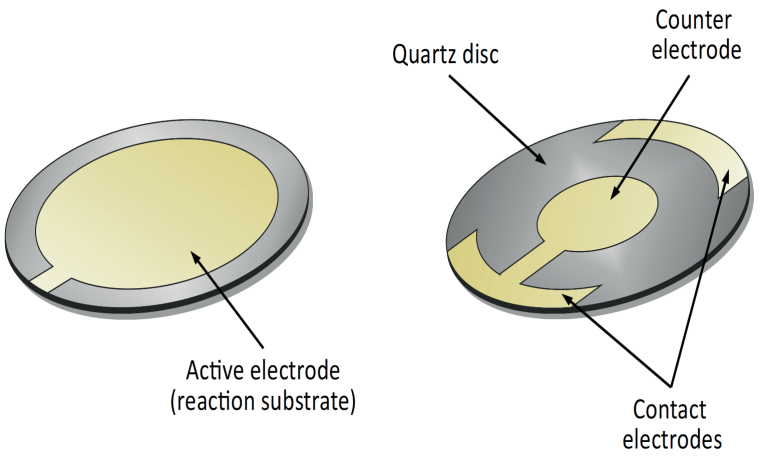

Figure 2.5. Two sides of the QCM-D quartz sensor: a) the sensing side where the polymer deposition is made; b) the contact side.

2.7.1.3. Basic QCM-D fundamentals

QCM-D is an acoustic technique in which the working principle is the resonance behavior of the crystalline piezoelectric material of the sensor used [4]. During a measurement with QCM-D,

two parameters are determined in real time: the change in frequency (ΔF) and the change in energy dissipation (ΔD). The use of quartz crystal microbalances (QCM) for measuring molecular interactions on surfaces in liquids goes back many decades [5,6]. However, it is only more recently that through measuring the impedance of the quartz sensor or applying the ring-down technique at least qualitative information on the viscoelasticity of adsorbed layers can also be obtained. The “D” in QCM-D stands for the so-called “dissipation factor” which provides information about the viscoelasticity or the “softness” of the adsorbed layer.

Sauerbrey proved that the frequency change is proportional to the adsorbed mass per area (or surface density) on the sensor surface as long as the mass adsorbed forms a rigid layer [7], following the equation:

$$\Delta m = -\frac{\nu_q \cdot \rho_q}{2 \cdot f_0^2} \cdot \frac{\Delta f}{n} = -C \cdot \frac{\Delta f}{n} \qquad \textbf{Equation 2.3}$$

with Δf: frequency change [s^{-1}]; Δm: adsorbed mass change per area [$ng \cdot cm^{-2}$] with the active area of the sensor being 1 cm^2; constant “C” equals 17,7 [$g \cdot s \cdot cm^{-2}$] in the case of the 5 MHz crystal used in this work with vq: wave velocity in quartz plate, here 3,34·105 [$cm \cdot s^{-1}$]; ρq: density of quartz, here 2,65 [$g \cdot cm^3$] and f_0: fundamental resonance frequency [s^{-1}]; n: number of harmonic. Concurrently with the frequency measurement, changes in energy dissipation were measured from which it was possible to deri-

ve information about the viscoelastic properties of the adsorbed film, i.e. whether it was “rigidly” or “softly” adsorbed. The ratio ΔD/ΔF represented changes in viscoelasticity per unit frequency (synonymous with mass adsorbed per area or surface density) illustrating possible compaction or swelling of the surface layer upon exposure changing liquid compositions.

2.7.1.4. Fouling and cleaning experiments

Prior to the fouling and cleaning experiments, all solutions were degassed either manually using a syringe when denaturation could occur (in the case of BSA solutions), or in an ultrasound bath for 15 minutes. All solutions were passed over the sensor surface using a peristaltic pump (Ismatec) with a continuous flow of 100 µl/min and at 23°C. In order to obtain a stable baseline as a reference, for each experiment the PBS buffer was passed over the sensor for about 90 minutes under the abovementioned conditions before injecting the foulant solutions. This time usually sufficed to equilibrate the ultra-thin PA film in the liquid. Stability was considered to be achieved when the frequency change was below 0.1 Hz/min. Each adsorption experiment was followed by rinsing with PBS buffer in order to see any desorption of the foulant (Figure 2.6).

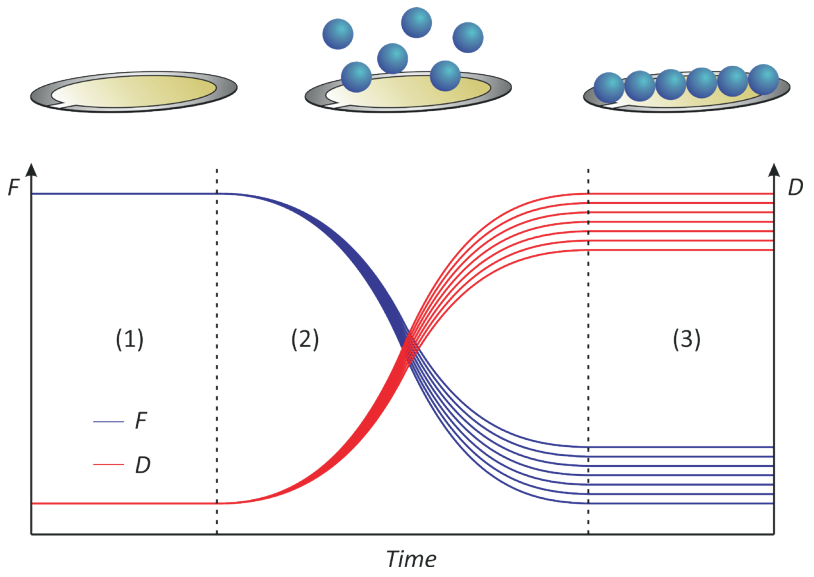

Figure 2.6. Experimental procedure of fouling experiments using QCM-D: Stabilization of the baseline in PBS buffer (1); adsorption of foulant onto the PA-coated QCM-D sensor (2); desorption step rinsing with PBS buffer (3). Blue lines represent the measured frequency while red lines represent the energy dissipation for different QCM-D harmonics.

In Chapter 5, once the irreversible foulant adsorption occured after desorption step, different cleaning agents were injected in order study their efficiency in removing organic fouling. Finally, a rinsing step was performed in order to see under reference conditions how much foulant was removed by the detergent.

2.7.2. Multi-Parameter Surface Plasmon Resonance (MP-SPR)

2.7.2.1. MP-SPR system

MP-SPR measurements were carried out using an MP-SPR from BIONAVIS (Finland). Same foulant and cleaning agent solutions as in QCM-D experiments were employed. Data were acquired and processed with the software "MP-SPR Navi Control" and "MP-SPR NaviData Viewer" (Bionavis, Finland), respectively.

2.7.2.2. MP-SPR sensors

MP-SPR sensors were composed of a glass slide coated with a thin metallic layer which in this case was gold (Figure 2.7). All the MP-SPR sensors were coated with the same polyamides used in QCM-D as described in Section 2.5.

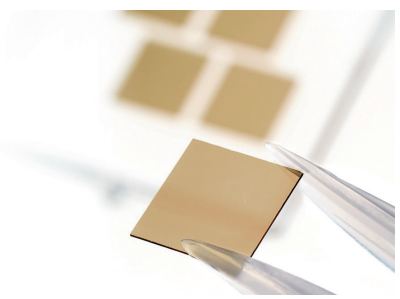

Figure 2.7. Example of an MP-SPR gold sensor [8].

2.7.2.3. Basic MP-SPR fundamentals

Multi-parametric surface plasmon resonance (MP-SPR) is an optical technique based on changes of the refractive index [9]. When a laser beam is projected onto the interface between the glass and gold layer of the MP-SPR sensor above the "critical angle", total in-

ternal reflection (TIR) occurs. Even though the light is not refracted under this condition, part of its energy penetrates the glass/gold interface creating the “evanescent field” into the gold layer. If the energy of this field is in resonance with the surface plasmons of the gold layer, then the latter are excited resulting in what can be seen as a minimum in the SPR curve at a given a resonance angle. This angle depends on the refractive index of the liquid adjacent to the gold surface and is highly sensitive to any changes. Therefore, when molecules are adsorbed on the gold surface, both the refractive index and resonance angle will change resulting in a shift of the minimum of the SPR curve which then can be correlated with the molecular adsorption phenomena (Figure 2.8).

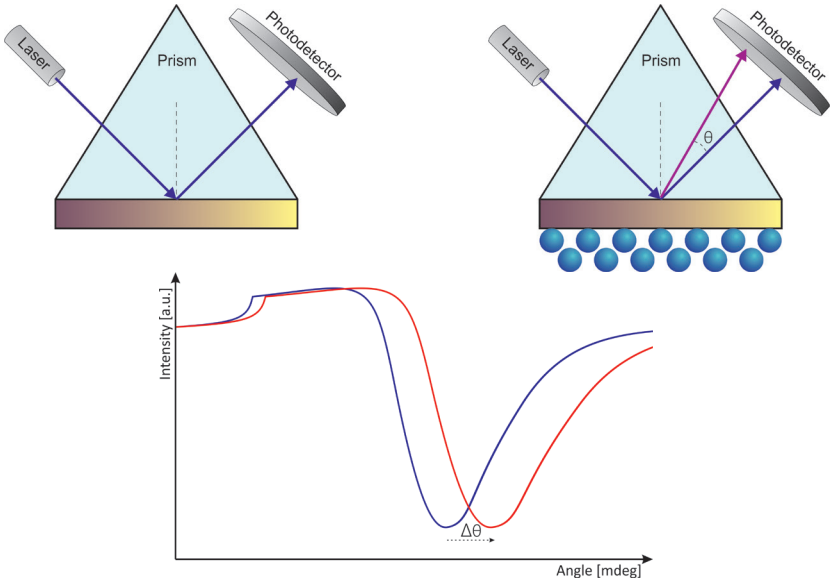

Figure 2.8. Working principle of the MP-SPR. Upper left: a laser beam is projected onto the interface between the glass and gold layer of the MP-SPR sensor and total internal reflection (TIR) occurs. Upper right: as foulant molecules adsorb onto the MP-SPR sensor surface, both the refractive index and the resonance angle change resulting in a shift of the minimum of the MP-SPR curve.

Based on Fresnel equations, MP-SPR enables a robust modelling in order to obtain the thickness and surface density of the adsorbed layer [10]. For proteins and when using a wavelength of 670 nm, the adsorbed mass per area may be approximately estimated equaling 0,833 ng/cm² to one millidegree of resonance angle change.

MP-SPR permits acquiring the whole SPR curve which enables many more parameters to be investigated (e.g. total internal reflection parameter, “TIR”) rather than only the curve minimum. Furthermore, the equipment used in this work operated with three different wavelengths (670, 785, and 980 nm, respectively) of different sensitivity. Increasing the wavelength, the sensitivity decreases. As the change of the refractive index is detected by the SPR depending on the wavelength used, this means that in this way three independent measurements were available for one and the same material-foulant interaction. When processing the resulting data in an interdependent manner using all the three wavelengths, a single solution of the foulant layer thickness can in principle be obtained.

The MP-SPR equipment used had two parallel “physical” flow channels over the MP-SPR sensor with each being adapted with two “optical” measurement channels. Throughout this thesis “Channel” will refer to the optical measurement channel. The signal of Channels 1 (670 nm) and 2 (785 nm) stemmed from one flow channel and the signal of Channels 3 (670 nm) and 4 (980 nm) from the other. The wavelength of 670 nm was

duplicated in either flow channel such as to add robustness to the measurements.

2.7.2.4. Fouling and cleaning experiments

All the fouling and cleaning experiments were carried following the same experimental procedure as in QCM-D measurements as described in Section 2.7.1.4. The flow velocity used during MP-SPR measurements was 50 µl/min.

2.8. Membrane fouling monitoring in a lab-scale and industrial RO plants (Chapter 6)

A proof of concept study of early-stage detection of membrane fouling was performed connecting the QCM-D equipment to a lab-scale cross-flow RO filtration plant. The RO plant used was provided by a local company (OTARI, Ingeniería del agua S.L., Irún, Spain). The produced water permeate flux was 3 m^3/day. RO membranes (Model: TW-PA-1812-100) were polyamide-based thin-film composite (PA-TFC) membranes provided by Sole Aqua (Taiwán) with a salt rejection of 99%. Experiments carried out using the lab-scale RO plant were accomplished recirculating feedwater with a total volume of 40 liters.

Once the proof of concept had been achieved, a pilot study was performed in an industrial setting (TRL 8). The industrial RO plant was operated by a major local company from the paper

sector. The RO membranes were PA-TFC membranes and the permeate water flux ranged from 60 to 65 m3/day. The pilot study lasted about 1 month.

2.9. References

[1] *S. Molina, P. Carretero, S.B. Teli, J.G. De la Campa, Á.E. Lozano, J. De Abajo, Hydrophilic porous asymmetric ultrafiltration membranes of aramid-g-PEO copolymers, J. Memb. Sci. 454 (2014) 233–242. https://doi.org/10.1016/j.memsci.2013.11.025.*

[2] *C. Procedures, Technical Service Bulletin, (2014) 1–16.*

[3] *Four-channel quartz crystal microbalance system Biolin Scientific | Quantum Design, (n.d.). https://qd-europe.com/fr/en/product/four-channel-quartz-crystal-microbalance-system/ (accessed March 15, 2022).*

[4] *M.C. Dixon, Quartz crystal microbalance with dissipation monitoring: Enabling real-time characterization of biological materials and their interactions, J. Biomol. Tech. 19 (2008) 151–158.*

[5] *P.L. Konash, G.J. Bastiaans, Piezoelectric crystals as detectors in liquid chromatography, Anal. Chem. 52 (1980) 1929–1931. https://doi.org/10.1021/ac50062a033.*

[6] *T. Nomura, M. Iijima, Electrolytic determination of nanomolar concentrations of silver in solution with a piezoelectric quartz crystal, Anal. Chim. Acta. 131 (1981) 97–102. https://doi.org/10.1016/S0003-2670(01)93538-X.*

[7] *G. Sauerbrey, Verwendung von Schwingquarzen zur Wägung dünner Schichten und zur Mikrowägung, Zeitschrift Für Phys. 155 (1959) 206–222. https://doi.org/10.1007/BF01337937.*

[8] *XanTec bioanalytics GmbH | Products | SPR Sensor chips, (n.d.). https://www.xantec.com/products/spr_sensorchips/index.php (accessed March 15, 2022).*

[9] *T. Viitala, N. Granqvist, S. Hallila, M. Raviña, M. Yliperttula, Elucidating the Signal Responses of Multi-Parametric Surface Plasmon Resonance Living Cell Sensing: A Comparison between Optical Modeling and Drug-MDCKII Cell Interaction Measurements, PLoS One. 8 (2013). https://doi.org/10.1371/journal.pone.0072192.*

[10] *H. Jussila, T. Albrow-Owen, H. Yang, G. Hu, S. Aksimsek, N. Granqvist, H. Lipsanen, R.C.T. Howe, Z. Sun, T. Hasan, New Approach for Thickness Determination of Solution-Deposited Graphene Thin Films, ACS Omega. 2 (2017) 2630–2638. https://doi.org/10.1021/acsomega.7b00336.*

CHAPTER 3

PREDICTION OF EARLY-STAGE MEMBRANE FOULING BY COMBINING QCM-D AND MP-SPR

3.1. Introduction

Freshwater is a natural resource that can be renewable, but due to increasing population growth and density local suppliers have difficulties to provide the necessary water not only in amount but also in quality [1]. There is therefore a strong need to provide technologies that could supply drinking water reliably and with high quality. Desalination of sea water based on membrane technologies such as reverse osmosis (RO) has become a promising way to face this challenge [2]. However, membrane fouling seriously affects the process efficiency and economics [3]. Several attempts have been made in order to reduce membrane fouling by modifying the membrane surface chemically [4,5]. One of the most common ways to do so is through grafting of hydrophilic polymeric chains onto the membrane surface in order to minimize the undesired adsorption of

molecules [6]. However, this strategy is limited by the low control over the grafting efficiency due to a heterogenous grafting density on the membrane surface.

One way to circumvent this shortcoming is to modify the respective monomers prior to polymerization [7]. Yet, rendering either the membrane surface or the polymer composition less prone to fouling often is based on a trial-and-error approach [8] requiring therefore a material-intensive and time-consuming screening. For optimizing desalination membrane materials, on one hand, and detect membrane fouling during the desalination process at an early stage such as to optimize membrane cleaning, on the other, robust on-line measurement techniques are needed that help turn the membrane water production processes more energy-efficient and sustainable.

Until today, some of the commonly reported fouling monitoring techniques such as direct observation trough membrane (DOTM) [9], electrical impedance spectroscopy [10], laser triangulometry [11], synchrotron IR spectroscopy [12], optical coherence tomography (OCT) [13], RAMAN and FTIR are indeed useful to study membrane fouling. However, they all have a limited sensitivity in common due to which they fail to detect how fouling develops at an early stage, starting from the very first adsorption layers. These layers form in the range of nanometers, roughly three orders of magnitude lower than the detection limit of common detection techniques. They have a predominant role during the fouling process as they change the

membrane surface properties and thus subsequently occurring interactions with the membrane surface. Another limitation of some of the aforementioned techniques is that they may not be robust enough for being implemented under harsh conditions on an industrial scale.

Within this context, a combination of quartz crystal microbalance with dissipation monitoring (QCM-D) and multi-parametric surface plasmon resonance (MP-SPR) was investigated as highly surface sensitive techniques for studying and predicting fouling phenomena. The aim was to establish a robust monitoring capable of detecting fouling from a nanometric scale onward, at an early stage, in real-time, and in a non-invasive manner.

Several studies reported in literature have employed either QCM-D or SPR on their own for studying membrane fouling on the laboratory scale using different membrane materials and model foulants [3,14–17]. Henmi and co-workers used SPR to study the fouling resistance of PVDF/PMMA-g-PEO MBR membranes of different lengths of PEO chains concluding that SPR would be useful for evaluating the fouling resistance of different membrane materials [18]. Other works employed SPR for studying the antifouling properties of different coatings for the biomedical field [19]. Polyethersulfone (PES) membrane-foulant interactions were previously studied by SPR in combination with Raman spectroscopy and molecular dynamics simulation [20]. A combination of model foulants has shown to cause a more severe damage into the filtration process [14,21–23].

QCM-D has been more widely employed for laboratory-scale fouling detection than SPR. Matsuyama and co-workers studied the fouling tendency of cellulose acetate butyrate (CAB) UF hollow fibre membranes when exposed to different model foulants. Their QCM-D experiments revealed that bovine serum albumin (BSA) was notably adsorbed at the CAB surface while alginate (ALG) and humic acid (HA) apparently did not adsorb at all. UF experiments confirmed that BSA was the most irreversibly adsorbed foulant and therefore the flux recovery was the lowest [24].

However, experimental evidence obtained by QCM-D may not always correlate with observations made during the membrane filtration process. For example, Wang and coworkers studied the adsorption of ALG and BSA on SiO2 coated sensors. They observed a strong interaction between BSA and silica which suggested strong propensity to fouling of silica membranes by BSA. Surprisingly, during corresponding filtration experiments the flux was apparently not affected [25].

One possible explanation for apparent contradictions between QCM-D and membrane filtration measurements could be that QCM-D as a sole fouling monitoring tool can be limited: it is known that QCM-D does not only measure the adsorption of foulants to the sensor surface but also the water molecules associated to the foulant (Figure 3.1). This amount of water may represent a significant fraction of the overall frequency (or mass) change detected. As a consequence, the real amount of adsorbed foulant

on the membrane surface would be strongly overestimated [26] by QCM-D, erroneously suggesting a high fouling propensity of the membrane surface. This is even more relevant as many common foulants such as proteins and polysaccharides are strongly hydrated when irreversibly adsorbing on the membrane surface.

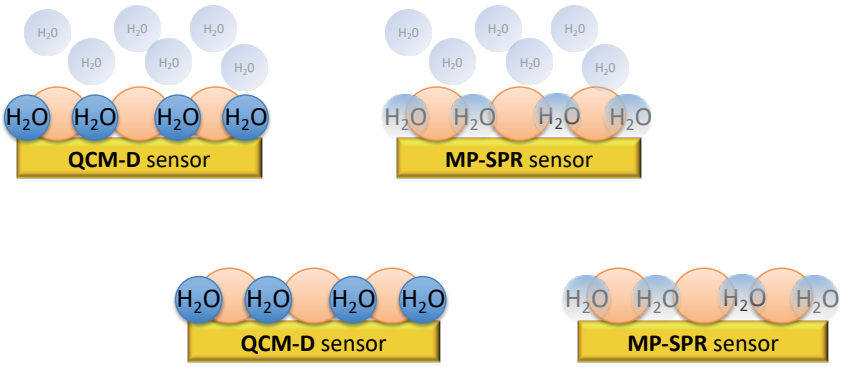

Figure 3.1. Sketch of how water molecules associated to foulants are perceived as an additional mass by QCM-D but not by MP-SPR.

SPR measurements, on the other hand, are not affected by water associated to surface-adsorbed foulants. The measurement concept of SPR is ultimately based on differences in refractive index [27]. As water possesses the same refractive index whether adsorbed to a surface foulant or whether in the bulk, it will not affect the SPR signal (Figure 3.1). Yet, both QCM-D and SPR have their potential advantages to characterize membrane fouling. The aim was therefore to demonstrate that it is indeed the combination of both QCM-D and SPR [28] that provides a unique, ro-

bust method for membrane fouling monitoring at an early stage and in real time. For this purpose, we employed polyamide (PA) modified to different degrees with polyethylene glycol (PEG) as a sensor surface layer and investigated its fouling by BSA.

3.2. Results and Discussion

3.2.1. Reproducibility and thickness of PA-PEG ultra-thin films

The aim of this study was to study fouling of a PA-modified sensor surface that should mimic the PA membrane surface of a reverse osmosis process. It was therefore indispensable to verify that the sensor polymer coating was indeed representative for the surface of a PA membrane as used in reverse osmosis (RO) [29]. Contreras et al. mimicked the surface of RO membranes by self-assembled monolayers (SAMs) [3,17]. However, this approach may bear the possible drawback of the surface not being entirely covered and, as a consequence, the contribution from the support (here: gold) will affect the measurements. In this work, spin-coating was therefore chosen as a quick and easy method for creating ultra-thin films of the membrane polymer on both the QCM-D and SPR sensors. Despite of spin-coating being a quick and easy method to generate ultra-thin films, the appropriate solvent and substrate surface chemistry for polymer deposition on QCM-D and SPR sensors needs to be found: apart from being a good solvent for the polymer, the solvent should wet the sensor surface and also be volatile enough such as to evaporate swiftly leaving behind an ultra-thin polymer film of reproducible properties.

The amount of polymer deposited was therefore determined for both techniques. As for QCM-D, and assuming that the ultra-thin PA film that has formed after drying could be considered “rigid”, the film thickness can be estimated according to the Sauerbrey equation (Eq. 2.1 on Chapter 2). As can be seen in Figure 3.2, except for pristine PA the average film thickness calculated was similar for all sensors and amounted to 50 nm (which according to Eq. 2.1 corresponds to a frequency shift of approximately 300 Hz) or above.

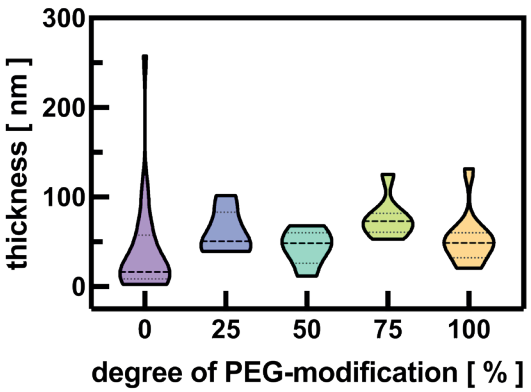

Figure 3.2. Violin-plot of the variation of the thickness of different PA-PEG films created by spin-coating and with increasing PEG content of PA.

Only pristine PA deposited not only has very thin films (average 10 nm) but also with a far higher dispersion of thickness values compared to the other polymers. Hence, the PEG modification apparently increased on one hand the adherence of the polymer solution to the sensor surface as well as the solubility of the PA in the solvent, resulting in thicker and more reproducible films.

Based on these data, for pristine PA the spin-coating protocol was adapted such as to warrant a deposition of always above 300 Hz.

It is commonly known that adsorption of molecules to a membrane surface is governed by the membrane surface topography, surface chemistry, and hydrophilicity [30]. We therefore investigated first these parameters prior to actual adsorption measurements.

3.2.2. Surface topography of the PA-PEG ultra-thin films

Ideally, the surface topography of the polymer-modified sensors would have to be sufficiently reproducible such as no to interfere with the subsequent adsorption measurements. AFM experiments were conducted in both air and liquid (PBS buffer) conditions in order to see how the polymer film surface remained after spin-coating and whether increasing the content of PEG had any effect on the PA surface topography. Figure 3.3 illustrates that while unmodified PA possessed a rather smooth surface according to AFM measurements in air, the surface became much rougher upon introduction of PEG, being PA-PEG75 the one which highest roughness (Table 3.1).

In fact, in air, PA-PEG75 possessed an about 30 times higher surface roughness than pristine PA. Considering that this increased surface roughness would result in a larger surface area, it would therefore be expected that the measured adsorption of foulants could potentially be overestimated for PA-PEG75.

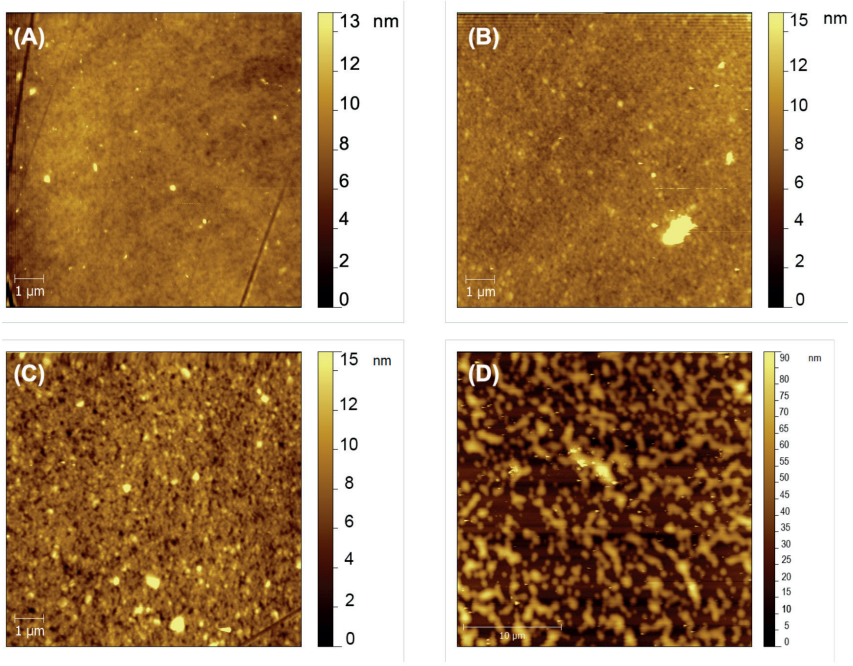

Figure 3.3. AFM images of the surface of PEG-modified PA films in air: **(A)** unmodified PA; **(B)** PA-PEG25; **(C)** PA-PEG50; **(D)** PA-PEG75.

Table 3.1. Roughness values Ra and Rq of PA-PEG films as determined in air.

sample	PEG content	Ra	Rq
	[%]	[nm]	[nm]
PA	**0**	0,7±0,1	1,2±0,4
PA-PEG25	**25**	1,7±0,7	12,8±5,2
PA-PEG50	**50**	1,5±0,1	4,2±2,5
PA-PEG75	**75**	20,5±7,2	36,3±21,9

On the other hand, AFM measurements in PBS buffer revealed that the surface topography was not only lower (Table 3.2) than in air but also slightly decreased with increasing degree of modification. All AFM images in buffer showed a comparatively rather smooth surface irrespective of the degree of PEG-modification (Figure 3.4). One might argue that the topography of PA-PEG75 reveals some more apparent “aggregations” visible as white spots. However, it is emphasized that these features are more extended in area rather than in height as can clearly be confirmed by the scale adjacent to the images. As shown by the data in Table 3.2, they furthermore did not result in a significant change in average surface roughness for PA-PEG75, as opposed to what was observed in air. This demonstrates the importance of conducting AFM characterization under actual experimental conditions.

The decreased surface roughness with increasing polymer modification by dangling hydrophilic side chains does not necessarily go along with an increase in surface roughness. K. Gleason et al. performed AFM measurements in air conditions on RO membranes with zwitterionic coating. They observed a decreased surface roughness with increasing the membrane modification, resulting in a smoother surface which proved less prone to protein adsorption [31]. A similar observation was made by Matsuyama et al. with multi-layered polyelectrolyte-modified RO membranes. As the number of layers increased, they also observed a significant reduction of the surface roughness expecting less protein adsorption [32].

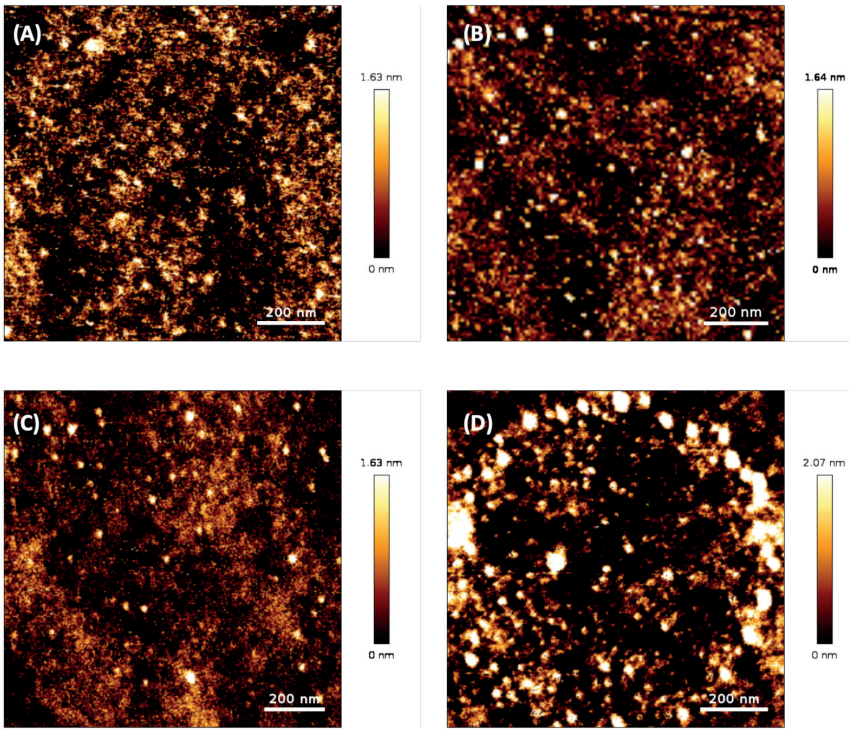

Figure 3.4. AFM images of the surface of PEG-modified PA films in PBS buffer: **(A)** unmodified PA; **(B)** PA-PEG25; **(C)** PA-PEG50; **(D)** PA-PEG75.

Table 3.2. Roughness values Ra and Rq of PA-PEG films as determined by AFM in PBS buffer.

sample	PEG content [%]	Ra [nm]	Rq [nm]
PA	**0**	0,6±0,4	2,5±2,2
PA-PEG25	**25**	0,6±0,2	1,2±0,5
PA-PEG50	**50**	0,5±0,3	0,9±1,1
PA-PEG75	**75**	0,4±0,02	0,5±0,02

Based on these AFM measurements it could be stated that the surface topography was in the same order of magnitude for all polymers with a tendency toward slightly smoother surfaces as the PEG content increased. However, taking into account the order of magnitude of the surface roughness in buffer (Ra<1nm) and within the standard deviation of the measurements these differences could be considered of minor significance and the surface topography of all surfaces assumed very similar.

3.2.3. Surface chemistry and contact angle of the PA-PEG ultra-thin films

The surface chemistry of the ultra-thin PA films was investigated by XPS. Using the chemical structure of the unmodified polyamide, the theoretical content of carbon and oxygen elements was calculated for each PEG-modified polyamide as a reference. Figure 3.5 depicts both the theoretically expected and measured content of carbon and oxygen of each PA-PEG film based on the polymer chemical structure (see Figure 2.1).

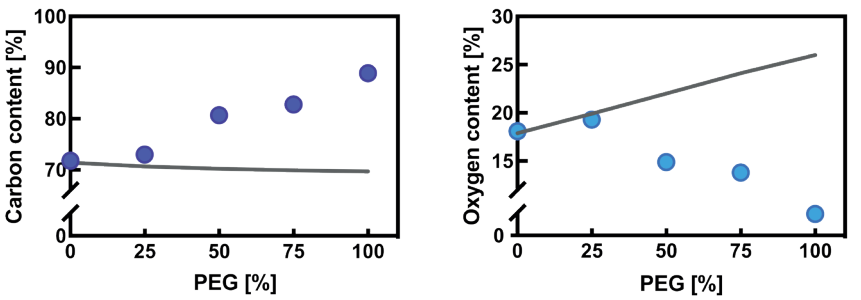

Figure 3.5. Left: Carbon content determined by XPS for PA-PEG films: theoretical content (straight line) and experimental data (purple circles). **Right:** Oxygen content determined by XPS for PA-PEG films: theoretical content (straight line) and experimental data (blue circles).

For unmodified polyamide (0% PEG), the predicted carbon and oxygen content is in excellent agreement with the experimentally determined values. However, upon increasing the percentage of PEG, the deviation between predicted and experimentally determined content for carbon and oxygen, respectively, deviates increasingly. A possible explanation can be a rearrangement of the polymer such as to expose the more hydrophobic moieties to the surface during solvent evaporation and given that the measurements were conducted in vacuum and, thus, absence of water [33]. Contact angle (CA) measurements widely confirmed this observation. Table 3.3 lists the water CA values measured for the different PA-PEG films. As opposed to what could be expected and was reported [7], water contact angles slightly increase with growing PEG-content of the polyamides. The water contact angle remains for all samples below 90∞ indicating a hydrophilic surface, however, the carbon content as determined by XPS and the CA measured for the ultra-thin films correlate very well, except for PA-PEG100 (Figure 3.6). In this latter case, it was noticed that the polymer was not stable upon prolonged contact with water, a reason for which PA-PEG100 was excluded from subsequent experiments.

Table 3.3. Water contact angle measured for PA-PEG films.

sample	PEG content [%]	Water contact angle [°]
PA	0	70,2±0,2
PA-PEG25	25	74,9±0,2
PA-PEG50	50	78,8±1,1
PA-PEG75	75	82,3±0,9
PA-PEG100	100	80,6±0,9

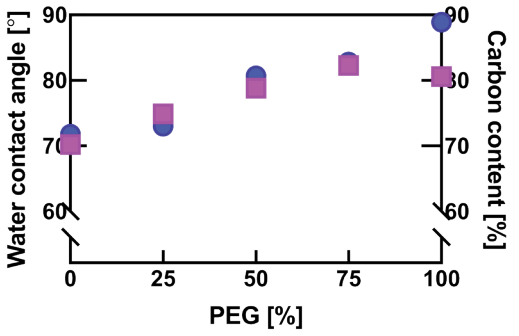

Figure 3.6. Water contact angle (pink squares) and experimental carbon content determined by XPS (purple dots) as a function of the degree of PEG-modification of PA.

In summary, experimental results based on XPS and CA would suggest a slight increase in hydrophobicity of the ultra-thin polyamide film surface upon gradual incorporation of PEG-moieties and, hence, slightly increased fouling tendency. This is the opposite of what would be expected as the incorporation of PEG units made the polyamide more hydrophilic according to previous measurements of water uptake and water contact angle [7].

We therefore verified with QCM-D and MP-SPR measurements whether the PA layers would indeed be more prone to fouling upon increasing the PEG content.

3.2.4. BSA adsorption on PA-PEG as determined by QCM-D

Using bovine serum albumin (BSA) as a model foulant for all aforementioned PEG-modified polyamides, a typical QCM-D analysis is depicted in Figure 3.7A. After a stabilization of the ultra-thin films in buffer, the time when BSA adsorption reaches stationary state (here: within 10 minutes) can be clearly identified. Contrary to what results obtained by XPS and water CA suggested, a clear anti-fouling contribution of PEG is identified: unmodified polyamide adsorbs BSA most while PA-PEG75 reduces the adsorption of BSA by almost 83 % (Figure 3.7B) confirming previous studies using similar membrane surface modifications [5,34]. Upon rinsing again with buffer (denoted as “desorption” in Figure 3.7A), a rise in frequency was observed indicating desorption of loosely bound BSA. This rise was 6,6%; 7,4%; 13,7%; and 28,5% for PA-PEG0; PA-PEG25; PA-PEG50; and PA-PEG75, respectively. PEG-modification therefore did not only diminish BSA adsorption but also weaken the interaction of the BSA with the PA surface. For membrane applications involving PA, this means that highest PEG-contents would not only decrease membrane fouling in the first place but also help removing fouling during water flushing and membrane cleaning.

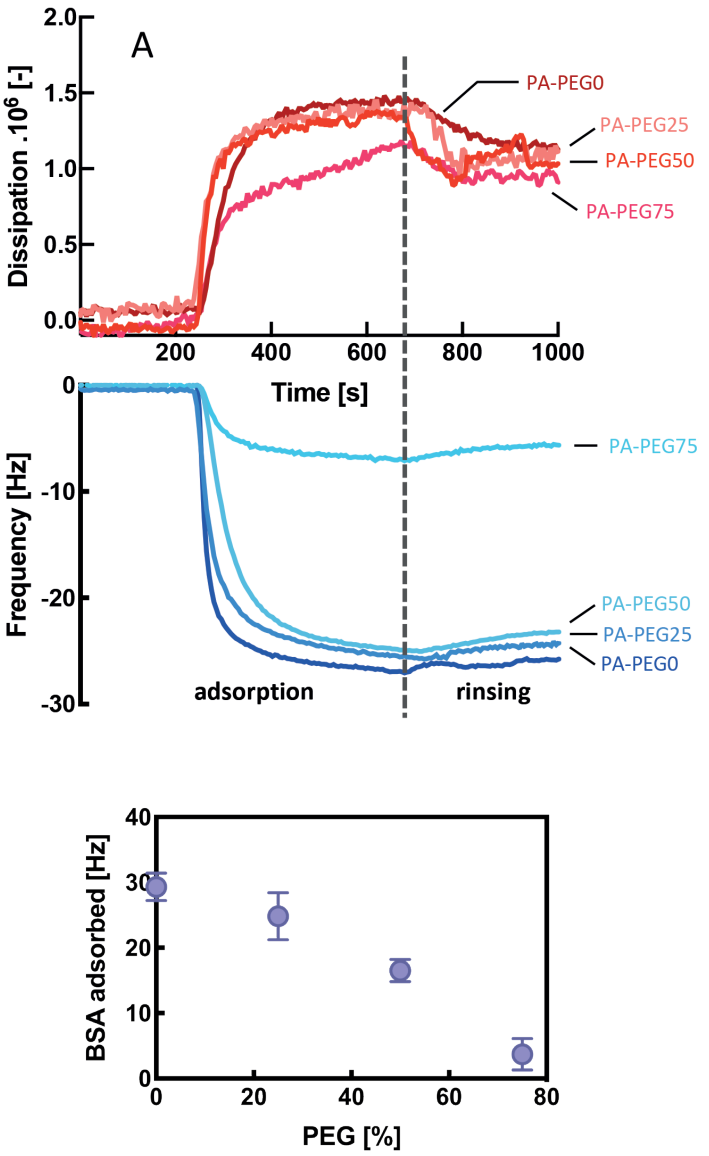

Figure 3.7A. Typical BSA adsorption/desorption experiment on polyamides modified to different degrees with PEG and monitored by QCM-D. **3.7B**. Average of steady-state values of BSA adsorption on PEG-modified polyamides as determined by QCM-D. The error bar represents the standard deviation of the mean.

3.2.5. Study of the viscoelasticity of the adsorbed BSA protein layer on PA-PEG films

The dissipation factor D is commonly associated with the "rigidity" or "softness" of the adsorbed layer and therefore holds information on the adsorbed layer properties which are particularly valuable for a membrane filtration process. For example, the same mass of a foulant can affect to a different degree membrane fouling depending on the foulant's density: what would be detected in QCM-D as a "softer" or more viscoelastic mass may generate a fouling with a more severe impact than the same mass but more "rigidly" attached (Figure 3.8).

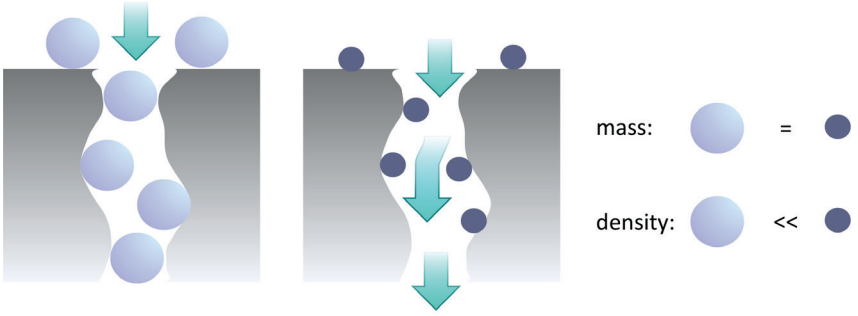

Figure 3.8. Sketch illustrating how the same mass of a foulant can differently affect the membrane process depending on the foulant's density. A softer, "spongy" adsorption layer **(left)** may diminish water flux to a higher degree than a denser, more condensed adsorbed layer **(right)** of the same mass.

This can be clearly demonstrated in the context of the simple model fouling system chosen for this study. Figures 3.9A and 3.9C depict the time-dependent frequency and dissipation for the 5th harmonic during BSA adsorption and subsequent rinsing on PA-PEG0 and PA-PEG75, respectively. Eliminating time as a parameter from these data, the dissipation is plotted in Figures 3.9B and 3.9D versus its respective frequency, i.e., the mass adsorbed on the membrane polymer surface.

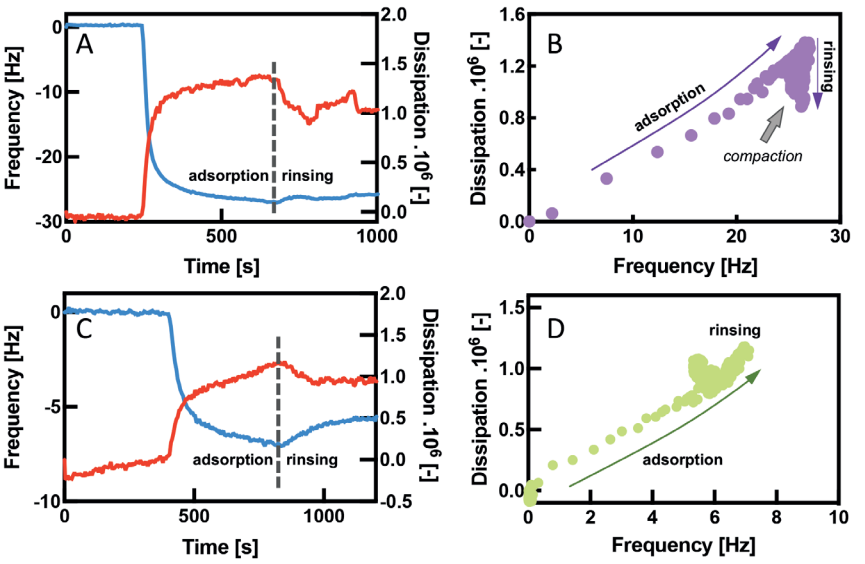

Figure 3.9A,C. Raw data of the adsorption of BSA on PA-PEG0 and PA-PEG75, respectively, as monitored by QCM-D; **B**, **D:** Representation of the raw data in a dissipation-frequency plot such as to illustrate changes in the viscoelasticity of the adsorbed BSA layer on PA-PEG0 and PA-PEG75, respectively.

It can be seen that while for both PA-PEG0 and PA-PEG75 the dissipation increases with incremental frequency during the adsorption of BSA, rinsing with buffer results in a compaction (decrease in dissipation at minor change of frequency) of the BSA layer formed in the case of PA-PEG0 and softening in the case of PA-PEG75. In a membrane process, the “rinsing” step would correspond to water flushing which according to these results would compress the protein fouling layer in the case of unmodified PA and in the case of PA-PEG75 loosen it slightly. The steady-state ratio between frequency and dissipation (ΔD/ΔF) during “rinsing” reveals whether the protein (BSA) is attached to the PA surface as a more rigid or soft layer. In accordance with the aforementioned, data depicted in Figures 3.10A and 3.10B demonstrate that BSA adsorbed with increasingly “softer” layers on the PA surface with increasing PEG-content. Particularly in case of PA-PEG75, the high ratio of ΔD/ΔF results from both a low ΔF and a high ΔD. BSA does, hence, not only adsorb least in this case, but also forms significantly softer adsorption layers as compared to the other polyamides. This could possibly be due to the PEG chains acting as flexible brush-like filaments that hinder BSA from adsorbing in a more compact manner. The ΔD/ΔF ratio can, hence, be used as a predictive parameter for the membrane cleaning efficiency in a membrane filtration process.

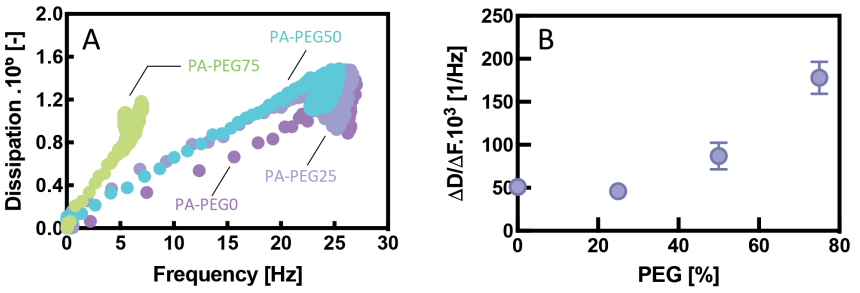

Figure 3.10A. Change of dissipation "D" as a function of the change of frequency "F" with incremental increase of the PEG-content of polyamides. **3.10B.** ΔD/ΔF ratio change as a function of the degree of PEG-modification of the polyamides. Data for ΔD/ΔF were taken from the water rinsing step after adsorption.

3.2.6. BSA adsorption on PA-PEG films as determined by MP-SPR and complementarity with QCM-D

MP-SPR differs from QCM-D inasmuch as it is an optical technique based on changes of the refractive index. However, the sensors employed in both MP-SPR and QCM-D can share the same sensor surface material which facilitates a direct comparison of results obtained by both techniques. Just as in QCM-D, the real-time kinetics of foulant interactions with the PEG-modified PA is monitored by MP-SPR, in this case following the shift in resonance angle (Figure 3.11A). Figure 3.11B depicts how the fouling tendency detected is in fact very similar to that of QCM-D: with increasing PEG content of the PA the BSA adsorption decreases.

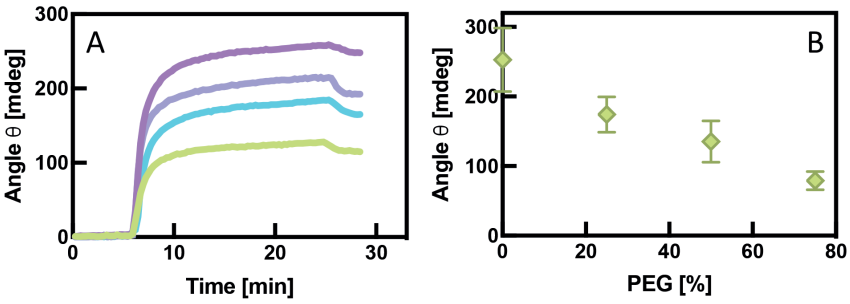

Figure 3.11A. MP-SPR response (using the wavelength of 670 nm) of adsorption of BSA on different PA-PEG films, PA-PEG0 (pink curve); PA-PEG25 (purple curve); PA-PEG50 (blue curve); PA-PEG75 (green curve); **3.11B.** MP-SPR resonance angle change due to adsorption of BSA on the same PA-PEG films as in A.

Normalizing the BSA adsorption data determined by both QCM-D and MP-SPR in relation to the adsorption measured at PA-PEG0, it becomes evident that although data from both techniques follow the same tendency, minor differences are observed for PA-PEG25 and PA-PEG75 where QCM-D detects a slightly higher and lower amount of BSA adsorbed, respectively, than MP-SPR (Figure 3.12). Frequency and angle changes as measured by QCM-D and MP-SPR, respectively, can be converted approximately into adsorbed masses per area or surface densities. Figure 3.12B illustrates that QCM-D detects a 2,5-fold higher total adsorbed mass per area than MP-SPR for the pristine PA while with increasing PEG content this difference becomes smaller and vanishes for PA-PEG-75. QCM-D measures the “wet mass” of the protein, i.e. the protein and its associated water. MP-SPR, on the other hand, is based on optical properties and as the as-

sociated water of the protein has the same refractive index as the bulk water, it only will sense the "dry" protein mass. Figure 3.12B therefore suggests that the hydration regime of BSA is entirely different between PA-PEG0 (highly hydrated) and PA-PEG75 (low hydration) which could be explained by different conformations which BSA undergoes on both surfaces. It is noteworthy that in the latter case the agreement between QCM-D and MP-SPR is excellent.

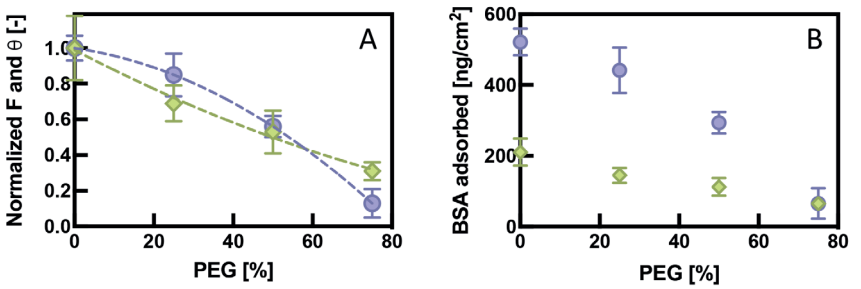

Figure 3.12A. Normalized values of BSA adsorption data for PEG-modified polyamides as determined by QCM-D (purple circles) and MP-SPR (green diamonds). **B:** BSA adsorbed mass on PEG-modified polyamides estimated from QCM-D (purple circles) and MP-SPR (green diamonds).

This example highlights the benefit of using both QCM-D and MP-SPR in combination as a fouling monitoring technique. For highly hydrated fouling layers, QCM-D might strongly overestimate membrane fouling and MP-SPR appears to yield far more reliable results as regards the foulant "dry" mass. This is particularly relevant when one aims at elucidating the fouling tendency of different compounds and/or membrane surfaces. On the oth-

er hand, during membrane filtration information on the hydrated fouling layer as measured by QCM-D might be of interest since pore blocking would most probably be more adequately described considering the hydrated rather than the dry foulant (as sketched in Figure 3.8). Moreover, the ΔD/ΔF ratio as a measure of the fouling layer viscoelasticity provided by QCM-D yields valuable insights into the rigidity of the layer which could ultimately be related to the ease of membrane cleaning.

3.2.7. Modelling of the BSA layer thickness on PA

A BSA molecule in aqueous solution has been reported to have the approximate dimension of 4 nm x 4 nm x 14 nm [35] such that its adsorption can occur either upright (height 14 nm) or lying down (height 4 nm). The area occupied by one BSA molecule is then 16 nm^2 and 56 nm^2, respectively. With an effective QCM-D sensor surface of approximately 1 cm^2, the Avogadro constant ($6{,}02 \cdot 10^{23}$ mol^{-1}) and molecular weight of BSA of 66,5 kDa, the mass of a BSA monolayer entirely covering the sensor surface is calculated to be 693 ng (BSA upright) and 198 ng (BSA lying down). Using the Sauerbrey equation (Eq. 2.1), the respective maximum frequencies are determined to be 39,2 Hz (upright) and 11,2 Hz (lying down) and based entirely on a theoretical calculation involving the geometry of a single BSA molecule.

For pristine PA with a maximum BSA adsorption (Figure 3.12B), MP-SPR measured a “dry” mass of BSA adsorbed of approximately 200 $ng \cdot cm^{-2}$ which would translate into 11,3 Hz using the Sauerbrey equation for QCM-D. At the BSA concentration used

in buffer (100 ppm), the surface coverage of PA is close to maximum (Figure 3.13). As a consequence, the excellent agreement between MP-SPR data and the theoretical calculation hint at BSA adsorbing apparently in the “lying down” mode which would suggest a layer thickness of around 4 nm.

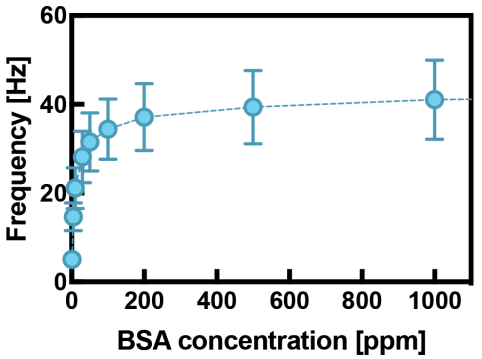

Figure 3.13. Adsorption isotherm of BSA on PA-PEG0. The concentration of the BSA in solution ranged from 1 ppm to 1000 ppm.

Assuming that pristine PA was almost entirely covered by BSA, we investigated in how far QCM-D and MP-SPR would be able to fit the BSA layer thickness. QCM-D acquires data on two independent variables simultaneously (different harmonics of frequency F and dissipation D) from which therefore not only the mass adsorption can be retrieved but also one further parameter such as the layer thickness. Using the raw QCM-D frequency and dissipation data, the thickness of the BSA layer adsorbed on pristine PA was determined by using the Sauerbrey model for a rigid layer and Voigt model for a viscoelastic layer, respectively. The modelled

layer thickness based on QCM-D data was 6 nm and 7 nm, hence, in reasonable agreement with the expected thickness of 4 nm.

Common SPR measures only one parameter (resonance angle shift) and can, hence, provide direct information only on one variable (surface coverage). The MP-SPR employed in this study was measuring with three different wavelengths (670nm, 785 nm, and 980 nm, respectively) yielding three independent data points per measurement and allowing, hence, for determining thickness as an additional variable apart from the surface coverage.

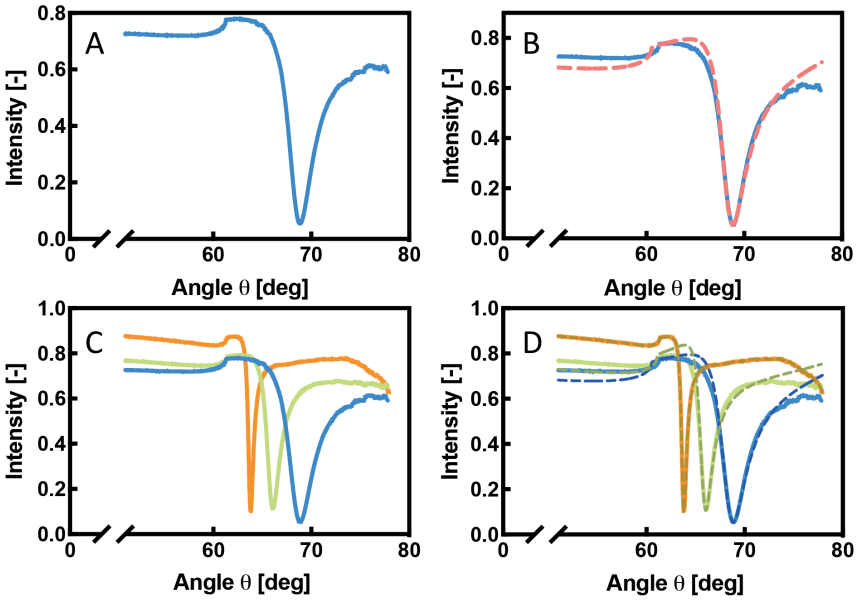

Figure 3.14. Modelling of MP-SPR data. Raw data using a single wavelength of 670 nm **(A)**, and corresponding fit **(B)**; raw data using three different wavelengths **(C)**: 670 nm (blue), 785 nm (green), 980 nm (orange), and corresponding interdependent fit **(D)**.

A thickness value of 1.6 nm was obtained when fitting the SPR curve obtained by protein adsorption with one wavelength (Figure 3.14A and 3.14B). This value is significantly lower than the minimum expected height of 4 nm. The issue with a single wavelength measurement is that there exist several possible combinations of refractive index and layer thickness which describe the same SPR curve because the system is underdetermined. As a consequence, only an approximate solution can be found. This shortcoming is overcome by working with three wavelengths instead of only one. Because the change of the refractive index depends on the wavelength, three independent measurements are available for one and the same data point such that three independent SPR-curves are obtained during one measurement (Figure 3.14C). Fitting the same data as before in an interdependent manner using all three wavelengths (Figure 3.14D) by means of LayerSolver software resulted in a single solution of about 4 nm. This value is exactly the size of the expected monolayer of BSA when lying down on the PA surface. Hence, a very good agreement was found between theoretical calculation and modelling, particularly using MP-SPR. Results so obtained are particularly useful for fouling characterization in membrane processes as knowledge of the layer thickness permits mass transfer modelling and subsequently process optimization.

3.2.8. Correlation between filtration process and QCM-D/MP-SPR data

We conducted a proof-of-concept study of a combined QCM-D/MP-SPR early stage detection of membrane fouling. For this purpose, we correlated results from a laboratory scale ultrafiltration (UF) [7] using membranes composed of the very same PEG-modified polyamides as studied in this work with our data from QCM-D and MP-SPR. The experimental conditions for the UF were the same as during QCM-D and MP-SPR experiments, using BSA as a model foulant. After fouling by BSA during UF the membranes were flushed with water for 15 minutes in order to desorb reversibly bound BSA, very similarly to what was done during our QCM-D and MP-SPR measurements (denoted as "rinsing" in Figure 3.7A). Subsequently, water flux recovery of the UF process was measured [7] with 100% indicating the flux of the pristine membranes. We used these data as a reference converting them into loss of water flux by simply applying: loss of water flux [%] = 100% - flux recovery [%]. The respective UF data could then be directly correlated with data from QCM-D (Figure 3.7B) and MP-SPR (Figure 3.11B) after rinsing.

Figure 3.15A illustrates the agreement between UF loss of water flux and QCM-D data (taken from Figure 3.7B). As can be observed, the correlation was excellent. Figure 3.15B shows that MP-SPR data correlated very well with data of UF loss of water flux with exception of the data point for PA-PEG75. It is recalled that QCM-D measures the hydrated mass of BSA adsorbed whilst MP-SPR measures only the "dry" mass. Given that UF membranes are porous, a sit-

uation like the one sketched in Figure 3.8 (left) most probably applies where it is the total mass of BSA (protein + associated water) that determines the impact of the fouling layer – hence, the excellent correlation with the QCM-D data. For non-porous membranes, however, QCM-D would most likely overestimate the fouling and a better correlation would be obtained with MP-SPR. It is thus the combination of both highly complementary techniques that provide a robust fouling monitoring of membrane separation processes.

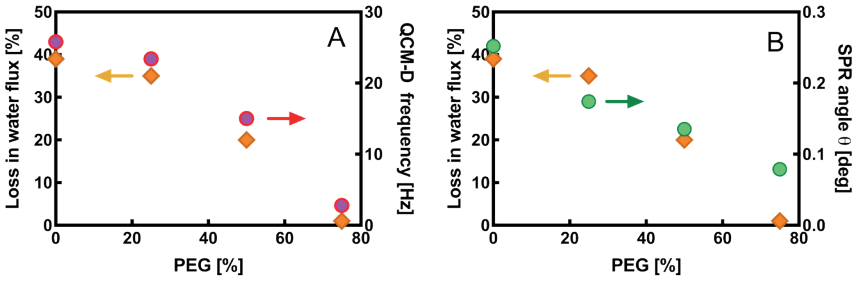

Figure 3.15. Correlation between the loss of water flux during UF [7] and (A) QCM-D data and (B) MP-SPR data as a function of the PEG content of PA.

3.3. Conclusions

A highly sensitive monitoring method for detecting membrane fouling at an early-stage has been reported. The method is based on a combination of QCM-D and MP-SPR. Using PA-PEG membrane polymers and BSA as a model foulant, both QCM-D and MP-SPR allowed measuring adsorption phenomena not only in real-time but the combined data could also be correlated with fouling phenomena in the respective membrane filtration process. The reported method provides the opportunity to determine the thickness of the fouling layer by a modelling of the acquisition raw data. It was found that multiple wavelength MP-SPR provides information on fouling layer thickness in a more reliably way than QCM-D. The latter, however, yields information on viscoelasticity of the adsorbed fouling film which can be correlated with the density of the membrane fouling layer. This information may allow an optimization of membrane cleaning protocols. Therefore, the combination of both QCM-D and MP-SPR is a very useful tool for predicting membrane fouling at an early-stage and in this way minimize its impact on the membrane filtration process.

3.4. References

[1] *A. Subramani, J.G. Jacangelo, Emerging desalination technologies for water treatment: A critical review, Water Res. 75 (2015) 164–187. https://doi.org/10.1016/j.watres.2015.02.032.*

[2] *M.E.A. Ali, L. Wang, X. Wang, X. Feng, Thin film composite membranes embedded with graphene oxide for water desalination, Desalination. 386 (2016) 67–76. https://doi.org/10.1016/j.desal.2016.02.034.*

[3] *J. Wu, A.E. Contreras, Q. Li, Studying the impact of RO membrane surface functional groups on alginate fouling in seawater desalination, J. Memb. Sci. 458 (2014) 120–127. https://doi.org/10.1016/j.memsci.2014.01.056.*

[4] *A. Akbari, E. Aliyarizadeh, S.M. Mojallali Rostami, M. Homayoonfal, Novel sulfonated polyamide thin-film composite nanofiltration membranes with improved water flux and anti-fouling properties, Desalination. 377 (2016) 11–22. https://doi.org/10.1016/j.desal.2015.08.025.*

[5] *B.P. Tripathi, N.C. Dubey, M. Stamm, Polyethylene glycol cross-linked sulfonated polyethersulfone based filtration membranes with improved antifouling tendency, J. Memb. Sci. 453 (2014) 263–274. https://doi.org/10.1016/j.memsci.2013.11.007.*

[6] *F. Poncin-Epaillard, T. Vrlinic, D. Debarnot, M. Mozetic, A. Coudreuse, G. Legeay, B. El Moualij, W. Zorzi, Surface Treatment of Polymeric Materials Controlling the Adhesion of Biomolecules, J. Funct. Biomater. 3 (2012) 528–543. https://doi.org/10.3390/jfb3030528.*

[7] *S. Molina, P. Carretero, S.B. Teli, J.G. De la Campa, Á.E. Lozano, J. De Abajo, Hydrophilic porous asymmetric ultrafiltration membranes of aramid-g-PEO copolymers, J. Memb. Sci. 454 (2014) 233–242. https://doi.org/10.1016/j.memsci.2013.11.025.*

[8] *N. Misdan, A.F. Ismail, N. Hilal, Recent advances in the development of (bio) fouling resistant thin film composite membranes for desalination, Desalination. 380 (2016) 105–111. https://doi.org/10.1016/j.desal.2015.06.001.*

[9] *H. Li, A.G. Fane, H.G.L. Coster, S. Vigneswaran, Direct observation of particle deposition on the membrane surface during crossflow microfiltration, J. Memb. Sci. 149 (1998) 83–97. https://doi.org/10.1016/S0376-7388(98)00181-1.*

[10] *L. Gaedt, T.C. Chilcott, M. Chan, T. Nantawisarakul, A.G. Fane, H.G.L. Coster, Electrical impedance spectroscopy characterisation of conducting membranes II. Experimental, J. Memb. Sci. 195 (2002) 169–180. https://doi.org/10.1016/S0376-7388(01)00542-7.*

[11] J. Altmann, S. Ripperger, Particle deposition and layer formation at the crossflow microfiltration, J. Memb. Sci. 124 (1997) 119–128. https://doi.org/10.1016/S0376-7388(96)00235-9.

[12] M. Xie, W. Luo, S.R. Gray, Synchrotron Fourier transform infrared mapping: A novel approach for membrane fouling characterization, Water Res. 111 (2017) 375–381. https://doi.org/10.1016/j.watres.2017.01.020.

[13] L. Fortunato, A. Qamar, Y. Wang, S. Jeong, T.O. Leiknes, In-situ assessment of biofilm formation in submerged membrane system using optical coherence tomography and computational fluid dynamics, J. Memb. Sci. 521 (2017) 84–94. https://doi.org/10.1016/j.memsci.2016.09.004.

[14] A.E. Contreras, A. Kim, Q. Li, Combined fouling of nanofiltration membranes : Mechanisms and effect of organic matter, 327 (2009) 87–95. https://doi.org/10.1016/j.memsci.2008.11.030.

[15] W. Ying, N. Siebdrath, W. Uhl, V. Gitis, M. Herzebrg, New insights on early stages of RO membranes fouling during tertiary wastewater desalination, J. Memb. Sci. 466 (2014) 26–35. https://doi.org/10.1016/j.memsci.2014.04.027.

[16] A. Sweity, W. Ying, M.S. Ali-Shtayeh, F. Yang, A. Bick, G. Oron, M. Herzberg, Relation between EPS adherence, viscoelastic properties, and MBR operation: Biofouling study with QCM-D, Water Res. 45 (2011) 6430–6440. https://doi.org/10.1016/j.watres.2011.09.038.

[17] A.E. Contreras, Z. Steiner, J. Miao, R. Kasher, Q. Li, Studying the role of common membrane surface functionalities on adsorption and cleaning of organic foulants using QCM-D, Environ. Sci. Technol. 45 (2011) 6309–6315. https://doi.org/10.1021/es200570t.

[18] H. Minehara, K. Dan, Y. Ito, H. Takabatake, M. Henmi, Quantitative evaluation of fouling resistance of PVDF/PMMA-g-PEO polymer blend membranes for membrane bioreactor, J. Memb. Sci. 466 (2014) 211–219. https://doi.org/10.1016/j.memsci.2014.04.039.

[19] C. Xing, F. Meng, M. Quan, K. Ding, Y. Dang, Y. Gong, Acta Biomaterialia Quantitative fabrication , performance optimization and comparison of PEG and zwitterionic polymer antifouling coatings, Acta Biomater. 59 (2017) 129–138. https://doi.org/10.1016/j.actbio.2017.06.034.

[20] T. Virtanen, P. Parkkila, A. Koivuniemi, J. Lahti, T. Viitala, M. Kallioinen, M. Mänttäri, A. Bunker, Separation and Puri fi cation Technology Characterization of membrane – foulant interactions with novel combination of Raman spectroscopy , surface plasmon resonance and molecular dynamics simulation, Sep. Purif. Technol. 205 (2018) 263–272. https://doi.org/10.1016/j.seppur.2018.05.050.

[21] M.M. Motsa, B.B. Mamba, A.R.D. Verliefde, Combined colloidal and organic fouling of FO membranes: The influence of foulant-foulant interactions and ionic strength, J. Memb. Sci. 493 (2015) 539–548. https://doi.org/10.1016/j.memsci.2015.06.035.

[22] A.H. Taheri, L.N. Sim, C.T. Haur, E. Akhondi, A.G. Fane, The fouling potential of colloidal silica and humic acid and their mixtures, J. Memb. Sci. 433 (2013) 112–120. https://doi.org/10.1016/j.memsci.2013.01.034.

[23] M. Ali, S. Nasseri, M. Ulbricht, Fouling effects of humic and alginic acids in nano fi ltration and in fl uence of solution composition, 250 (2010) 688–692. https://doi.org/10.1016/j.desal.2009.05.021.

[24] M. Hashino, K. Hirami, T. Katagiri, N. Kubota, Y. Ohmukai, T. Ishigami, T. Maruyama, H. Matsuyama, Effects of three natural organic matter types on cellulose acetate butyrate microfiltration membrane fouling, J. Memb. Sci. 379 (2011) 233–238. https://doi.org/10.1016/j.memsci.2011.05.068.

[25] E. Arkhangelsky, F. Wicaksana, C. Tang, A.A. Al-Rabiah, S.M. Al-Zahrani, R. Wang, Combined organic-inorganic fouling of forward osmosis hollow fiber membranes, Water Res. 46 (2012) 6329–6338. https://doi.org/10.1016/j.watres.2012.09.003.

[26] F. Höök, B. Kasemo, T. Nylander, C. Fant, K. Sott, H. Elwing, Variations in coupled water, viscoelastic properties, and film thickness of a Mefp-1 protein film during adsorption and cross-linking: A quartz crystal microbalance with dissipation monitoring, ellipsometry, and surface plasmon resonance study, Anal. Chem. 73 (2001) 5796–5804. https://doi.org/10.1021/ac0106501.

[27] E. Reimhult, C. Larsson, B. Kasemo, F. Höök, Simultaneous surface plasmon resonance and quartz crystal microbalance with dissipation monitoring measurements of biomolecular adsorption events involving structural transformations and variations in coupled water, Anal. Chem. 76 (2004) 7211–7220. https://doi.org/10.1021/ac0492970.

[28] K. Otto, Biophysical approaches to study the dynamic process of bacterial adhesion, Res. Microbiol. 159 (2008) 415–422. https://doi.org/10.1016/j.resmic.2008.04.007.

[29] Z. Steiner, J. Miao, R. Kasher, Development of an oligoamide coating as a surface mimetic for aromatic polyamide films used in reverse osmosis membranes, Chem. Commun. 47 (2011) 2384–2386. https://doi.org/10.1039/c0cc04379f.

[30] J.A. Franco, S.E. Kentish, J.M. Perera, G.W. Stevens, Fabrication of a superhydrophobic polypropylene membrane by deposition of a porous crystalline polypropylene coating, J. Memb. Sci. 318 (2008) 107–113. https://doi.org/10.1016/j.memsci.2008.02.032.

[31] H.Z. Shafi, Z. Khan, R. Yang, K.K. Gleason, Surface modification of reverse osmosis membranes with zwitterionic coating for improved resistance to fouling, Desalination. 362 (2015) 93–103. https://doi.org/10.1016/j.desal.2015.02.009.

[32] T. Ishigami, K. Amano, A. Fujii, Y. Ohmukai, E. Kamio, T. Maruyama, H. Matsuyama, Fouling reduction of reverse osmosis membrane by surface modification via layer-by-layer assembly, Sep. Purif. Technol. 99 (2012) 1–7. https://doi.org/10.1016/j.seppur.2012.08.002.

[33] E. De Giglio, N. Ditaranto, L. Sabbatini, 3 Polymer surface chemistry : Characterization by XPS, (n.d.).

[34] H. Karkhanechi, F. Razi, I. Sawada, R. Takagi, Y. Ohmukai, H. Matsuyama, Improvement of antibiofouling performance of a reverse osmosis membrane through biocide release and adhesion resistance, Sep. Purif. Technol. 105 (2013) 106–113. https://doi.org/10.1016/j.seppur.2012.12.016.

[35] H.T.M. Phan, S. Bartelt-Hunt, K.B. Rodenhausen, M. Schubert, J.C. Bartz, Investigation of bovine serum albumin (BSA) attachment onto self-assembled monolayers (SAMs) using combinatorial quartz crystal microbalance with dissipation (QCM-D) and spectroscopic ellipsometry (SE), PLoS One. 10 (2015). https://doi.org/10.1371/journal.pone.0141282.

CHAPTER 4

STUDY OF THE INTERACTIONS BETWEEN COMMON FOULANTS AND MEMBRANE SURFACE USING QCM-D AND MP-SPR

4.1. Introduction

The efficiency of membrane-based filtration processes in water treatment is strongly affected by membrane fouling caused by colloidal deposition, adsorption of organic compounds, formation and growth of bacterial biofilms and/or precipitation of sparingly soluble inorganic compounds [1].

Natural organic matter (NOM) and microbiological substances are commonly present in water resources [2]. These compounds are the principal causes of membrane fouling during a membrane filtration process such as reverse osmosis.

Membrane fouling is such a complex phenomenon depending on a variety of parameters (hydrophobicity or charge of the membrane material, nature of foulant and hydrodynamics of the filtration process) that it results almost impossible

to completely comprehend its development such as to find an optimum strategy to avoid it in a real membrane filtration process [3]. Yet, several studies have performed great work on trying to understand in depth partial aspects of fouling phenomena [4–7].

The results discussed in Chapter 3 have clearly shown that the combination of QCM-D and MP-SPR techniques is a very powerful tool for characterizing molecular interactions at the nanoscale between the surface of different synthetic polyamides films (model membrane system) and a model foulant such as the bovine serum albumin (BSA) protein. The sensitivity of both techniques allowed detecting fouling phenomena at an early-stage and it was shown that the use of both methods could be useful for membrane fouling monitoring during a real filtration process. While this concept was proven in Chapter 3 with a simple case study using a model foulant such as BSA this Chapter 4 is to further investigate the complementarity of QCM-D and MP-SPR for studying the adsorption phenomena underlying membrane fouling. For this purpose, adsorption isotherms were determined on polyamide for BSA, humic acid (HA) and sodium alginate (ALG) with both techniques.

An important aspect to consider when determining adsorption isotherms is that it must be warranted that equilibrium conditions are reached. Mass transfer limitations can affect particularly high-molecular weight solutes such as proteins which have a low

diffusion coefficient according to the Stokes-Einstein relationship [8]. As proteins have high adsorption affinity for most surfaces [9], the kinetic rate of the adsorption can be very fast in comparison with the diffusion of protein molecules into the boundary layer adjacent to the material surface. Thus, reaching the adsorption/desorption equilibrium can be mass-transfer limited. As QCM-D and MP-SPR are real-time monitoring techniques, they bear the advantage that it reaching steady-state can be verified which makes the determination of adsorption isotherms more reliable [8].

4.2. Results and Discussion

The model membrane system used in this Chapter is composed of a commercially available NOMEX-based aromatic polyamide as opposed to Chapter 3 where the polyamide was synthetic (see Chapter 2).

4.2.1. BSA adsorption on an aromatic polyamide as a membrane model

Protein adsorption on a given surface is commonly characterized by measuring adsorption isotherms in order to quantify the amount of protein adsorbed under equilibrium conditions on a specific solid surface. Different experimental methods including optical, spectroscopic, microscopic and thermal analysis tech-

niques are commonly employed to study the adsorption and desorption kinetics of a protein, structural changes and other physical as well as kinetic and thermodynamic parameters related to the adsorption phenomenon [9,10]. The simplest method to study the adsorption of a protein is the Solution Depletion Technique where a concentration change is measured in bulk solution prior and after the adsorption of the protein onto the surface of the employed material [9].

Figures 4.1 A-D depict the adsorption isotherm of the BSA protein measured by QCM-D on both pristine (gold, A) and aromatic polyamide-coated QCM-D sensors (C-D), respectively. The frequency values depicted in all the plots correspond to the steady-state during the desorption step of all the measurements (see Materials and Methods) and therefore represent the irreversible fouling caused by BSA on both gold and aromatic polyamide-coated sensor. Adsorption on a bare gold sensor was measured as a reference because gold is the default sensor surface on top of which the polyamide was deposited.

All adsorption isotherms, including the adsorption of BSA on gold, were Langmuir type. By definition, the latter means that BSA molecules adsorbed on the sensor surface apparently as a monolayer. This observation is in line with what has been reported in previous protein adsorption studies [6].

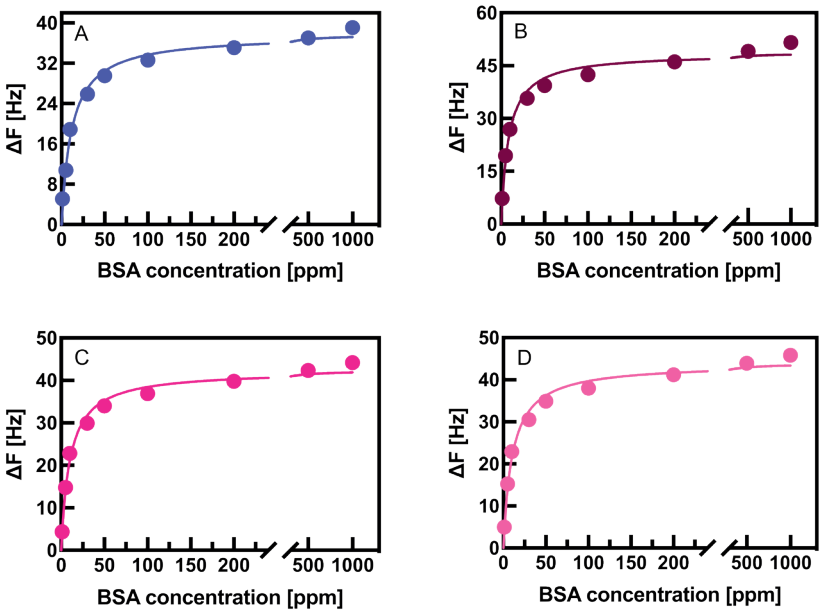

Figure 4.1. Adsorption isotherm of the BSA protein on (A) a bare QCM-D gold sensor and (B-D) QCM-D sensors coated with an aromatic polyamide. B-D were carried out using a different QCM-D sensor for each experiment. The concentration of BSA in the solution ranged from 1 to 1000 ppm. The values were fitted with a Langmuir-type equation considering specific binding, only.

The Langmuir constant and the adsorption maximum values were obtained from the Langmuir-type fit

$$F = \frac{[BSA]_{feed} \cdot Ads_{max}}{[BSA]_{feed} + K_L} \qquad \textbf{Equation 4.1}$$

with: $[BSA]_{feed}$ being the concentration of the BSA protein in the solution; Ads_{max} being the maximum amount adsorbed on

the surface; KL being the Langmuir constant which describes at which concentration of BSA 50% of the saturation is reached.

The respective values are listed in Table 4.1.

Table 4.1. Langmuir constant and maximum adsorption values determined from the fitting of all the adsorption experiments. Test 1 corresponds to the BSA adsorption on gold QCM-D sensor. Test 2, 3 and 4 shows values of the BSA adsorption on PA-coated sensors.

Test ID	K_L [ppm]	Ads_{max} [Hz]
Test 1 (Au-BSA)	11,8	37,7
Test 2 (PA-BSA)	10,0	42,3
Test 3 (PA-BSA)	10,5	43,9
Test 4 (PA-BSA)	10,0	48,5
Average (PA-BSA)	10,2±0,3	44,9±3,2

As can be seen from Table 4.1, the average value of both the Langmuir constant (K_L) and the maximum amount adsorbed (Ads_{max}) of measurements performed with the PA-coated sensors were 10,2±0,3 ppm and 44,9±3,2 Hz, respectively. K_L and Ads_{max} values of BSA on gold are slightly higher and lower, respectively, but of very similar magnitude. This showed the need for guaranteeing that the PA deposition would completely cover the gold electrode in order to avoid experimental artefacts.

On a closer look, Langmuir-fit slightly underestimates the measured frequency value at 1000 ppm (Figure 4.1). A possible explanation could be the contribution of the non-specific interactions between the BSA molecules. At lower concentrations, these interactions also can occur but they will be negligible because the BSA-PA interactions are predominant. As soon as the surface becomes more and more saturated with BSA concentration, the probability of non-specific interactions will increase. In an attempt to corroborate this hypothesis, the following theoretical considerations were made:

A BSA molecule in aqueous solution has been reported to have the approximate dimension of 4 nm x 4 nm x 14 nm [11]. The maximum possible adsorption of BSA would occur with the BSA molecules in an upright position (height 14 nm). The area covered on the sensor surface by a single molecule would then be 16 nm^2. Accounting for the active area of a QCM-D sensor amounting to 1 cm^2 and that the average molecular weight of a BSA molecule is 66,5 kDa, the mass of the adsorbed BSA would be about 690 ng. This mass corresponds to a frequency signal of 39 Hz according to the Sauerbrey equation. Comparing with the data listed in Table 4.1, this value is close to the observed maximum adsorption on gold (37,7 Hz) and below the mean of the Ads_{max} values on PA which is 44,9±3,2 Hz. The very good agreement between theoretically calculated and measured Ads_{max} for gold may be explained by an almost “ideal” adsorption of BSA molecules on a gold surface of minimum surface roughness and lack of surface functional

groups. As opposed to a gold surface, and although polyamide depositions had a low surface roughness in comparison with the molecular dimensions of BSA (see Chapter 3), the presence of surface functional groups may trigger adaptation of the BSA molecules to the polymer surface, which in turn can give rise to additional protein-protein interactions based on van der Waals forces as compared to what occurs on a gold surface [12]. This could explain the higher Ads_{max} values of BSA on PA as compared to gold. The slight underestimation of the adsorbed mass at a liquid BSA concentration of 1000 ppm would then be due to non-specific protein-protein interactions which are independent of the sensor surface.

Similar observations were made with MP-SPR. Figure 4.2 and 4.3 illustrate the change in the resonance angle ($\Delta\theta$) due to the adsorption of the BSA at different concentrations on both an uncoated and PA-coated gold MP-SPR sensors. As before, the data shown in both figures correspond to the desorption step and hence to an irreversible fouling caused by BSA.

As explained in Chapter 2, different wavelengths possess a different sensitivity with sensitivity decreasing with increasing wavelength. As Channels 1 and 3 (670 nm) are the most sensitive ones, they were selected for subsequent calculations when comparing data of MP-SPR and QCM-D. Furthermore, and as mentioned in Chapter 2, the MP-SPR had two parallel “physical” flow channels over the sensor with each

being adapted with two “optical” measurement channels. In the following, “channel” refers to the optical measurement. Hence, the signal of Channels 1 (670 nm) and 2 (785 nm) stem from one flow channel and the signal of Channels 3 (670 nm) and 4 (980 nm) from the other. Duplicating the wavelength of 670 nm in either flow channel added robustness to the measurements.

As can be seen from Figure 4.2 and 4.3, the adsorption isotherm resulted from the irreversible adsorption of the BSA on both gold and PA-coated MP-SPR sensors was a Langmuir type which agreed well with QCM-D data.

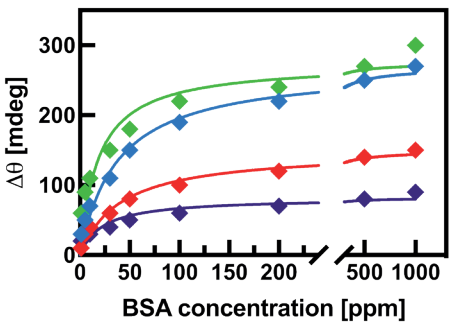

Figure 4.2. Adsorption isotherm of the BSA protein on a bare MP-SPR gold sensor. The concentration of the BSA in the solution ranged from 1 to 1000 ppm. Different colors represent different channels of wavelengths: green curve (channel 1, 670 nm); red curve (channel 2, 785 nm); blue curve (channel 3, 670 nm); purple curve (channel 4, 980 nm).

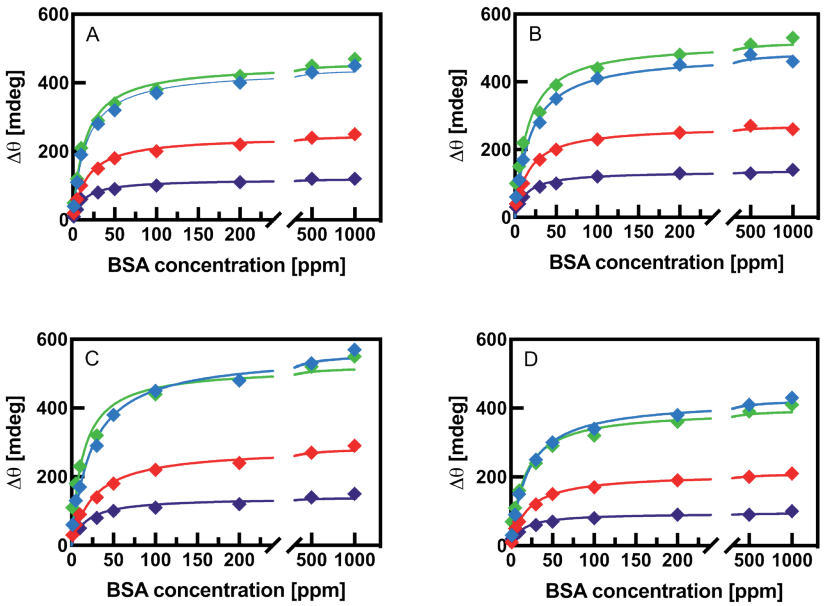

Figure 4.3. Four different adsorption isotherm of the BSA protein on PA-coated MP-SPR sensors. A (Test 2); B (Test 3); C (Test 4); D (Test 5). The concentration of the BSA in the solution ranged from 1 to 1000 ppm. Different colors represent different channels of wavelengths: green curve (channel 1, 670 nm); red curve (channel 2, 785 nm); blue curve (channel 3, 670 nm); purple curve (channel 4, 980 nm).

The resulting Langmuir constant K_L and the maximum of the adsorption Ads_{max} are listed for each independent measurement in Tables 4.2 and 4.3.

Table 4.2. Langmuir constant determined from the curves fitting of the MP-SPR measurements. Test 1 corresponds to the BSA adsorption on a bare gold MP-SPR sensor while Test 2-5 show values of the BSA adsorption on PA-coated MP-SPR sensors.

Test ID	K_L [ppm]			
	Channel 1 (670 nm)	Channel 2 (785 nm)	Channel 3 (670 nm)	Channel 4 (980 nm)
Test 1 (Au-BSA)	37,7	40,5	18,5	22,6
Test 2 (PA-BSA)	15,5	16,8	14,5	13,0
Test 3 (PA-BSA)	18,7	16,1	14,8	12,9
Test 4 (PA-BSA)	23,6	26,4	13,4	16,9
Test 5 (PA-BSA)	20,2	20,2	16,0	13,7
Average (PA-BSA)	19,5±3,4	19,9±4,7	14,7±1,1	14,1±1,9

It is noted that despite the fact that different wavelengths have different sensitivity, this should not affect the Langmuir constant K_L. As can be seen from Table 4.2, the K_L values obtained from Test 1 (Au-BSA) were higher than the K_L values obtained from Tests 2-5 for all the channels. This observation was also made with QCM-D (Table 4.1), however, to a much lesser extent. There is furthermore a significant difference in the K_L values obtained in Channels 1 and 2, on one hand, and Channels 3 and 4, on the other. This seems to correlate with the respective flow channel. For gold, K_L of Channels 1 and 2 double that of Channels 3 and 4; for PA, the K_L as determined by Channels 3 and 4 is about 75%

that of the value obtained from Channels 1 and 2 and it almost doubles that determined by QCM-D (Table 4.1). While for PA all K_L's are similar and of the same order of magnitude (QCM: ~10 ppm; SPR: ~19 ppm and ~14 ppm, respectively), they demonstrate an apparent dependency on the measurement method and/or channel conditions even for equilibrium measurements. Similar observations have been made in an SPR benchmark study on affinity-based biosensors [13]. This corroborates while both QCM-D and MP-SPR yield interactions parameters with a good reproducibility, their absolute values should be used with some caution (as applies to any other measurement method).

In order to simplify following discussions , the mean KL was calculated from Channel 1 and 3 to be 17,1±3,5 ppm.

Table 4.3 presents the adsorption maximum values calculated for all the irreversible adsorption measurements on both uncoated and PA-coated MP-SPR sensors. It was expected that the value of Ads_{max} would diminish according to decreasing sensitivities of the wavelengths (670 nm > 785 nm > 980 nm).

Table 4.3. Maximum adsorption values determined from the curves fitting of the MP-SPR measurements. Test 1 corresponds to the BSA adsorption on bare gold sensor while Test 2-5 shows values of the BSA adsorption on PA-coated sensors.

Test ID	**Ads_{max}** [mdeg]			
	Channel 1 (670 nm)	Channel 2 (785 nm)	Channel 3 (670 nm)	Channel 4 (980 nm)
Test 1 (Au-BSA)	270	150	270	80
Test 2 (PA-BSA)	440	240	460	120
Test 3 (PA-BSA)	480	270	520	140
Test 4 (PA-BSA)	560	280	520	140
Test 5 (PA-BSA)	420	210	400	90
Average (PA-BSA)	480±60	250±30	480±60	120±20

The Ads_{max} values of Channel 1 and 3 were very similar between all tests involving PA coatings and the mean values between Channel 1 and 3 for PA-coated sensors were identical: 480±60 mdeg. Assuming that 1 mdeg corresponds to 0,8333 ng/cm² of protein for a wavelength of 670 nm (see Chapter 2), the maximum adsorbed mass per area as determined by MP-SPR would be Ads_{max}(PA-BSA, SPR) = 400,0 ± 50 ng·cm^{-2}. In comparison, according to Table 4.1 and applying the Sauerbrey equation, the adsorbed surface density as determined by QCM-D would be Ads_{max}(PA-BSA, QCM-D) = 44,9 ± 3,2 Hz Δ 794,7 ± 56,6 ng·cm^{-2}, which is practically twice as much as determined by MP-SPR.

Interestingly, as for gold, the same calculation would yield, Ads-max(Au-BSA, QCM-D) = 37,7 Hz = 667,3 ng·cm^{-2} for QCM-D, and Ads_{max} (Au-BSA, SPR) = 270 mdeg = 225,0 ng·cm^{-2} for MP-SPR. Hence, QCM-D determines the maximum amount of BSA adsorbed on polyamide to be twice as high as MP-SPR does, for gold it is even three times as high.

The reason for this difference is the fact that QCM-D detects both the BSA mass and its associated water while MP-SPR only detects the adsorption of the protein ("dry mass", Figure 3.1). This complementarity of both methods is useful as associated water molecules can lead to a different structural changes that can affect protein stability and assembly [6,14]. In this context, the interaction of BSA with either gold or polyamide and the hydration of each of the two surfaces will also be different. As for the polymer deposition, the sensors were coated using a commercially available aromatic NOMEX-based polyamide (see Chapter 2). In order to properly solubilize this polyamide, lithium chloride salt (LiCl) was added to the solution. Lithium cations interact with the amide groups of the polyamide thus diminishing the strength of the hydrogen bonds generated inside the polymeric chains and promoting a better solubilization into the solvent [15]. As a consequence, LiCl molecules are located between the polymeric chains of the polyamide and can be expected to significantly contribute to the surface charge and hydration. This, in turn, may affect how BSA adsorbs on the surface.

In Chapter 3 a LiCl-free polyamide was used for deposition and for an equilibrium liquid concentration of BSA of 100 ppm and the surface density of BSA adsorbed was determined to be 522±37 ng/cm² and 211±38 ng/cm² for QCM-D and MP-SPR, respectively (Figure 3.12.). In this case QCM-D overestimated the mass adsorbed by a factor of 2.5 which is slightly higher than for NOMEX.

The ratio of “dry” mass (MP-SPR) to “wet” mass (QCM-D) was found to be concentration-dependent. Figure 4.4 depicts the calculated MP-SPR/QCM-D mass ratios from the experimental data as a function of the BSA equilibrium concentration in solution.

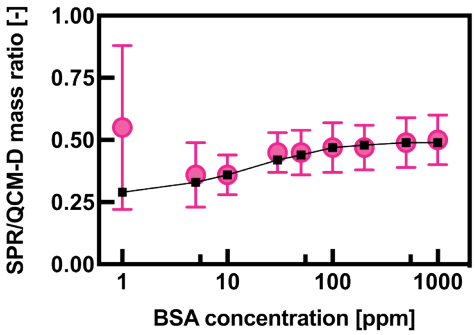

Figure 4.4. SPR/QCM-D adsorbed mass ratios for each BSA concentration in the solution. The experimental values are represented by circles. Error bars correspond to the standard deviation of the mean. Black squares represent theoretical values calculated using equation 4.1. (Langmuir fit).

As can be seen, in general the MP-SPR/QCM-D mass ratios increase with rising BSA concentration. This means that at low surface densities BSA is apparently more hydrated than at surface densities near saturation (above a liquid concentration of 100 ppm). The only exception is the experimental data point at 1 ppm which differs significantly from theoretical mass ratio values (black squares) and suggests a significantly less hydrated BSA. It is emphasized that the reproducibility of the results from QCM-D measurements at liquid BSA concentration of 1 ppm was very low as can be observed from the error bar. Yet, as outlined in Chapter 3, QCM-D reveals information on the viscoelasticity of adsorbed layers through its dissipation measurement. In the case of a relatively less hydrated adsorption layer in the latter case, one would assume that this will be reflected in a lower dissipation or dissipation/mass ratio as long as the Sauerbrey equation holds.

Figure 4.5 (left) shows the change in the measured dissipation as a function of the frequency for the adsorption of the BSA onto the PA-coated QCM-D sensors for one experiment. While there is an overall linear relationship between the dissipation and the frequency implying that apparently BSA adsorbs in the same way irrespective of the surface density, a minor “bump” toward a slightly higher dissipation can be observed at 1 ppm (grey). This could indicate a slightly higher degree of hydration rather than lower.

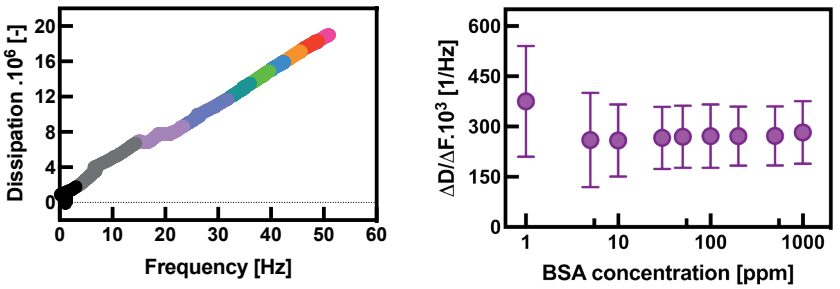

Figure 4.5. Left: Measured dissipation as a function of the frequency for one experiment. Each color represents a different BSA concentration in the solution: baseline obtained with PBS buffer (black); 1 ppm (grey); 5 ppm (mauve); 10 ppm (lavender); 30 ppm (cyan); 50 ppm (green); 100 ppm (blue); 200 ppm (orange); 500 ppm (red);1000 ppm (pink). **Right:** ΔD/ΔF ratio as a function of the BSA concentration in the solution for the BSA adsorption on PA-coated sensors measured by QCM-D. The error bars correspond to the standard deviation of the mean.

This finding is corroborated by plotting the ΔD/ΔF ratio for each concentration of the BSA in the solution (Figure 4.5., right). The ΔD/ΔF ratio represents how much energy is dissipated per unit of adsorbed mass. The higher ΔD/ΔF value the softer will be the adsorbed BSA layer, which would significate a greater amount of associated water or a larger water cloud attached to the adsorbed layer.

As can be observed, for BSA concentrations ranging from 5 to 1000 ppm, the ΔD/ΔF ratios remained almost constant except for a higher ΔD/ΔF ratio at 1 ppm. This is in line with Figure 4.5, left, and the tendency of the fitted data in Figure 4.4 (black squares). It can therefore be concluded that the respective experimental

value in Figure 4.4. is an artefact stemming from high noise. For the rest of BSA concentrations the dissipation did not reveal any additional insights.

Steady-state conditions were observed within less than 20 minutes when determining BSA isotherms. In a real membrane filtration process, the membrane may be exposed to varying concentrations of foulants which might imply that steady-state is actually not reached. Nevertheless, in the subsequent measurements performed with other foulants an experimental time interval of 20 minutes was also chosen for the adsorption step for comparison reasons, irrespective of whether equilibrium conditions were reached.

4.2.2. ALG adsorption on an aromatic polyamide as a membrane model

The presence of natural organic matter (NOM) in natural water resources is very typical and the compounds that are classified as NOM are considered the most problematic foulants for membrane-based processes [16]. NOM is usually divided into hydrophilic and hydrophobic fractions. Regarding the hydrophilic fraction, polysaccharides are the main constituents of NOM in seawater [1]. Therefore, sodium alginate (ALG) was chosen as a representative organic model foulant. ALG is an acidic polysaccharide which is mainly produced by microalgae, macroalgae and bacteria [2]. The aim of the following section was to study the capability of QCM-D and MP-SPR for detecting the ALG de-

position on the polyamide-coated sensors and therefore, predict what would be the effect of the presence of this compound on a real membrane-based filtration process.

A first principal difference observed in comparison to BSA adsorption on polyamide was that alginate (ALG) had not reached an equilibrium adsorption even after 17 hours (Figure 4.6.).

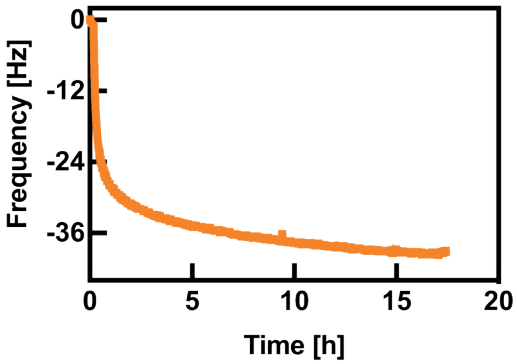

Figure 4.6. Adsorption of sodium alginate on an QCM-D sensor coated with an aromatic polyamide. Only after 17 hours of experimentation the adsorption equilibrium was reached.

This observation was the opposite of what has been previously observed in another study where authors reported measurements of ALG adsorption by QCM-D. In that work the author claimed that ALG reached the adsorption equilibrium in less than 2 hours with an average time of 1 hour in most cases [17]. In the cited work, the QCM-D sensors had been modified with self-assembled monolayers (SAMs) of different functionalities representative for the functional groups of an aromatic polyamide membrane. The difference observed might therefore stem from

the fact that in this Chapter the sensors had been modified with the polyamide membrane polymer rather than only SAMs in order simulate the membrane surface in a more realistic manner.

For reasons outlined in the previous section, adsorption studies were limited to 20 minutes for comparison reasons although in view of Figure 4.6. it becomes evident that under these conditions adsorption of ALG on PA was far from steady-state. Figure 4.7 depicts the change in the frequency corresponding to the adsorption of ALG as a function of its concentration in solution on both pristine (Test 1) and aromatic polyamide-coated QCM-D sensors respectively (Tests 2-4). The represented values where those corresponding to the desorption step of the measurements in order to simulate irreversible fouling caused by ALG.

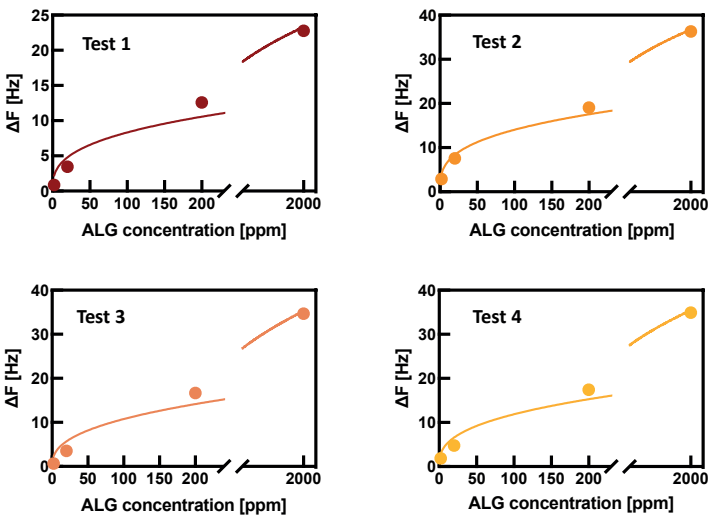

Figure 4.7. Adsorption of ALG on a bare QCM-D gold sensor (Test 1) and on polyamide (Tests 2-4). The concentration of the ALG in the solution ranged from 2 to 2000 ppm. The values were fitted to a Freundlich-type curve.

In order to study the reproducibility of all these measurements, a Freundlich least squares fit was applied according to the following equation:

$$\Delta F = K_F \cdot [C]_{feed}^{1/n} \qquad \textbf{Equation 4.2}$$

where ΔF is the frequency change corresponding to the amount of ALG adsorbed on the QCM-D sensor; K_F: Freundlich constant; C_{feed}: concentration of ALG in the solution; n: empirical Freundlich exponent.

As can be observed from Figure 4.7, all the experiments fitted quite well to a Freundlich-type isotherm although strictly seen the equilibrium conditions as required for isotherms had not been reached. This type of isotherm is typical for a multi-layer adsorption system. It would indicate that apparently ALG molecules interacted first with the functional groups of the polyamide covering the sensor surface. Once no more alginate-polyamide interactions could be established, alginate-alginate interactions began to occur. This aspect is crucial for a real membrane filtration process because being able to detect the presence of this compound from the beginning is imperative as it can generate considerable fouling.

Table 4.4. lists the Freundlich constant and exponent, K_F and n, respectively, for the adsorption of ALG on both gold and polyamide.

Table 4.4. Freundlich constants K_F and exponents n as determined from the fitting of all the adsorption experiments. Test 1 corresponds to the ALG adsorption on gold QCM-D sensor. Values from Test 2, 3 and 4 correspond to the ALG adsorption on PA-coated sensors.

Test ID	K_F [Hz·ppm$^{-1/n}$]	n [-]
Test 1 (Au-ALG)	1,71	2,91
Test 2 (PA-ALG)	3,21	3,12
Test 3 (PA-ALG)	1,73	2,52
Test 4 (PA-ALG)	2,21	2,74
Average (PA-ALG)	2,38±0,76	2,79±0,30

The average value of both the Freundlich constant (K_F) and exponent (n) for the PA-coated sensors were 2,38±0,76 Hz·ppm$^{-1/n}$ and 2,79±0,30, respectively. The exponent (n) of gold and PA-coated sensors agreed quite well. One concern was whether these data are meaningful even though they were obtained far from adsorption equilibrium. In order to clarify this aspect, the adsorption isotherm of BSA was taken as an example. Even considering frequency values for each concentration when the adsorption kinetics was still at only about 50% of equilibrium value (toward the end of the linear transient), a Langmuir type adsorption was obtained (Figure 4.8.). K_L and Ads_{max} amounted to 11,9 ppm and 31,6 Hz, respectively. Compared to values listed in Table 4.1, Ads_{max} is naturally lower but the more relevant K_L is similar. The adsorption "isotherm", hence, maintained its characteristics despite of using non-equilibrium data.

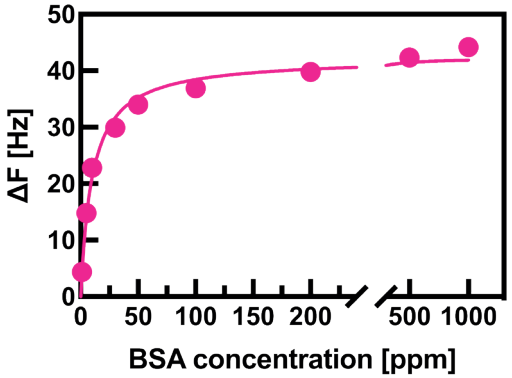

Figure 4.8. Adsorption isotherm of the BSA protein on QCM-D sensor coated with an aromatic polyamide. The values represented correspond to frequency values obtained without letting the experiment reach the steady state. The concentration of the BSA in the solution ranged from 1 to 1000 ppm. The values were fitted to a Langmuir-type curve in the same way of data that correspond to an equilibrium (Figure 4.1).

Figure 4.9 and 4.10 illustrate the change in the resonance angle (Δθ) due to the adsorption of the ALG at different concentrations on both an uncoated and PA-coated gold MP-SPR sensors. The data shown in both figures correspond to the desorption step and hence to an irreversible fouling caused by ALG. Each curve represents a different wavelength of varied sensitivity. Data were fitted according to the aforementioned Freundlich equation. As can be seen in Figures 4.9 and 4.10, data related to the adsorption of ALG on both gold and polyamide surfaces fitted well to Freundlich isotherm and in good agreement with QCM-D (Figure 4.7).

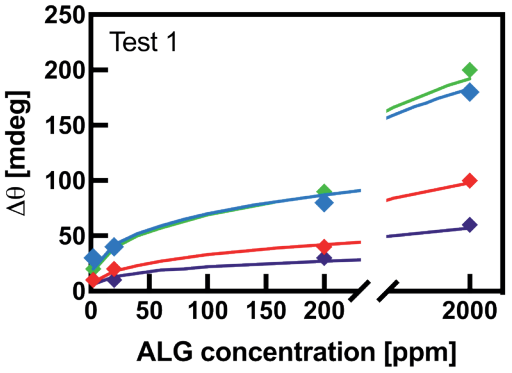

Figure 4.9. Adsorption isotherm of the ALG foulant on a bare MP-SPR gold sensor. The concentration of the ALG in the solution ranged from 2 to 2000 ppm. Different colors represent different channels of wavelengths: green curve (channel 1, 670 nm); red curve (channel 2, 785 nm); blue curve (channel 3, 670 nm); purple curve (channel 4, 980 nm).

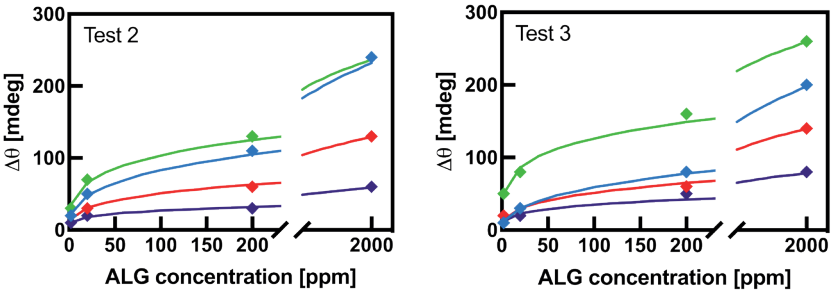

Figure 4.10. Adsorption isotherm of the ALG foulant on PA-coated MP-SPR gold sensors. The concentration of the ALG in the solution ranged from 2 to 2000 ppm. Different colors represent different channels of wavelengths: green curve (channel 1, 670 nm); red curve (channel 2, 785 nm); blue curve (channel 3, 670 nm); purple curve (channel 4, 980 nm). Two independent measurements were carried out using two different MP-SPR sensors.

Table 4.5 and Table 4.6 list the fitted Freundlich parameters K_F and n for all wavelengths.

Table 4.5. Freundlich constant determined from the fitting of all the adsorption experiments. Test 1 corresponds to the ALG adsorption on gold MP-SPR sensor. Test 2 and 3 correspond to the ALG adsorption on PA-coated MP-SPR sensors.

Test ID	**K_F** [mdeg·ppm$^{-1/n}$]			
	Channel 1 (670 nm)	Channel 2 (785 nm)	Channel 3 (670 nm)	Channel 4 (980 nm)
Test 1 (Au-ALG)	20	10	10	10
Test 2 (PA-ALG)	20	10	30	10
Test 3 (PA-ALG)	10	10	40	10
Average (PA-ALG)	15±7	10±0	35±7	10±0

As can be seen, all the K_F values were similar between all the measurements which implies that they were reproducible. However, Channel 1 and 3 (both having a wavelength of 670 nm) gave different values. The same behavior was observed for the BSA adsorption isotherms using the MP-SPR. Regarding the ALG adsorption experiments, in both Test 2 and 3 the K_F value determined using the Channel 3 is slightly higher than that of Channel 1. More importantly, the Freundlich exponent “n” as determined in Channel 1 (2,69±0,32) was in very good agreement with the one obtained by QCM-D (2,79±0,30) while all other channels yielded higher, although similar values.

Table 4.6. Freundlich exponent "n" determined from the fitting of all the adsorption experiments. Test 1 corresponds to the ALG adsorption on gold MP-SPR sensor. Tests 2 and 3 correspond to the ALG adsorption on PA-coated MP-SPR sensors.

Test ID	**n** [-]			
	Channel 1 (670 nm)	Channel 2 (785 nm)	Channel 3 (670 nm)	Channel 4 (980 nm)
Test 1 (Au-ALG)	3,15	2,72	2,90	3,12
Test 2 (PA-ALG)	2,91	3,21	3,62	3,84
Test 3 (PA-ALG)	2,46	2,99	4,18	3,70
Average (PA-ALG)	2,69±0,32	3,10±0,16	3,90±0,40	3,77±0,10

Again, based on Table 4.6. it can be concluded that ALG adsorbs in a very similar manner on the gold reference as on polyamide. This also is in agreement with data from QCM-D (Table 4.4).

As opposed to BSA (Figure 4.4), the alginate adsorbed on polyamide seems to form more and more hydrated fouling layers with increasing concentrations, as indicated by a decreasing MP-SPR/QCM-D ("dry"/"wet") mass ratio (Figure 4.11, left). ALG molecules are known to interact creating a net-like structure in which water molecules can be trapped. The experimental datapoint for the lowest concentration of 2ppm bears a large error but the theoretical MP-SPR/QCM-D mass ratios calculated on the basis of the Freundlich equation (black squares) confirm this trend. The MP-SPR/QCM-D mass ratio of the ALG layers adsorbed was in a

similar range as those determined with BSA. Yet it can intuitively be recognized that Freundlich-type fouling by ALG may be more severe in membrane applications than Langmuir-type fouling of BSA which does not go beyond the formation of a mono-layer.

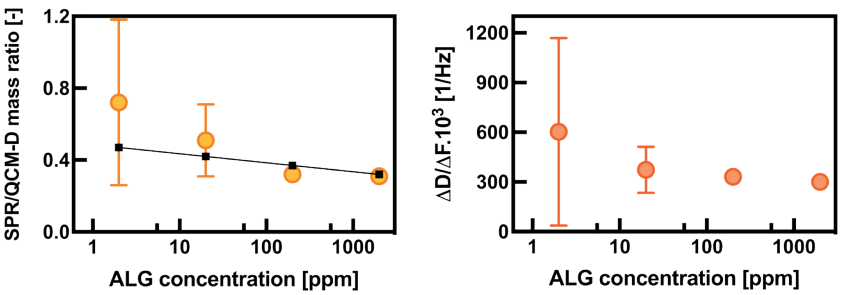

Figure 4.11. Left: SPR/QCM-D adsorbed mass ratios for each ALG concentration in the solution. The experimental values are represented by orange circles. Error bars correspond to the standard deviation of the mean. Black squares represent the theoretical values calculated using Equation 4.2. of the curve fitting. Right: ΔD/ΔF ratio as a function of the ALG concentration in the solution for the ALG adsorption on PA-coated sensors measured by QCM-D. The error bars correspond to the standard deviation of the mean.

One would expect that an increasing degree of hydration with rising ALG concentration in the liquid would be reflected in the viscoelasticity, i.e. an increase in the ΔD/ΔF ratio. Figure 4.11, right, illustrates that this was not the case. ΔD/ΔF ratios remained almost constant independently of the ALG concentration between 20 to 2000 ppm of ALG, with an average ΔD/ΔF of $334{,}9.10^{-3} \pm 36{,}6.10^{-3}$ Hz^{-1}. The large error of the datapoint at 2 ppm prohibits making interpretations. Similarly to observations made with QCM-D, while ΔD/ΔF values

did not reveal significant insights, the MP-SPR/QCM-D mass ratios did. This advocates once more for a combination of both techniques.

4.2.3. HA adsorption on an aromatic polyamide as a membrane model

The hydrophobic fraction of NOM is mainly composed of humic substances being the most common foulant the Humic Acid (HA) [16]. HA is naturally present in water resources but it can be also found in raw wastewater and in primary, secondary and tertiary effluents from municipal wastewater treatments facilities [18]. In this section HA was used as a representative model foulant of hydrophobic fraction of NOM. Its adsorption on PA-coated QCM-D and MP-SPR sensors was studied in order to further study the complementarity of both methods.

While ALG required already a relatively long time to reach a steady-state adsorption (about 17 h), HA exceeded this time by far. After almost one week (150 hours) of experimentation, the steady state was not completely reached, yet (Figure 4.12). For this reason, the same experimental time interval of 20 minutes was fixed for subsequent experiments as had been done before in the adsorption measurements of BSA and ALG.

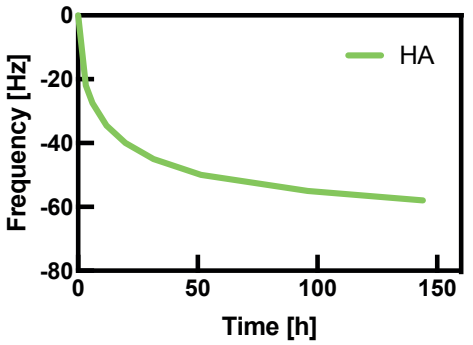

Figure 4.12. Adsorption of humic acid on an QCM-D sensor coated with an aromatic polyamide. After almost 150 hours of experimentation the adsorption equilibrium was not completely reached.

Figure 4.13 illustrates the change in the frequency measured by QCM-D (left) and the change in the resonance angle (Δθ) measured by MP-SPR (right) due to the adsorption of the HA at different concentrations on bare QCM-D and MP-SPR sensor.

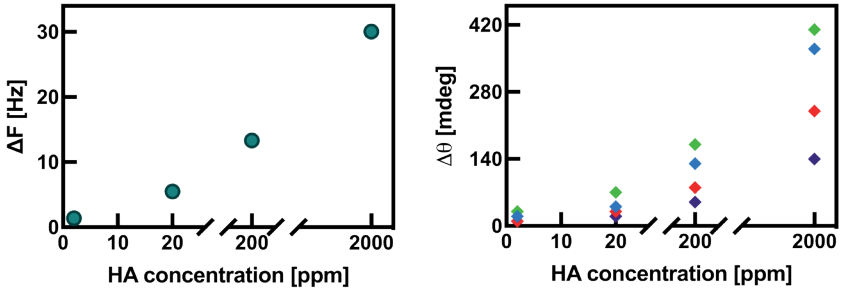

Figure 4.13. Measured change in the frequency (left) and resonance angle (right) due to the adsorption of HA on a bare QCM-D and MP-SPR sensor. The concentration of the HA in the solution ranged from 2 to 2000 ppm.

Figure 4.14 shows the change in the frequency and resonance angle measured by QCM-D and MP-SPR, respectively, due to the adsorption of HA on PA-coated sensors. These frequency values correspond to the desorption step of all the measurements thus representing the irreversible adsorption of HA. An increasing amount of HA was deposited on both gold and PA when exposing the sensors to an increasing concentration of HA in the solution.

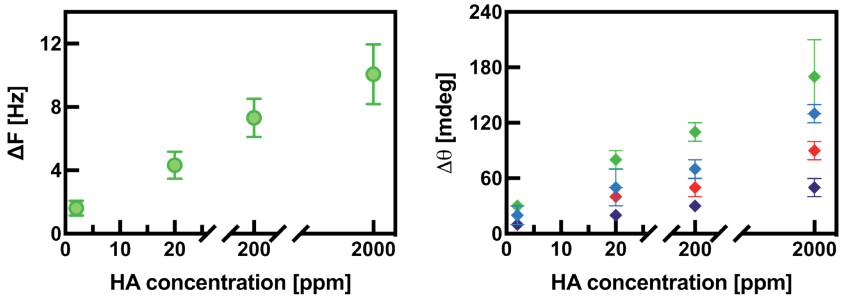

Figure 4.14. Measured change in the frequency (left) and resonance angle (right) due to the adsorption of HA on PA-coated QCM-D and MP-SPR sensors. Four independent QCM-D and two independent MP-SPR measurements were carried out using a different sensor for each experiment. The concentration of the ALG in the solution ranged from 2 to 2000 ppm. The error bars represent the standard deviation of the mean.

However, on PA measurements, the average maximum change in the measured frequency was 10,06±1,89 Hz, which was lower of what has been observed with measurements using BSA and ALG. From MP-SPR measurements, a maximum change in the resonance angle (Δθ) of 130±10 and 170±40 mdeg were obtained for Channels 1 and 3, respectively. These values were also lower of what was measured for BSA and ALG.

HA is a highly negatively charged molecule and as PA is also negatively charged, electrostatic repulsion can occur explaining the lower amount of adsorption. Similar observations were found in other works where adsorption of HA was studied using the QCM-D on negatively charged surfaces such as cellulose acetate butyrate (CAB) and Silica (SiO_2) [16,19].

In this case, it was not possible to fit these data to any adsorption model. Empirically seen, there appeared to exist a logarithmic correlation between sensor signals and solute concentration in the liquid.

In the case of HA, neither the MP-SPR/QCM-D nor the ΔD/ΔF ratios revealed any significant insights (Figure 4.15). The MP-SPR/QCM-D mass ratio varied around an average value of about 0,68 which hints at a less hydrated adsorption layer in comparison to BSA and ALG.

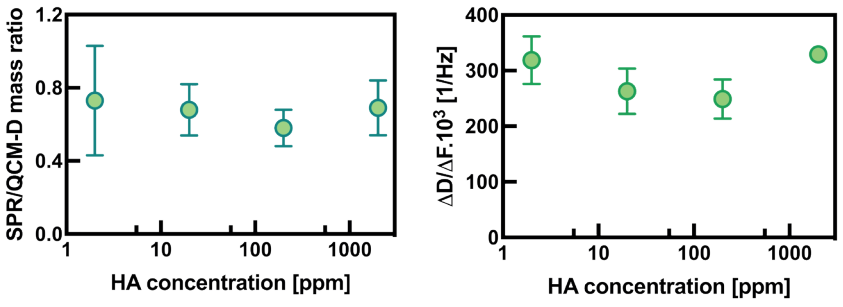

Figure 4.15. MP-SPR/QCM-D mass ratio (left) and ΔD/ΔF ratio from QCM-D (right) for each HA concentration in the solution. Error bars correspond to the standard deviation of the mean. Logarithmic scale is applied to the "x" axis in order to visualize data with a more homogeneous distribution.

On the other hand, from ΔD/ΔF ratios (Figure 4.14, right) seem to reveal up to 200 ppm of HA in solution that the HA layer adsorbed on PA becomes less dissipative and, hence, more rigid, i.e. the opposite of what would be concluded from mass ratios. However, the data point of 2000 ppm deviated from this apparent trend supposedly indicating a more dissipative adsorbed HA layer, the reason for which remains unclear. Conducting these measurements closer to a steady-state condition could possibly yield more robust insights with respect to the hydration and dissipation of the HA layer.

4.2.4. Determining the real fouling degree of an aromatic polyamide

Intensive work has been performed in order to elucidate fouling mechanisms in pressure-driven membrane processes such as RO. However, as will be shown in this section of Chapter 4, the conclusions can be very different depending on the experimental conditions.

Figure 4.16 compares the time needed for each foulant to reach steady-state adsorption on an aromatic polyamide, represented by the change in the frequency measured by QCM-D.

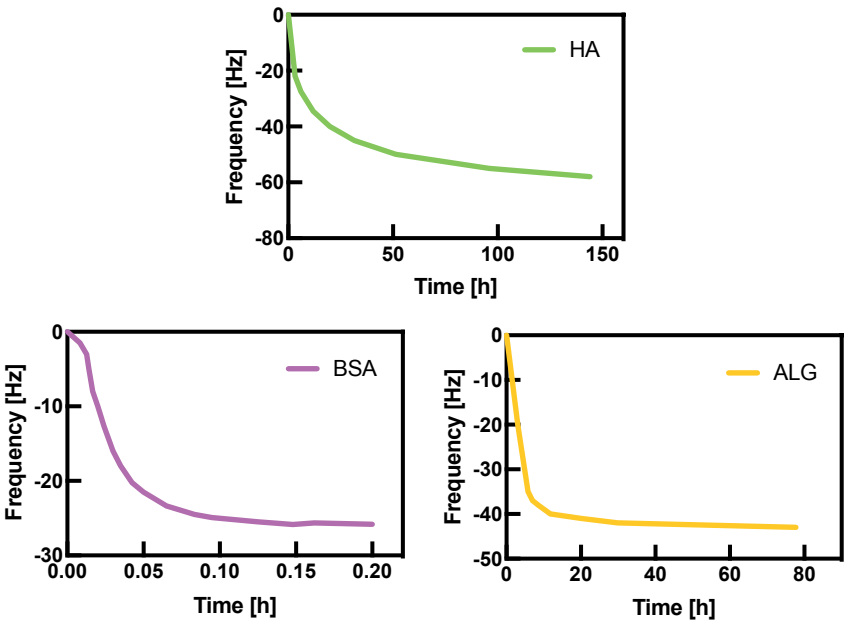

Figure 4.16. Adsorption of BSA, ALG and HA on a PA-coated QCM-D sensor. The change in the frequency is represented as a function of time in order to compare the adsorption profile of the three representative foulants. The concentration used in the measurements was 2000 ppm for all the foulants.

The time required to reach the steady-state was considerably different between the three foulants. While in the case of BSA and adsorption equilibrium was reached in about 15 minutes along with the generation of a monolayer (see section 4.2.1), it took ALG about 80 hours, more than three days. For HA almost one week (150 hours) was not enough for reaching the adsorption equilibrium.

The tremendous difference in the time which these three foulants require in order to reach and adsorption equilibrium (in the case of HA it would take even longer) have a very important consequence on characterizing the severity of fouling by different foulants:

When measuring the adsorption of these three foulants during 15 minutes – an apparently reasonable experimental duration given that BSA reaches the adsorption equilibrium – one would observe and conclude that BSA fouls polyamide far more than the ALG and particularly HA which until then hardly adsorbed on the polyamide surface (Figure 4.17, A).

If, however, studying the adsorption for 4 hours, one would find that all three compounds foul the membrane to the same extent (Figure 4.17, B).

Finally, letting the experiment run for one week, one would observe that in this case, the most problematic foulant apparently was HA as it adsorbed the most, followed by ALG. BSA, on the other hand, would be considered to be the foulant that adsorbed least (Figure 4.17, C) – all in all, precisely the opposite to the outcome of the first experiment (Figure 4.17, A).

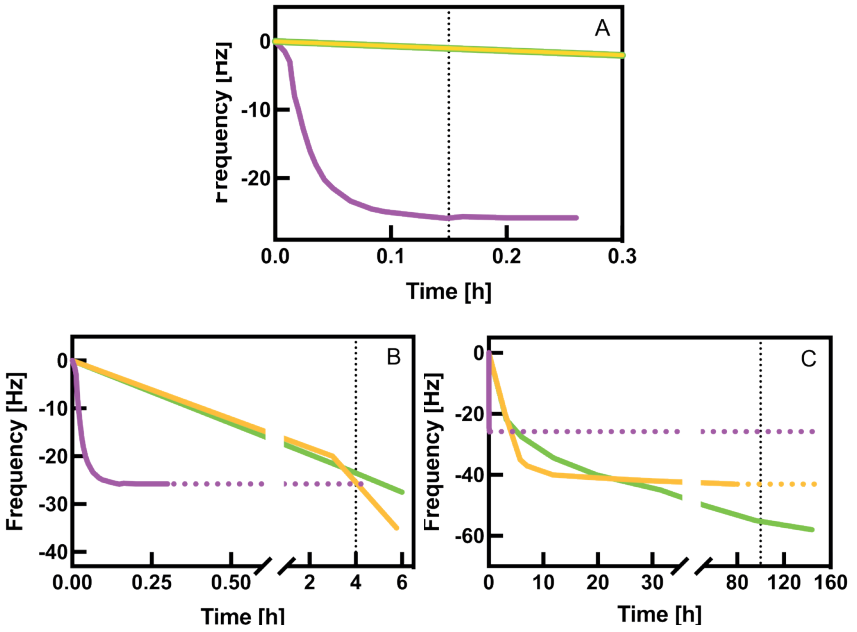

Figure 4.17. Adsorption of BSA (pink), ALG (orange) and HA (green) on a PA-coated QCM-D sensor with the vertical dotted line indicating 15 minutes (A); 4 hours (B); and almost one week (C, 150 hours) of experimentation.

This means that if the experimental methodology does not permit verifying in real-time that that steady-state conditions have actually been reached, then results on the fouling tendency may not at all be reliable. While this seems to be obvious, this aspect has been discussed little in literature, which might be one of the reasons for the occasionally contradictory findings reported.

Based on the results depicted in Figure 4.16, from a process point of view the most problematic foulants would be ALG and particularly HA, as they slowly form multi-layers rather than reaching quickly a steady-state as does BSA. In fact, it has been reported in literature that fouling by ALG is more severe in the long run than that of BSA [4]. The fouling generated by ALG is furthermore aggravated in the presence of divalent cations such as Ca^{2+} and Mg^{2+} [20]. These divalent cations complex with carboxylate groups of ALG molecules creating a gel layer [21]. It has also been reported that the presence of hydraulic pressure make these ALG gel layer more compact being more difficult to recover the membrane surface after the cleaning step [5].

Yet, Qilin Li et al. [4] observed when exposed to BSA, the flux of an RO membrane was relatively stable for the first 8 hours of experimentation but thereafter the flux decreased continuously during 4 days without reaching a steady state flux. The authors explained this trend by assuming a two-stage BSA fouling. First, BSA molecules adsorbed on the membrane surface due to hydrophobic interactions until a monolayer is created. The adsorption occurs slowly as both the BSA and the RO membrane are negatively charged and thus, the initial flux decline is not significant. Afterwards more BSA molecules deposit onto the adsorbed BSA monolayer creating a multilayer. The authors claimed that apparently BSA-BSA interactions are stronger than BSA-membrane interactions thus leading to a greater flux decline than what was

observed in the first hours of the filtration. This observation is opposite to what has been found in this Chapter, where it was demonstrated that the BSA formed a monolayer on the PA-coated sensor and no more adsorption is detected when increasing its concentration in the solution. The authors refer to previous studies where BSA fouling was studied for microfiltration (MF) and ultrafiltration (UF) membranes [22,23]. However, these types of membranes have pores and therefore pore-clogging could occur due to the hydraulic pressure. This would explain the greater flux decline in comparison with RO membranes. Thus, the flux decrease observed in the cited work may not be related to a multi-layered BSA fouling based on strong BSA-BSA interactions but a possible explanation could rather be that physical aspects such as concentration polarization in the hydrodynamic membrane boundary layer could contribute to a flux decline [18].

From a process point of view, studying fouling interactions may be of limited value. There are several studies focusing on mixtures of foulants in order to understand which would be the potential of the combined compounds to foul the RO membrane. A synergistic effect was observed when mixing different foulants such as BSA, ALG and HA creating a higher flux decline than that caused by individual foulants [1,25,26]. This demonstrates that in the common case that the feedwater contains many different compounds, predicting the fouling propensity if virtually impossible.

4.3. Conclusions

QCM-D and MP-SPR are complementary and highly useful methods for monitoring and predicting membrane fouling based on chemical interactions. Both techniques measure on real-time the chemical interactions between the functional groups of the aromatic polyamide and those of model foulants. Therefore, this analytical combination is very powerful to elucidate membrane fouling phenomenon. However, QCM-D has a limitation: together with the adsorbed mass per area it also measures intrinsically the associated water molecules that contribute to an additional mass thus leading to an overestimation of the mass adsorbed per area. In this sense, the MP-SPR seems to allow a more robust characterization of fouling layers if it is the "dry" mass per area that is of interest. For porous membranes, however, it might be very useful to measure the hydrated mass as it would possibly describe pore clogging more accurately.

While QCM-D could potentially provide useful information on the viscoelasticity of the adsorbed fouling layers thanks to the dissipation parameter, experimental data of dissipation for the adsorption of BSA, ALG and HA on the aromatic polyamide-coated sensors did not reveal any significant information. MP-SPR/QCM-D mass ratios were more illustrative in this sense.

Finally, the combination of QCM-D and MP-SPR is a useful way for measuring the real adsorption equilibrium of com-

mon foulants on an aromatic polyamide as both methods measured on real time. However, although having a thermodynamic understanding of the adsorption process is important, from a process point of view this may not be very relevant. What is really important is to rapidly detect critical limits of fouling such as to take timely action based on this information.

4.4. References

[1] M.M. Motsa, B.B. Mamba, A.R.D. Verliefde, Combined colloidal and organic fouling of FO membranes: The influence of foulant-foulant interactions and ionic strength, J. Memb. Sci. 493 (2015) 539–548. https://doi.org/10.1016/j.memsci.2015.06.035.

[2] G. Amy, Fundamental understanding of organic matter fouling of membranes, Desalination. 231 (2008) 44–51. https://doi.org/10.1016/j.desal.2007.11.037.

[3] S. Jiang, Y. Li, B.P. Ladewig, A review of reverse osmosis membrane fouling and control strategies, Sci. Total Environ. 595 (2017) 567–583. https://doi.org/10.1016/j.scitotenv.2017.03.235.

[4] Q. Li, Z. Xu, I. Pinnau, Fouling of reverse osmosis membranes by biopolymers in wastewater secondary effluent : Role of membrane surface properties and initial permeate flux, 290 (2007) 173–181. https://doi.org/10.1016/j.memsci.2006.12.027.

[5] B. Mi, M. Elimelech, Organic fouling of forward osmosis membranes : Fouling reversibility and cleaning without chemical reagents Organic fouling of forward osmosis membranes : Fouling reversibility and cleaning without chemical reagents, (2017). https://doi.org/10.1016/j.memsci.2009.11.021.

[6] A.E. Contreras, A. Kim, Q. Li, Combined fouling of nanofiltration membranes : Mechanisms and effect of organic matter, 327 (2009) 87–95. https://doi.org/10.1016/j.memsci.2008.11.030.

[7] A. Sweity, Y. Oren, Z. Ronen, M. Herzberg, The influence of antiscalants on biofouling of RO membranes in seawater desalination, Water Res. 47 (2013) 3389–3398. https://doi.org/10.1016/j.watres.2013.03.042.

[8] R.A. Latour, The Langmuir isotherm: A commonly applied but misleading approach for the analysis of protein adsorption behavior, J. Biomed. Mater. Res. - Part A. 103 (2015) 949–958. https://doi.org/10.1002/jbm.a.35235.

[9] V. Hlady, J. Buijs, H.P. Jennissen, Methods for studying protein adsorption, Methods Enzymol. 309 (1999) 402–429. https://doi.org/10.1016/S0076-6879(99)09028-X.

[10] M. Wiśniewska, D. Sternik, P. Nowicki, S. Chibowski, M. Medykowska, M. Gęca, K. Szewczuk-Karpisz, Adsorption, viscosity and thermal behaviour of nanosized proteins with different internal stability immobilised on the surface of mesoporous activated biocarbon obtained from the horsetail herb precursor, Appl. Nanosci. (2021). https://doi.org/10.1007/s13204-021-01759-x.

[11] H.T.M. Phan, S. Bartelt-Hunt, K.B. Rodenhausen, M. Schubert, J.C. Bartz, Investigation of bovine serum albumin (BSA) attachment onto self-assembled

monolayers (SAMs) using combinatorial quartz crystal microbalance with dissipation (QCM-D) and spectroscopic ellipsometry (SE), PLoS One. 10 (2015). https://doi.org/10.1371/journal.pone.0141282.

[12] C.M. Roth, B.L. Neal, A.M. Lenhoff, Van der Waals interactions involving proteins, Biophys. J. 70 (1996) 977–987. https://doi.org/10.1016/S0006-3495(96)79641-8.

[13] R.L. Rich, G.A. Papalia, P.J. Flynn, J. Furneisen, J. Quinn, J.S. Klein, P.S. Katsamba, M.B. Waddell, M. Scott, J. Thompson, J. Berlier, S. Corry, M. Baltzinger, G. Zeder-Lutz, A. Schoenemann, A. Clabbers, S. Wieckowski, M.M. Murphy, P. Page, T.E. Ryan, J. Duffner, T. Ganguly, J. Corbin, S. Gautam, G. Anderluh, A. Bavdek, D. Reichmann, S.P. Yadav, E. Hommema, E. Pol, A. Drake, S. Klakamp, T. Chapman, D. Kernaghan, K. Miller, J. Schuman, K. Lindquist, K. Herlihy, M.B. Murphy, R. Bohnsack, B. Andrien, P. Brandani, D. Terwey, R. Millican, R.J. Darling, L. Wang, Q. Carter, J. Dotzlaf, J. Lopez-Sagaseta, I. Campbell, P. Torreri, S. Hoos, P. England, Y. Liu, Y. Abdiche, D. Malashock, A. Pinkerton, M. Wong, E. Lafer, C. Hinck, K. Thompson, C. Di Primo, A. Joyce, J. Brooks, F. Torta, A.B. Bagge Hagel, J. Krarup, J. Pass, M. Ferreira, S. Shikov, M. Mikolajczyk, Y. Abe, G. Barbato, A.M. Giannetti, G. Krishnamoorthy, B. Beusink, D. Satpaev, T. Tsang, E. Fang, J. Partridge, S. Brohawn, J. Horn, O. Pritsch, G. Obal, S. Nilapwar, B. Busby, G. Gutierrez-Sanchez, R. Das Gupta, S. Canepa, K. Witte, Z. Nikolovska-Coleska, Y.H. Cho, R. D'Agata, K. Schlick, R. Calvert, E.M. Munoz, M.J. Hernaiz, T. Bravman, M. Dines, M.H. Yang, A. Puskas, E. Boni, J. Li, M. Wear, A. Grinberg, J. Baardsnes, O. Dolezal, M. Gainey, H. Anderson, J. Peng, M. Lewis, P. Spies, Q. Trinh, S. Bibikov, J. Raymond, M. Yousef, V. Chandrasekaran, Y. Feng, A. Emerick, S. Mundodo, R. Guimaraes, K. McGirr, Y.J. Li, H. Hughes, H. Mantz, R. Skrabana, M. Witmer, J. Ballard, L. Martin, P. Skladal, G. Korza, I. Laird-Offringa, C.S. Lee, A. Khadir, F. Podlaski, P. Neuner, J. Rothacker, A. Rafique, N. Dankbar, P. Kainz, E. Gedig, M. Vuyisich, C. Boozer, N. Ly, M. Toews, A. Uren, O. Kalyuzhniy, K. Lewis, E. Chomey, B.J. Pak, D.G. Myszka, A global benchmark study using affinity-based biosensors, Anal. Biochem. 386 (2009) 194–216. https://doi.org/10.1016/j.ab.2008.11.021.

[14] H.T.M. Phan, S. Bartelt-hunt, K.B. Rodenhausen, M. Schubert, J.C. Bartz, Investigation of Bovine Serum Albumin (BSA) Attachment onto Self-Assembled Monolayers (SAMs) Using Combinatorial Quartz Crystal Microbalance with Dissipation (QCM-D) and Spectroscopic Ellipsometry (SE), (2015). https://doi.org/10.1371/journal.pone.0141282.

[15] Z. Yang, H. Peng, W. Wang, T. Liu, Crystallization behavior of poly(ε-caprolactone)/layered double hydroxide nanocomposites, J. Appl. Polym. Sci. 116 (2010) 2658–2667. https://doi.org/10.1002/app.

[16] M. Ali, S. Nasseri, M. Ulbricht, Fouling effects of humic and alginic acids in nano fi ltration and in fl uence of solution composition , 250 (2010) 688–692. https://doi.org/10.1016/j.desal.2009.05.021.

[17] A.E. Contreras, Z. Steiner, J. Miao, R. Kasher, Q. Li, Studying the role of common membrane surface functionalities on adsorption and cleaning of organic foulants using QCM-D, Environ. Sci. Technol. 45 (2011) 6309–6315. https://doi.org/10.1021/es200570t.

[18] S. Yadav, I. Ibrar, S. Bakly, D. Khanafer, A. Altaee, V.C. Padmanaban, A.K. Samal, A.H. Hawari, Organic fouling in forward osmosis: A comprehensive review, Water (Switzerland). 12 (2020). https://doi.org/10.3390/w12051505.

[19] M. Hashino, K. Hirami, T. Katagiri, N. Kubota, Y. Ohmukai, T. Ishigami, T. Maruyama, H. Matsuyama, Effects of three natural organic matter types on cellulose acetate butyrate microfiltration membrane fouling, J. Memb. Sci. 379 (2011) 233–238. https://doi.org/10.1016/j.memsci.2011.05.068.

[20] J. Wu, A.E. Contreras, Q. Li, Studying the impact of RO membrane surface functional groups on alginate fouling in seawater desalination, J. Memb. Sci. 458 (2014) 120–127. https://doi.org/10.1016/j.memsci.2014.01.056.

[21] I. Bhushan, R. Parshad, G.N. Qazi, V.K. Gupta, Immobilization of lipase by entrapment in Ca-alginate beads, J. Bioact. Compat. Polym. 23 (2008) 552–562. https://doi.org/10.1177/0883911508097866.

[22] S.T. Kelly, A.L. Zydney, Mechanisms for BSA fouling during microfiltration, J. Memb. Sci. 107 (1995) 115–127. https://doi.org/10.1016/0376-7388(95)00108-O.

[23] I.H. Huisman, P. Prádanos, A. Hernández, The effect of protein-protein and protein-membrane interactions on membrane fouling in ultrafiltration, J. Memb. Sci. 179 (2000) 79–90. https://doi.org/10.1016/S0376-7388(00)00501-9.

[24] B. Mi, M. Elimelech, Chemical and physical aspects of organic fouling of forward osmosis membranes, J. Memb. Sci. 320 (2008) 292–302. https://doi.org/10.1016/j.memsci.2008.04.036.

[25] Q. Li, Z. Xu, I. Pinnau, Fouling of reverse osmosis membranes by biopolymers in wastewater secondary effluent: Role of membrane surface properties and initial permeate flux, J. Memb. Sci. 290 (2007) 173–181. https://doi.org/10.1016/j.memsci.2006.12.027.

[26] T.T. Nguyen, C. Lee, R.W. Field, I.S. Kim, Insight into organic fouling behavior in polyamide thin-film composite forward osmosis membrane: Critical flux and its impact on the economics of water reclamation, J. Memb. Sci. 606 (2020) 118118. https://doi.org/10.1016/j.memsci.2020.118118.

CHAPTER 5

MEMBRANE CLEANING MONITORING USING QCM-D AND MP-SPR

5.1. Introduction

The use of membrane processes for water production such as reverse osmosis (RO) has been exponentially increasing and nowadays they comprise 80% of the total desalination plants around the world. This number is expected to increase as RO is becoming a more cost-effective and energy-efficient method day by day [1]. However, the main limitation of membrane-based processes is membrane fouling which in turns strongly affects the permeate water flux and the membrane lifespan [2]. Great efforts have been made to minimize the negative impact of membrane fouling: while some studies focus on improving the antifouling properties of membranes by chemical modifications or by incorporation of new membrane materials such as carbon nanotubes [3,4], others adapt the operational conditions such as water flux [5]. In any case, it has become clear that all these

approaches are not efficient enough to entirely mitigate membrane fouling. For that reason, additional measures are necessary such as improving feed water quality by pre-treatment and optimized membrane cleaning strategies.

If the installation of pre-treatment stages is discarded for economic reasons, then the focus lies on optimizing the membrane cleaning strategy in order to maintain a highest possible RO-based water production efficiency.

Reversibly adsorbed fouling layers can be removed to a certain extent from the membrane surface by physical methods such as hydraulic flushing, osmotic backwashing, pulse feed flow, air scouring or ultrasound [6]. However, these methods are usually not efficient enough to completely recover the original water permeate flux. At that point chemical cleaning using detergents must be employed. For organic fouling, the type of detergent used depends on the chemical nature of the fouling layer, but most commonly used chemicals can be grouped into alkalis, acids, metal chelating agents or sequestrants, surfactants, salt solutions, and enzymes [7,8].

Alkaline solutions (hydroxides, carbonates and/or phosphates) remove organic fouling by hydrolysis and solubilization due to the electrostatic repulsion generated between the negatively charged foulants and the membrane surface due to a pH increase [9]. Metal chelating agents destabilize the fouling layer as they remove those divalent cations (such as calcium) that cause severe fouling especially with polysaccharides such as alginates

[10]. Due to their amphiphilic nature, surfactants are very useful for removing organic fouling as they form micelles around the organic molecules which then may be carried away by flushing with water [8]. Solutions of salts such as sodium chloride (NaCl) can be very efficient to eliminate gel-forming organic foulants due to ion-exchange reactions [11]. Salts solution produce structural changes and deformation of the gel-layer due to the osmotic pressure difference between the bulk solution and the internal structure of the gel-layer. This difference leads to swelling of the gel network and consequently an ion-exchange reaction between the calcium attached to polysaccharides and the sodium of the cleaning solution occurs, thus destabilizing the gel fouling layers [12].

The cleaning efficiency is determined by the type of chemical, dosage sequence of the chemical and contact time [13]. These parameters can be optimized in order to avoid excessive waste being discharged into the environment and to ensure the best performance of the cleaning process in terms of costs, efficiency and sustainability [11]. Furthermore, cleaning agents can be used either individually or in combination. In fact, most of the commercially available cleaning products are based on mixtures of the abovementioned compounds. For example, an alkali solution debilitating an organic fouling layer may be combined with a surfactant that helps dislodging foulants. Yet, in most cases the exact chemical composition of commercially available products is unknown which makes it difficult for the end-user to understand in depth the underlying cleaning mechanisms and predict

the product efficiency. On the other hand, also the composition of the actual fouling layer is often an unknown. This results in either having to find the optimum cleaning strategy by a trial and error approach or putting adequate fouling monitoring techniques in place.

A wide range of physical and chemical cleaning strategies have been studied in order to efficiently recover the membrane surface after fouling [for example, 13,21–24]. Although these approaches are very useful to further understand the mechanisms that are involved in membrane cleaning, in most cases there are not completely conclusive. For that reason, fast-screening monitoring tools for testing different membrane cleaning protocols would be highly useful. In this context, this chapter presents an approach on combining both QCM-D and MP-SPR to test different membrane cleaning strategies in a time-efficient and material-extensive manner. Three different chemical membrane cleaning protocols were investigated in order to study if the proposed combination of QCM-D/MP-SPR was capable of testing the efficiency in removing fouling by those detergents both on-line and off-line.

5.2. Results and Discussion

5.2.1. Reproducibility and thickness of pure PA ultra-thin films

Prior to studying the effect of detergents on the polyamide (PA), the PA-deposition itself was first characterized by QCM-D in order to warrant that only sensors would be used that bear a simi-

lar PA layer. Spin-coating was chosen as a quick and easy method to deposit PA onto QCM-D and MP-SPR sensor according to the protocol described in Chapter 2.

QCM-D is able to characterize the resulting PA films as for their mass and viscoelasticity. As can be observed from Figure 5.1A, the mass of deposited PA on the gold sensor and the viscoelasticity of the resulting ultra-thin PA films was highly disperse. The average shift in the frequency upon PA deposition was 420 ± 138 Hz. There was no obvious correlation between the mass of PA deposited and the energy dissipation of the resulting film. This scatter within the ΔD-ΔF plot could be attributed to slightly varying solvent evaporation conditions during spin-coating which invariably occur when using a basic spin-coating set-up. However, as has been discussed in Chapter 3, this was not a limitation for studying surface-sensitive phenomena as long as coating of the sensor by PA could be warranted.

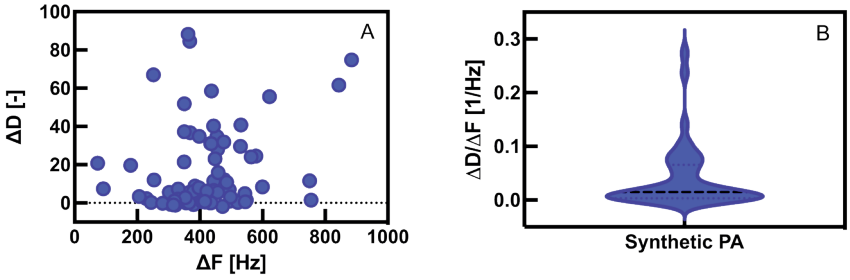

Figure 5.1. A: Dissipation ΔD represented as a function of the frequency ΔF of the PA ultra-thin film; **B**: Violin-plot of the variation of the ΔD/ΔF ratio of the unmodified PA ultra-thin films.

As depicted in Figure 5.1B, the ΔD/ΔF ratio of the deposited PA ultra-thin films remained above 0,4 Hz^{-1}. Because for a 5MHz QCM-D sensor a layer could be approximated as rigid for ΔD/ΔF values lower than $4x10^{-7}$ Hz^{-1} [18], this suggested that the PA films formed could be considered as rigid films. As a consequence, the thickness of these ultra-thin PA films could be estimated according to the Sauerbrey equation (Equation 2.5, Chapter 2). The average film thickness calculated was 75 nm for the polymer deposited with the major part of films having a thickness between 55 and 90 nm (Figure 5.2).

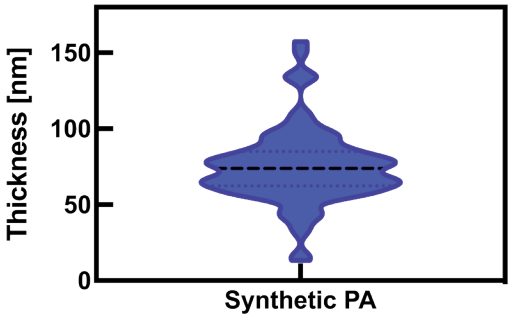

Figure 5.2. Violin-plot of the variation of the thickness of the PA ultra-thin film deposition on QCM-D gold sensor surface.

The minimum film thickness measured was 16 nm and still yielding a robust coverage of the QCM-D sensor with PA. Nevertheless, for the subsequent cleaning studies only sensors with a film-thickness between 50-90 nm were used in order to avoid any possible artefacts (e.g., pinhole formation in the PA-film).

5.2.2. Fouling and chemical cleaning measurements

Carrying out a correct membrane cleaning protocol is essential for maintaining membrane properties such as permeability and selectivity [16]. Three different cleaning protocols were tested to study how the generated organic fouling was removed from the unmodified PA-coated sensor surface. The cleaning process was monitored using both QCM-D and MP-SPR. The representative foulants used were bovine serum albumin (BSA), sodium alginate (ALG) and humic acid (HA), respectively. Cleaning agents comprised both a commercial (CAS1) and a custom-made alkaline solutions (AS2) as well as a commercial enzymatic solution (CES) specifically formulated for protein removal (for details, see Chapter 2).

5.2.3. Study of the effect of cleaning agents on the pristine PA

Cleaning agents do not only act on the fouling layer but may also alter the physical and chemical properties of the membranes, thus affecting the subsequent membrane performance [19,20]. Therefore, it was investigated by both QCM-D and MP-SPR in a first set of experiments whether the cleaning agents caused any change or damage into the PA layer. These measurements were carried out with all the aforementioned cleaning agents.

5.2.3.1.Interaction between the custom-made alkaline solution (AS2) and PA

Figure 5.3 depicts the raw data of a measurement performed with QCM-D using the AS2 detergent and a PA-coated QCM-D sensor. This measurement is shown as a representative example of four identical independent measurements.

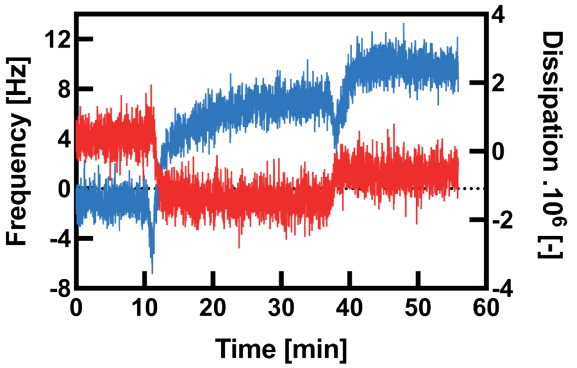

Figure 5.3. Raw data of the QCM-D measurement performed to study the interaction between the AS2 cleaning detergent and the unmodified PA. Steps of the experiment: stabilization of the baseline in ultra-pure water for 10 minutes; injection of the AS2 detergent for 30 minutes; rinsing with ultra-pure water after 40 minutes of experimentation.

From Figure 5.3 it can be observed that after the rinsing step (after 40 min), the frequency remained about 10 Hz above the baseline and the dissipation decreased slightly. This is indicative for a loss of material. Hence, detergent AS2 apparently damaged the PA deposited on the QCM-D sensor surface.

Table 5.1. Comparison between the deposited PA on the QCM-D sensors and the amount of PA removed after the rinsing step.

QCM-D test	Deposited PA [Hz]	Removed PA [Hz]	Removed PA [%]
Test 1 (PA-AS2)	645,3	10,3	1,6
Test 2 (PA-AS2)	672,4	9,1	1,3
Test 3 (PA-AS2)	718,2	6,4	0,9
Test 4 (PA-AS2)	628,6	6,7	1,1
Average Tests 1-4	661,1±39,1	8,1±1,9	1,2±0,3

After the rinsing step with ultra-pure water, an average frequency shift of 8,1±1,9 Hz was measured. Considering that the average amount of the PA deposited on the QCM-D sensor surface was 661,1±39,1 Hz, the calculated percentage of the PA removed was 1,2±0,3% (Table 5.1). The average frequency shift of 8,1±1,9 Hz of removed PA corresponds to approximately 143±34 ng·cm^{-2} or about 1,3±0,3 nm. However, it should be borne in mind that this value might be overestimated because QCM-D does not only detect removal of PA but also the respective removal of water absorbed in PA. The latter might amount to about 10% in weight of the PA [21].

Interestingly, also the bulk response was positive for the frequency and negative for the dissipation (Figure 5.3). Owing to its composition, AS2 will have a slightly higher density than water which should consequently generate a negative and positive bulk response in the frequency and the dissipation, respectively. The opposite occurred which may be explained by the apparent

bulk response observed being the sum of the negative frequency change due to a change in bulk density and the positive frequency change due to removal of polyamide. These two phenomena cannot be distinguished within the QCM-D measurement and only the net change is measured.

The same experiments were therefore carried out using MP-SPR as a complementary technique. In this case, three identical measurements were performed of which the raw data of one are depicted as an example in Figure 5.4. As can be observed, after the rinsing step (starting at 50 minutes), the change in the resonance angle measured by MP-SPR remained below the baseline for all wavelengths. The latter means that the PA layer deposited onto the sensor was partially removed. This observation agreed with data from QCM-D (Figure 5.3).

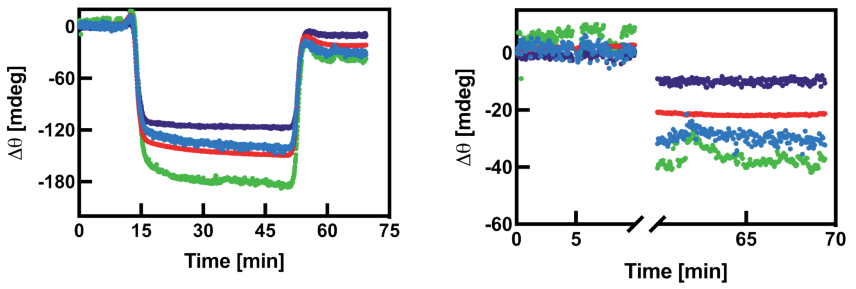

Figure 5.4. Raw data of the measured interaction between the AS2 cleaning detergent and the unmodified PA considering the contribution of the bulk change due to the exposure of PA to the detergent (left) and without the bulk contribution (right). Steps of the experiment: stabilization of the baseline in ultra-pure water during 15 minutes; injection of the AS2 detergent for 35 minutes; subsequent rinsing with ultra-pure water. Different curves represent measurements of different wavelengths (blue and green: 670 nm; red: 785 nm; purple: 980 nm).

Different sensors of varying amount of deposited PA were then prepared for investigating a possible relationship between the deposited PA film thickness and the PA removed after exposure to AS2 cleaning agent. It would be expected that the PA removal rate were independent of the thickness of the PA layer. As can be seen from Table 5.2, this was in fact the case. The average amount of the PA removed was 28,6±6,5 mdeg (Table 5.2) irrespective of the thickness of the PA layer. It corresponded to a percentage of PA removed ranging from 0,7 to 16,7% of the original amount of PA deposited.

Table 5.2. Comparison between the deposited PA onto the MP-SPR sensors and the amount of PA removed after the rinsing step. For each test, two results were obtained for the same wavelength of 670 nm (channel 1 and 3 of the MP-SPR).

MP-SPR test	Deposited PA [mdeg]	Removed PA [mdeg]	Removed PA [%]
Test 1-1	4520	30	0,7
Test 1-2	3580	40	1,1
Test 2-1	1110	25	2,3
Test 2-2	1140	25	2,2
Test 3-1	180	30	16,7
Test 3-2	140	21,5	15,4

Hence, both QCM-D and MP-SPR proved that upon exposure to the detergent AS2 the PA was damaged. This is in line with some studies in literature that have reported that thin-film composite polyamide-based RO membranes are very sensitive to high pH solutions such as AS2 while they are very resistant to low pH

cleaning agents [22]. The PA removal of 28,6±6,5 mdeg as measured by MP-SPR would correspond to approximately 24±5 $ng \cdot cm^{-2}$ or 0,2 nm which is significantly lower than what was measured with QCM-D (143±34 $ng \cdot cm^{-2}$ or about 1,3±0,3 nm), even if allowing for the contribution of water in the latter. Nevertheless, with the thickness of the selective PA-layer of a TFC membrane used in reverse osmosis ranging typically from 20-200 nm [23–25], this clearly illustrates how repeated exposure to cleaning agents can significantly reduce membrane lifetime. Indeed, the AS2 solution is considered to represent a harsh cleaning regime [26].

Similarly to what was observed with QCM-D, also in MP-SPR the bulk response was the opposite of what would be expected: as the refractive index of the NaOH/SDS-based solution is higher than that of water, it should generate a positive SPR-angle change. What is more, the negative SPR-angle of the bulk change is significantly more pronounced than during subsequent rinsing, as opposed to what was detected with QCM-D (Figure 5.3). A possible explanation is that during cleaning AS2 acts on the PA-layer as a swelling agent, reducing locally the refractive index which in turn results in a temporary lower SPR-angle. This would be in line with considerations made before on the results obtained by QCM-D where an additional uptake of water by PA (swelling) along with the bulk response would be perceived as a negative frequency change contribution overcompensated by the PA removal.

5.2.3.2.Interaction between the commercial alkaline solution (CAS1) and PA

CAS1 is a cleaning agent of high pH (11-12) which is commercialized for the removal of organic fouling and particularly proteins as it promotes their hydrolysis. CAS1 contains pyrophosphates in order to control scale formation, to act as a dispersant agent and to control the final pH of the solution.

Figure 5.5 shows raw data of a QCM-D measurement performed with the CAS1 commercial detergent and a PA-coated sensor. First, the PA sensor was stabilized in ultra-pure water for 10 minutes before injecting the CAS1 detergent. The injection of CAS1 was followed by a rinsing step with ultra-pure water in order to see whether exposure to CAS1 would also damage the PA layer as was seen with AS2.

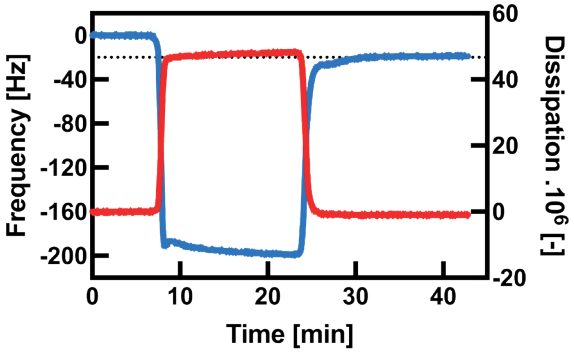

Figure 5.5. Raw data of the interaction of CAS1 cleaning detergent with PA as measured by QCM-D. Steps of the experiment: stabilization of the baseline in ultra-pure water (about 8 min), injection of the CAS1 detergent (about 15 min) and rinsing with ultra-pure water (about 20 min).

A high bulk response was observed in both the frequency (≈ 200 Hz) and dissipation (≈ 45) during the injection of CAS1 cleaning agent, as opposed to cleaning agent AS2 (Figure 5.3). However, attention is drawn to the fact that CAS1 was significantly more concentrated than AS2 (see Chapter 2). After rinsing, it became apparent that constituents of the detergent had adsorbed on the PA layer surface. In fact, a significant average frequency shift of 19,6 ± 1,7 was observed in all these measurements corresponding to an average adsorbed mass per area of 347 ± 30 $ng \cdot cm^{-2}$. Taking into account the composition of CAS1, one may conclude that pyrophosphate molecules that are present in this commercial cleaning product could interact via their cation with the PA surface. The latter should be borne in mind when evaluating the foulant removal capacity of CAS1 in Section 5.2.5. It was furthermore speculated whether the apparent adsorption of pyrophosphates could possibly mask damage to PA that might occur concurrently. Pyrophosphates can be expected to have a high degree of hydration and since QCM-D measures surface-layer associated water, the adsorption could overcompensate removal of PA.

The same experiments were therefore carried out with MP-SPR. Figure 5.6 reveals that the PA deposited onto the MP-SPR sensor was apparently damaged due to its exposure to CAS1 detergent as the resonance angle remained below the baseline for all the wavelengths after rinsing (Figure 5.6B). This observation was opposite to QCM-D data (Figure 5.5). A possible explanation is that water molecules associated to highly hydrated pyrophos-

phates contributed to an additional mass big enough such as to generate an overall decrease in the frequency despite removal of PA. This corroborates one more time the complementarity of both techniques for studying membrane surface phenomena.

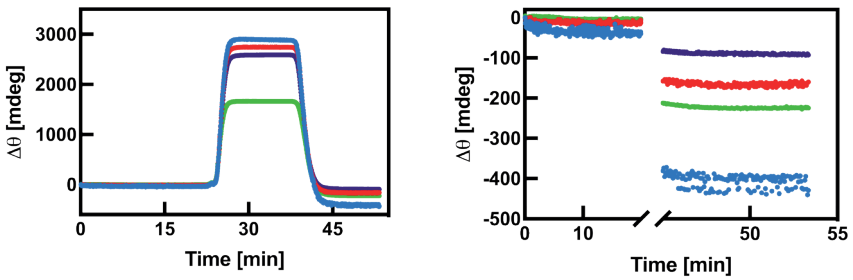

Figure 5.6. Left: raw data of the adsorption of CAS1 cleaning detergent on the unmodified PA measured by MP-SPR and considering the contribution of the bulk. **Right:** same experiment without the contribution of the bulk. Different curves represent measurements of different wavelengths (blue and green: 670 nm; red: 785 nm; purple: 980 nm). Steps of the experiment: stabilization of the baseline in ultra-pure water (about 15 min), injection of the CAS1 detergent (about 30 min) and finally rinsing with ultra-pure water.

The amount of PA apparently removed from the PA surface was in this case about 400 mdeg for channel 1 and 210 mdeg for channel 3 (which would correspond approximately to 333 and 175 ng·cm^{-2}, respectively). These values are much more higher than those obtained with AS2 detergent (an average of about 28,6 mdeg, see Table 5.2) which is, however, in line with the fact that CAS1 was a far stronger alkaline solution than AS2 resulting in an expectedly higher damage of PA.

5.2.3.3. Interaction between the commercial enzymatic solution (CES) and polyamide

Enzymes can specifically degrade biological macromolecules under milder cleaning conditions as regards pH and temperature, bearing furthermore the advantage of being biodegradable and biocompatible cleaning agents [12]. As can be observed in Figures 5.7 and 5.8, the exposure of PA to a commercial enzymatic cleaning solution (CES) caused an expected high bulk response due to a density change followed by a final decrease in the frequency of 35,1 Hz (corresponding to about 621,3 ng·cm^{-2}), indicating that enzymes remained adsorbed on the PA surface.

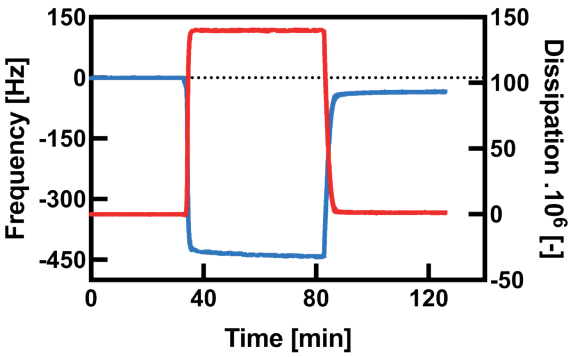

Figure 5.7. Raw data of the adsorption of CES cleaning detergent on the unmodified PA measured by QCM-D. Steps of the experiment: stabilization of the baseline in ultra-pure water for about 30 minutes, injection of the CES detergent for about 40 minutes and rinsing with ultra-pure water.

This observation was not very surprising because it is commonly known that enzymes can be adsorbed on polyamide membranes by hydrophobic interactions and act as a substrate to promote further bio-

fouling development [27]. Besides, as was shown in the Chapter 3 (Figure 8B), BSA as a model protein adsorbed to a similar amount on PA.

MP-SPR confirmed this observation (Figure 5.8). As can be seen, after an expected positive bulk change the change in the resonance angle after the rinsing remained above the baseline indicating an adsorption of enzymes onto the PA-coated sensor. The SPR-angle change for the 670 nm wavelength was 300 (blue line) and 237 mdeg (green line), corresponding to 250 and 197 ng·cm^{-2}, respectively. Also in this case these data agree well with the adsorption measured for BSA in Chapter 3 (Figure 12B). As a conclusion, the commercial enzyme solution might be an efficient cleaning agent but it generates fouling itself on the PA membrane surface. Its use would therefore most probably only be justified if it manages to eliminate thick fouling layers. In this case residual detergent adsorbed to the PA surface would be the lesser of two evils.

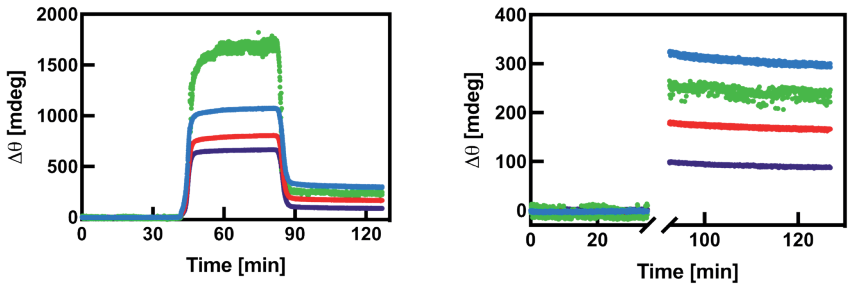

Figure 5.8. Left: raw data of the adsorption of CES cleaning detergent on the unmodified PA measured by MP-SPR and considering the contribution of the bulk. **Right:** same experiment without the contribution of the bulk. Different curves represent measurements of different wavelengths (blue and green: 670 nm; red: 785 nm; purple: 980 nm). Steps of the experiment: stabilization of the baseline in ultra-pure water (about 30 min); injection of the CES detergent (about 55 min) and finally rinsing with ultra-pure water.

5.2.4. Monitoring of membrane cleaning in real-time

From a membrane-process point of view, on-line monitoring of membrane cleaning is very relevant in order to observe its efficiency in real time and in this way optimize the duration of the cleaning. For verifying the actuation of cleaning detergents or determining in how far they damage the membrane polymer, off-line monitoring is sufficient and more suitable. For both cases, QCM-D and MP-SPR are compared for complementarity but emphasis is put on the potential of using either or both techniques as on-line membrane fouling detection techniques.

5.2.4.1. Toward on-line monitoring of cleaning using QCM-D

The fundamental frequency (f0) of a QCM-D sensor refers to the lowest frequency where the crystal can be exited to resonance and it depends among other parameters on the sensing depth. For a 5 MHz QCM-D sensor the amplitude of the base harmonic can penetrate about 250 nm into the liquid [28]. This means that although QCM-D is a surface-sensitive technique, the measured signal can be affected by bulk responses.

During a cleaning experiment, the detergent generates a change in the bulk properties of the liquid which is in contact with the sensor surface, amongst which density and viscosity. QCM-D is sensitive to changes of the latter. Therefore, as density and viscosity of the liquid entering into the QCM-D

microfluidic module increase during cleaning, there will be an inevitable bulk response in both frequency and dissipation which generally decreases and increases, respectively [29]. Thus, the question arises whether despite such a bulk response to the cleaning agent QCM-D maintains its surface-sensitivity of whether surface phenomena are masked by the bulk (Figure 5.9.). In the former case, it would be possible to detect cleaning and related phenomena already during the bulk response and one could in this way monitor its efficiency in real-time.

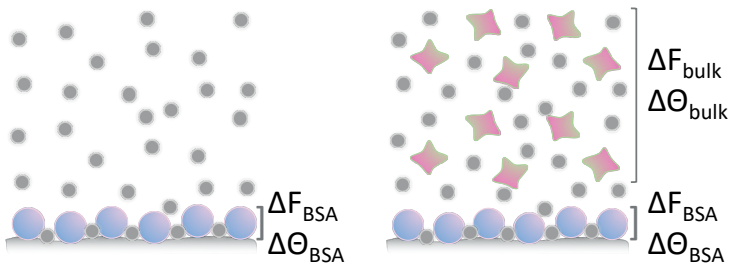

Figure 5.9. Schematic illustration of bulk effects when measuring with QCM-D or MP-SPR. **Left:** the adsorption of a monolayer of BSA protein generates a shift in frequency or SPR-angle during measurement; the bulk is "invisible" as it represents reference conditions. **Right:** during a change of the bulk solution, the measured overall shift in frequency or SPR-angle is the contribution of both the adsorption of BSA and the bulk change due (density and viscosity for QCM-D, refractive index for MP-SPR).

In order to verify the effect of the bulk response on measuring the cleaning efficiency, on both QCM-D and MP-SPR the two pa-

rameters were compared (Figure 5.10): on one hand, $\Delta F_{cleaning,buffer}$ or $\Delta\Theta_{cleaning,buffer}$ comprises the removal of foulant (and also possibly polymer) and is measured in reference conditions before and after the bulk change due to cleaning. On the other hand, $\Delta F_{cleaning,bulk}$ and $\Delta\Theta_{cleaning,bulk}$ comprises the removal of foulant (and also possibly polymer) but is measured during the bulk response, i.e. cleaning.

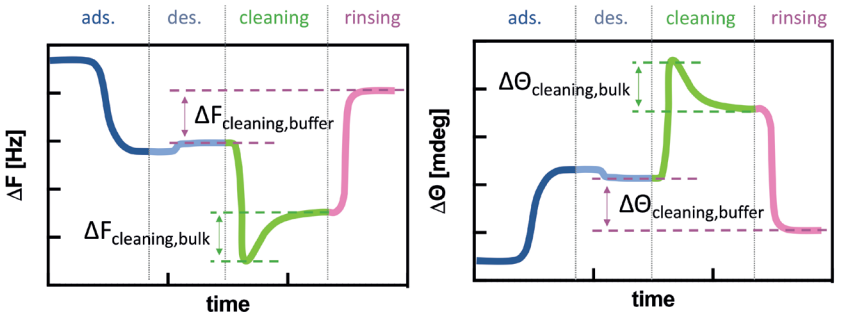

Figure 5.10. Schematic illustration of a typical fouling and cleaning experiment by QCM-D (left) and MP-SPR (right). The different intervals are adsorption of foulant after baseline (reference) measurement, “ads.”; desorption of loosely bound foulant under reference conditions, “des.”; injection of cleaning agent going along with a bulk change, “cleaning”; final rinsing under reference conditions, “rinsing”.

As an example, Figure 5.11 illustrates an experiment performed by QCM-D using BSA as a model foulant and AS2 alkaline solution as a model cleaning detergent.

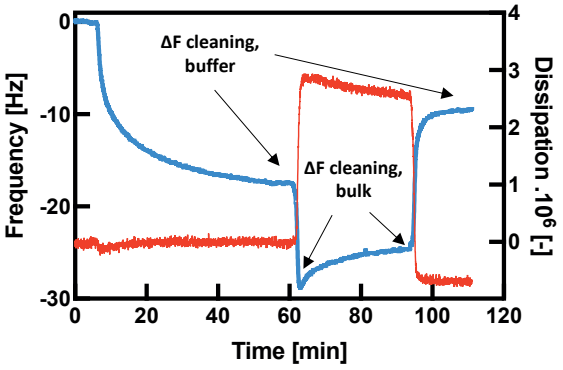

Figure 5.11. Raw data of the adsorption of BSA foulant on PA-coated QCM-D sensor and subsequent cleaning measurement using AS2 alkaline solution as a model detergent. Measurements steps: (1) Stabilization of the baseline in PBS buffer; (2) adsorption of BSA protein; (3) desorption of reversibly bound protein molecules after rinsing with PBS buffer; (4) injection of AS2 detergent and (5) rinsing with PBS buffer.

As can be observed, the BSA adsorbed irreversibly with about 18 Hz onto the PA-coated QCM-D sensor. After the rinsing step with buffer, another decrease in the frequency occurred during injection of detergent AS2. This frequency decrease corresponded to a bulk response generated by the detergent. It could be observed that $\Delta F_{cleaning,bulk}$ was smaller than $\Delta F_{cleaning,buffer}$. The latter means that apparently the bulk response masks to some extent surface phenomena.

In order to investigate deeper the effect of the bulk on the removal of fouling layer, 26 identical independent measurements were performed. In all these experiments it could be seen that the $\Delta F_{cleaning,\ bulk}$ was always smaller than $\Delta F_{cleaning,buffer}$.

However, both parameters were linearly correlated (Figure 5.12).

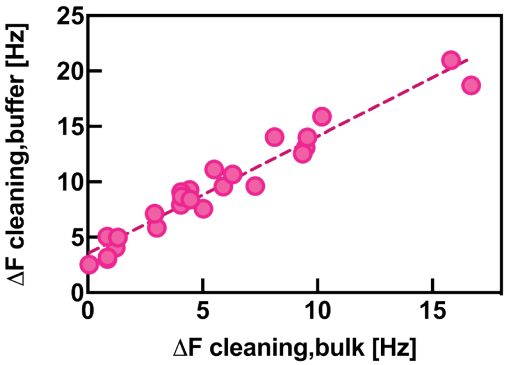

Figure 5.12. Correlation between the BSA removal determined based on reference conditions ($\Delta F_{cleaning,buffer}$) and the BSA removal measured in real time during the cleaning process in presence of a bulk change ($\Delta F_{cleaning,bulk}$); data refer to QCM-D.

The fit of these 26 parameters yielded the empirical correlation

$$\Delta F_{cleaning,buffer} = \Delta F_{cleaning,bulk} + 3{,}7\ [Hz] \qquad \textbf{Equation 5.1}$$

This means that the sensor maintained its surface sensitivity despite the additional contribution of the bulk response due to the detergent injection, but with a threshold of 3,7 Hz (in the case of AS2 solution). Hence, membrane cleaning can be monitored in real-time by QCM-D and so can the fouling removal. With the above equation, it is possible to fit the steady state values of Figure 5.11 using the values for fouling, bulk response, and cleaning efficiency (Figure 5.13):

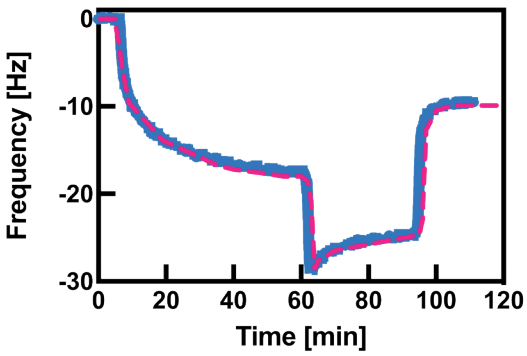

Figure 5.13. Comparison between cleaning experiment using BSA as a model foulant and AS2 as cleaning agent (data as in Figure 5.11, blue curve) and a predicted experiment based on steady-state values of the most relevant events (dashed red line). The transient regimes were not modelled but simulated for illustration purpose.

With this simple empirical model, different scenarios can be simulated in order to primarily predict how different degrees of cleaning efficiency, attack of the PA polymer layer and fouling by the detergent itself would generate different patterns of the fouling-cleaning curves. Figure 5.14 illustrates that the resulting patterns during the bulk response are very distinct and recognizable for two cleaning efficiencies, namely 50% and 100%, respectively, and as such permit a quick evaluation of the progress and nature of the cleaning process in real time.

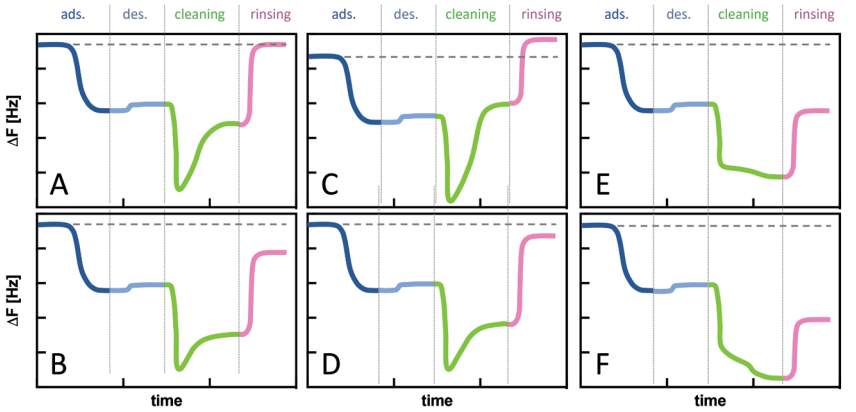

Figure 5.14. Upper row: 100% cleaning efficiency; bottom row: 50% cleaning efficiency. **A,B:** neither fouling nor PA attack by detergent (ideal); **C,D:** no fouling but PA attack by detergent; **E,F:** no PA attack but fouling by detergent equal in amount to the initial adsorption step.

One important feature of QCM-D is that it allows measuring different frequency overtones or harmonics which can be useful for studying the viscoelastic properties of a material. Each harmonic acquires information from a different perspective of the same material as they measure with different sensitivity and penetration depth. The crystal oscillation is focused to the part of the sensor where the two electrodes overlap. As a consequence, the maximum oscillation amplitude is reached in the middle of the sensor and it decreases in a Gaussian manner towards the edges [30]. The width of the bell curve varies depending on harmonic number “n”. By increasing the harmonic number “n”, the oscillation amplitude and, hence, penetration depth at the sensor surface decreases (Figure 5.15). In addition, the higher the harmonic, the sharper is the Gaussian curve [31]. This means that lower harmonics are more sensitive than higher

ones because their bell curve is wider and therefore collects more information on the phenomena occurring at the sensor surface. On the contrary, higher harmonics have a smaller amplitude (sharper Gaussian) and cover less sensor surface being therefore less sensitive to surface phenomena [32,33].

Thus, taking into account that both the sensitivity and the penetration depth of all the harmonics differ, the question arises whether any differences would be observed between the 5th harmonic (data of which are reported throughout this thesis) and a higher overtone (for example 9th, 11th, or 13th) during the bulk measurement of the cleaning step. The underlying hypothesis is that since the higher harmonic has a lower amplitude and penetration depth, it could be possibly less affected by bulk effects (Figure 5.15).

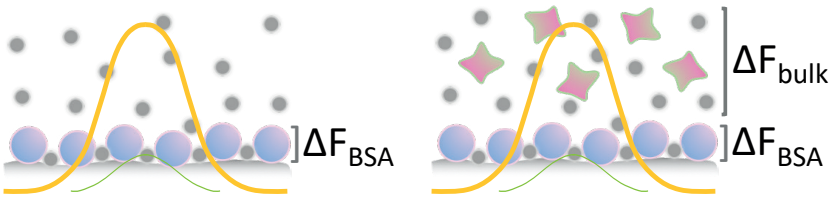

Figure 5.15. Schematic representation of the change in the penetration depth and sensitivity of different harmonics. Green curve represents the higher harmonic, the orange curve the lower one. The grey shade at the bottom represents the polyamide layer on the sensor surface. **Left:** The adsorption of a monolayer of BSA on PA generates a frequency shift during measurement. **Right:** The measured frequency shift is the contribution of both the adsorption of BSA on PA and the bulk change due to the injection of the cleaning agent. The hypothesis depicted is that the higher harmonic is less affected by changes in the bulk due to a reduced penetration depth.

Figure 5.16 compares the response of higher harmonics (9th, 11th and 13th) with the 5th which it is usually considered for data interpretation.

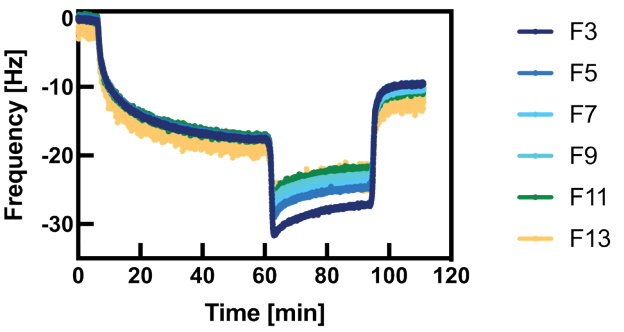

Figure 5.16. Comparison between different harmonics measured by QCM-D for fouling-cleaning experiment performed with BSA as a model foulant and AS2 as cleaning agent. Each color represent a different harmonic.

As can be observed, the bulk response in the cleaning step is highest for the 3rd harmonic (F3, dark blue curve) and lowest for the higher harmonics, as was the initial hypothesis. However, it can also be seen that higher harmonics still have a bulk response, even though to a lesser degree. In fact, there is a decrease of bulk effect from the 3rd to the 9th harmonic (F3 to F9), but then both 11th and 13th harmonics (F11 and F13) are practically identical with the only difference that the 13th harmonic has much more noise.

Furthermore, the difference between the measured frequency at the beginning and the end of the bulk response (equal to what is denoted $\Delta F_{cleaning,bulk}$ in Figure 5.10) is practically the

same for all the harmonics. This means that the bulk affects all of them equally. Thus, there is apparently no point in using higher harmonics.

5.2.4.2. Toward on-line monitoring of cleaning using MP-SPR

MP-SPR was used as a complementary tool for monitoring cleaning experiments. The aim was to study whether the cleaning can be followed during the bulk response similarly as studied with QCM-D. Figure 5.17 depicts raw data of a typical fouling-cleaning experiment performed by MP-SPR measured with the wavelength of 670 nm (channel 1 and 3). As in QCM-D, the model foulant employed was BSA protein and the cleaning agent was the AS2 alkaline solution.

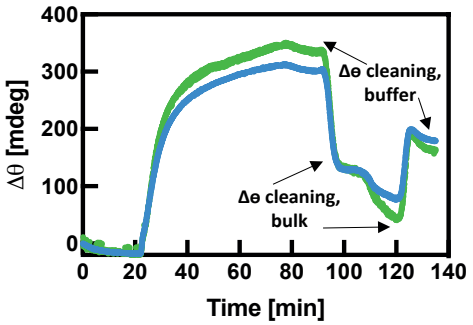

Figure 5.17. Raw data of the adsorption of BSA foulant on a PA-coated MP-SPR sensor and subsequent cleaning measurement using AS2 alkaline solution as a model detergent. Measurements steps: (1) Stabilization of the baseline in PBS buffer (20 min); (2) adsorption of BSA protein (until 70 min); (3) desorption of reversibly bound protein molecules by rinsing with PBS buffer (until 85 min); (4) injection of detergent AS2 (85-120 min); (5) rinsing with PBS buffer. Both curves correspond to a wavelength of 670 nm in channel 1 (blue curve) and channel 3 (green curve), respectively.

As can be observed, after the desorption step (at 85 minutes) the BSA that had remained irreversibly adsorbed on the PA surface yielded an angle change of 320 and 330 mdeg for channels 1 and 3, respectively. During subsequent injection of detergent AS2, a $\Delta\theta_{cleaning,bulk}$ of 60 mdeg and 100 mdeg was measured for channel 1 and channel 3, respectively. However, after rinsing with PBS buffer the amount of BSA removed ($\Delta\theta_{cleaning,buffer}$) was 120 and 160 mdeg for channels 1 and 3, respectively, i.e. on average 1,75 times more. This agrees with previous QCM-D measurements, namely that $\Delta\theta_{cleaning,bulk}$ is smaller than $\Delta\theta_{cleaning,buffer}$. Therefore, the bulk response measured with MP-SPR apparently also masks to some extent surface phenomena but real-time monitoring of the cleaning remains possible. Based on various experiments, also for MP-SPR a correlation between the change in peak minimum angle generated due to BSA removal ($\Delta\theta_{cleaning,buffer}$) and during the bulk response ($\Delta\theta_{cleaning,bulk}$) was found for the wavelength of 670 nm (Figure 5.18).

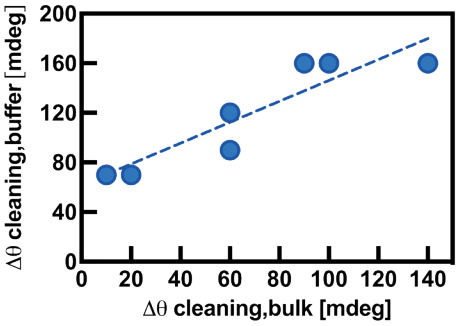

Figure 5.18. Correlation between the measured BSA removal after the cleaning step ($\Delta\theta c_{leaning,buffer}$) and the measured BSA removed during the cleaning process in the bulk ($\Delta\theta_{cleaning,bulk}$) for the wavelength of 670 nm (channels 1 and 3).

The simple empirical correlation between $\Delta\theta_{cleaning,bulk}$ and $\Delta\theta_{cleaning,buffer}$ was:

$$\Delta\theta_{cleaning,buffer} = 0{,}8 \cdot \Delta\theta_{cleaning,bulk} + 61{,}9\ [mdeg]$$ **Equation 5.2**

Hence, very similarly to what was observed with QCM-D, bulk changes affect the MP-SPR signal (peak minimum angle) but membrane cleaning can be monitored in real-time although with a perception threshold of 61,9 mdeg.

Interestingly, the thresholds of 3,7 Hz (QCM-D) and 61,9 mdeg (MP-SPR) correspond to very similar approximated surface densities (mass per area): 65,5 and 51,6 ng·cm^{-2}, respectively. This reveals that at least in terms of sensitivity both QCM-D and MP-SPR are equally suitable to monitor membrane cleaning in real-time and under changing bulk conditions.

Conceptually not unlike the harmonics of QCM-D, MP-SPR uses different wavelengths of different energy and penetration depth. The energy accumulated in the glass/gold interface of the sensor due to the total internal reflection (TIR) phenomenon generates the so-called the evanescent field or wave (see Chapter 2). The amplitude of the evanescent wave decreases exponentially with increasing distance from the interface surface [34] and by varying the wavelength the penetration depth of the evanescent wave will change. Hence, the wavelength of 980 nm (channel 4) protrudes more than that of 670 nm (channels 1 and 3) into the bulk while the latter is of higher energy than the former. Similar-

ly to investigating with QCM-D whether certain harmonics are less prone to be affected by bulk changes, it was investigated whether any of the three wavelengths of the MP-SPR would be more suitable than others to monitor membrane cleaning in real-time, i.e. when the bulk conditions differ significantly from the reference.

Figure 5.19 compares the change in the resonance angle $\Delta\theta_{cleaning,bulk}$ measured by the wavelength of 980 nm (channel 4) and that of 670 nm (channels 1 and 3).

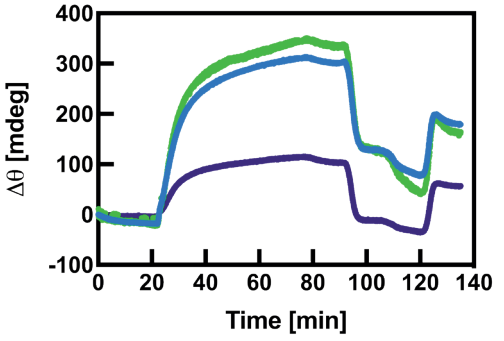

Figure 5.19. Comparison between channels 1 and 3 (670 nm, blue and green curves) and channel 4 (purple curve) for the adsorption of BSA foulant on a PA-coated MP-SPR sensor and subsequent cleaning measurement using AS2 alkaline solution as a model detergent. Measurements steps: (1) Stabilization of the baseline in PBS buffer (20 min), (2) adsorption of BSA protein (75 min), (3) desorption of reversibly bound protein molecules after rinsing with PBS buffer (90 min), (4) injection of AS2 detergent (95 min) and (5) rinsing with PBS buffer (120 min).

As can be observed, channel 4 (980 nm) has in general a lower sensitivity. The change in the resonance angle generated due

to the irreversible adsorption of BSA was 110 mdeg, while channels 1 and 3 yielded a signal on average three times higher, 320 and 330 mdeg, respectively. The approximately same ratio could be observed during the injection of AS2 detergent ($\Delta\theta_{cleaning,bulk}$(980nm) = 26 mdeg and $\Delta\theta_{cleaning,bulk}$(670nm) = 60 and 100 mdeg in channels 1 and 3, respectively) and after rinsing with PBS buffer for the total amount of BSA removed ($\Delta\theta_{cleaning,buffer}$(980nm) = 50 mdeg while $\Delta\theta_{cleaning,buffer}$(670nm) = 120 and 160 mdeg for channels 1 and 3, respectively). Thus, the wavelength of 980 nm shows a lower peak minimum angle for the bulk but to the same extent also for the detection of surface phenomena. Similarly to what was observed with different harmonics in QCM-D, there is hence no advantage in using other wavelengths than the most sensitive one which in this case is the one of 670 nm.

Summarizing, both QCM-D and MP-SPR are powerful tools for measuring membrane cleaning in real-time and under changing bulk conditions without the need to operate under reference conditions.

5.2.5. Monitoring of membrane cleaning off-line

Off-line studies of membrane cleaning are useful to validate the cleaning efficiency of a detergent. As an example, Figure 5.20 shows the removal of BSA from nitrocellulose by using the simplest possible cleaning agent, 0,1% (w/w) NaOH as measured by QCM-D (5.20A) and MP-SPR (5.20B). Nitrocellulose is a very

common polymer for bioanalytical applications (for example, lateral flow devices) while NaOH is a common surface regeneration/cleaning agent.

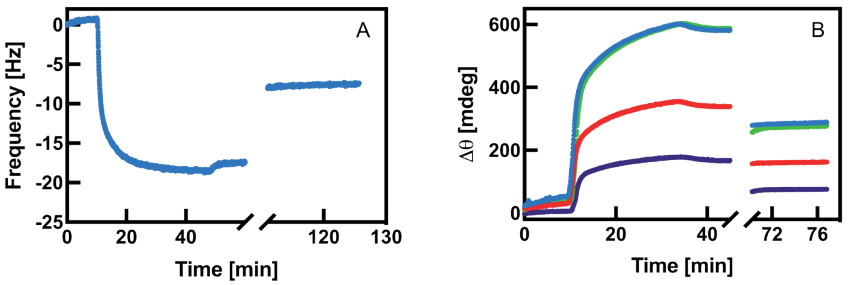

Figure 5.20. Adsorption of BSA foulant on Nitrocellulose-coated QCM-D (A) and MP-SPR sensors and subsequent cleaning step using 0,1% NaOH as detergent. Different colors represent different MP-SPR curves of varying wavelengths (B).

Nitrocellulose had been deposited on the sensor surface according to Chapter 2 followed by adsorption of BSA. The cleaning efficiencies determined by QCM-D and MP-SPR were calculated as

$$\text{cleaning efficiency } [\%] = \frac{\Delta F, \theta^*_{foulant} - \Delta F, \theta^{cleaned}_{foulant}}{\Delta F, \theta^*_{foulant}} \cdot 100$$

Equation 5.3

with $\Delta F,\theta^*_{foulant}$ referring to the foulant adsorbed on the surface before cleaning and $\Delta F,\theta^{cleaned}_{foulant}$ indicating the amount remaining after cleaning. The values obtained were 49% ± 7 and 46% ± 10, respectively, in four independent measurements and thus agreed well.

Figure 20 mainly demonstrates two aspects: first, QCM-D and MP-SPR are both suitable for studying the efficiency of cleaning agents for removing membrane fouling. Second, it clearly demonstrates that cleaning can be little efficient such that the regeneration/cleaning of a polymer surface might be incomplete. In this case, about 50% of the fouling could not be removed during cleaning.

Subsequently, the efficiency of three different membrane cleaning agents (AS2, CAS1, and CES, see Chapter 2) to remove three different foulants (BSA, ALG, and HA) from a PA surface was determined. From interviews with desalination plant operators it was known that membrane cleaning can be highly variable and inefficient. One operator even stated that from all cleaning agents available on the market, a simple alkaline solution (such as the detergent "AS2" in this work) yielded best results. The results depicted in Figure 5.21 for both QCM-D and MP-SPR entirely confirm this empirical observation.

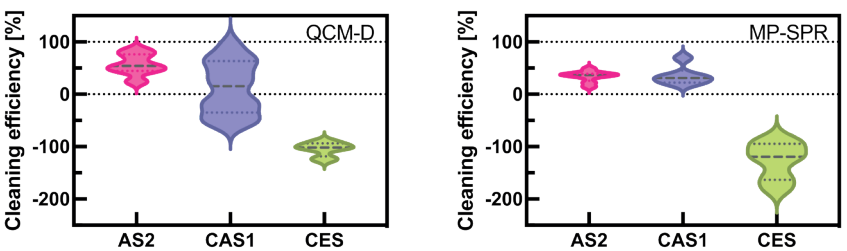

Figure 5.21. Violin-plot of the cleaning efficiency on removal of BSA of cleaning agents AS2, CAS1 and CES measured by QCM-D (left) and MP-SPR (right).

Despite a significant scatter in some of the data sets (particularly in CAS1 of QCM-D and CES in MP-SPR), which will be subject to further investigation, the alkaline solution AS2 yielded on average a cleaning efficiency of about 45-50%. It is emphasized that “cleaning efficiency” comprises both removal of foulant and possible PA membrane attack (see Section 5.2.3.1) which could explain the scatter observed. Future studies will focus on elucidating this further. On the other hand, CAS1 not only yielded the highest scatter in the QCM-D data but even reached during the latter to a significant part negative values which possibly result from adsorption of pyrophosphate and overcompensated foulant removal, if it occurred at all.

The worst performance of all three agents was CES, supposedly formulated particularly for organic fouling removal. CES did apparently not remove any BSA but rather adsorbed on the PA-BSA surface thus aggravating fouling even further. This is in line with what was found in Section 5.2.3.3.

Similar observations were made with the two other organic foulants, ALG and HA. With AS2, cleaning efficiencies were similar to what was found for BSA namely , 50% ± 5 and 36% ± 13 for QCM-D and MP-SPR, respectively, for alginate and 44% ± 9 and 38% ± 17, respectively, for humic acid. Scatter in the data was far more pronounced for the detergent CAS1 which did not yield reproducible results. A possible explanation is that fouling by alginate and humic acid had not reached steady-state during the

experiments, as opposed to BSA (please see Chapter 4, section 4.2.2 and 4.2.3.). As a consequence, the degree of fouling prior to cleaning was not only less than with BSA but the non-steady state conditions might have contributed to less reproducible fouling layers. Both aspects can be expected to detrimentally affect cleaning reproducibility.

5.2.6. Proof-of-concept of minimizing membrane fouling by an optimized cleaning strategy

The ultimate aim of using QCM-D and MP-SPR for membrane fouling monitoring is to have a tool which enables the optimization of a membrane cleaning strategy such as to mitigate as far as possible membrane fouling and furthermore minimize the use of detergent, process downtimes, and membrane damage.

For this reason, a proof-of-concept experiment was conducted using QCM-D during which a conventional cleaning strategy was compared with a predictive strategy, using BSA as a model foulant. The conventional cleaning was characterized by a fouling interval with a total duration of $\Delta t_{fouling}$ followed by a cleaning interval with a total duration of $\Delta t_{cleaning}$ (Figure 5.22). In both intervals stationary state was obtained. The membrane fouling remaining after conventional cleaning was then considered in this experiment to represent 100% of the irreversible membrane fouling.

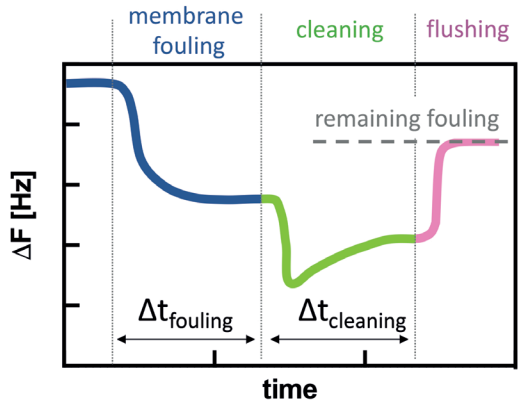

Figure 5.22. Schematic representation of a conventional cleaning measurement by QCM-D.

In a second set of experiments, a repetitive series of nine shorter fouling and cleaning intervals were conducted equaling, however, in their sum the time intervals of the previous (conventional) experiment, such as:

$$\sum \Delta t_{fouling,1}^{predictive} + \Delta t_{fouling,2}^{predictive} + \cdots + \Delta t_{fouling,9}^{predictive} = \Delta t_{fouling}^{conventional}$$

and

$$\sum \Delta t_{cleaning,1}^{predictive} + \Delta t_{cleaning,2}^{predictive} + \cdots + \Delta t_{cleaning,9}^{predictive} = \Delta t_{cleaning}^{conventional}$$

Equation 5.4

The aim was to verify the hypothesis that early-stage detection of fouling and predictive cleaning can restrain membrane fouling without increasing overall process downtimes needed for clea-

ning (see Figure 1.5). The target was, hence, to remain below the conventional target of 100% of membrane fouling.

As can be seen in Figure 5.23, the predictive cleaning maintained membrane fouling repeatedly and throughout all nine cycles at a level approximately at 50% of what would be the level of fouling using the conventional strategy.

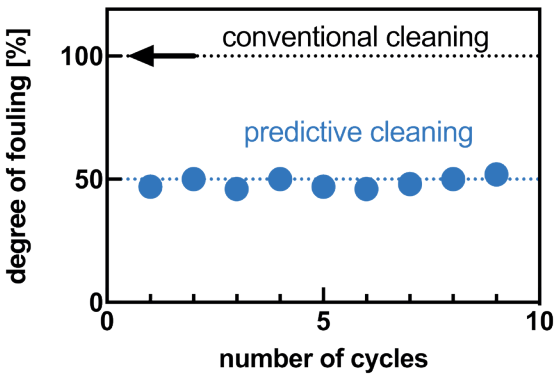

Figure 5.23. Degree of fouling after repeated predictive cleaning cycles. Blue dots represent the remained fouling degree after each cleaning step.

The steady-state fouling layer of BSA in a conventional cleaning experiment can be considered a relatively compact monolayer (Figure 5.24A). It is assumed that by cleaning the membrane before reaching the steady-state fouling, the fouling layer was not given time enough to consolidate and compact. Repeated cleaning cycles could possibly create a “patchy” fouling layer (Figure 5.24B) which can be, at least in part, more easily removed.

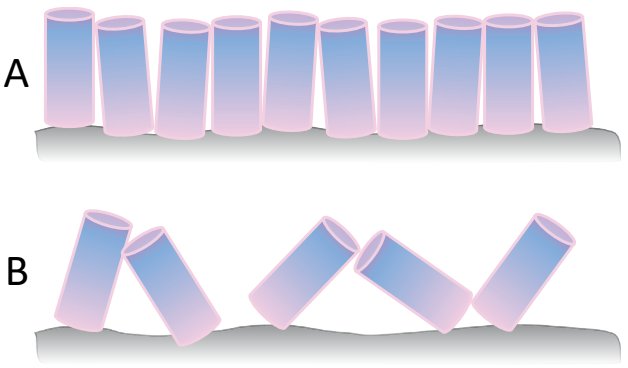

Figure 5.24. Schematic representation of the structure of the remaining fouling layers after the conventional cleaning process (A) and predictive cleaning process (B).

5.3. Conclusions

QCM-D and MP-SPR are capable of providing a fast screening on the cleaning efficiency of detergents both on-line and off-line. Off-line studies of membrane cleaning also revealed that some detergents attack the membrane polymer or even aggravate fouling. On-line monitoring of membrane cleaning is possible despite of the bulk response caused by the detergents. During these bulk changes, QCM-D and MP-SPR maintained their surface sensitivity, but with a perception threshold.

A proof-of-concept study performed for predictive cleaning demonstrated and confirmed that early-stage detection of fouling and resulting optimization of the cleaning strategy can keep fouling at significantly lower levels than during conventional operation.

5.4. References

[1] *S.F. Anis, R. Hashaikeh, N. Hilal, Reverse osmosis pretreatment technologies and future trends: A comprehensive review, Desalination. 452 (2019) 159–195. https://doi.org/10.1016/j.desal.2018.11.006.*

[2] *S. Jiang, Y. Li, B.P. Ladewig, A review of reverse osmosis membrane fouling and control strategies, Sci. Total Environ. 595 (2017) 567–583. https://doi.org/10.1016/j.scitotenv.2017.03.235.*

[3] *Y. Zhou, S. Yu, C. Gao, X. Feng, Surface modification of thin film composite polyamide membranes by electrostatic self deposition of polycations for improved fouling resistance, Sep. Purif. Technol. 66 (2009) 287–294. https://doi.org/10.1016/j.seppur.2008.12.021.*

[4] *D.S. Sholl, J.K. Johnson, Making high-flux membranes with carbon nanotubes, Science (80-.). 312 (2006) 1003–1004. https://doi.org/10.1126/science.1127261.*

[5] *J.S. Vrouwenvelder, J.A.M. van Paassen, J.M.C. van Agtmaal, M.C.M. van Loosdrecht, J.C. Kruithof, A critical flux to avoid biofouling of spiral wound nanofiltration and reverse osmosis membranes: Fact or fiction?, J. Memb. Sci. 326 (2009) 36–44. https://doi.org/10.1016/j.memsci.2008.09.029.*

[6] *Y. Kim, S. Li, N. Ghaffour, Evaluation of different cleaning strategies for different types of forward osmosis membrane fouling and scaling, J. Memb. Sci. 596 (2020) 117731. https://doi.org/10.1016/j.memsci.2019.117731.*

[7] *T. Mohammadi, S.S. Madaeni, M.K. Moghadam, Investigation of membrane fouling, Desalination. 153 (2003) 155–160. https://doi.org/10.1016/S0011-9164(02)01118-9.*

[8] *N.M. D'Souza, A.J. Mawson, Membrane cleaning in the dairy industry: A review, Crit. Rev. Food Sci. Nutr. 45 (2005) 125–134. https://doi.org/10.1080/10408690490911783.*

[9] *W.S. Ang, S. Lee, M. Elimelech, Chemical and physical aspects of cleaning of organic-fouled reverse osmosis membranes, J. Memb. Sci. 272 (2006) 198–210. https://doi.org/10.1016/j.memsci.2005.07.035.*

[10] *W.S. Ang, A. Tiraferri, K.L. Chen, M. Elimelech, Fouling and cleaning of RO membranes fouled by mixtures of organic foulants simulating wastewater effluent, J. Memb. Sci. 376 (2011) 196–206. https://doi.org/10.1016/j.memsci.2011.04.020.*

[11] *W.S. Ang, N.Y. Yip, A. Tiraferri, M. Elimelech, Chemical cleaning of RO membranes fouled by wastewater effluent: Achieving higher efficiency with dual-step cleaning, J. Memb. Sci. 382 (2011) 100–106. https://doi.org/10.1016/j.memsci.2011.07.047.*

[12] Z. Wang, J. Ma, C.Y. Tang, K. Kimura, Q. Wang, X. Han, Membrane cleaning in membrane bioreactors: A review, J. Memb. Sci. 468 (2014) 276–307. https://doi.org/10.1016/j.memsci.2014.05.060.

[13] P.S. Goh, W.J. Lau, M.H.D. Othman, A.F. Ismail, Membrane fouling in desalination and its mitigation strategies, Desalination. 425 (2018) 130–155. https://doi.org/10.1016/j.desal.2017.10.018.

[14] R. Valladares Linares, V. Yangali-Quintanilla, Z. Li, G. Amy, NOM and TEP fouling of a forward osmosis (FO) membrane: Foulant identification and cleaning, J. Memb. Sci. 421–422 (2012) 217–224. https://doi.org/10.1016/j.memsci.2012.07.019.

[15] S.S. Madaeni, S. Samieirad, Chemical cleaning of reverse osmosis membrane fouled by wastewater, Desalination. 257 (2010) 80–86. https://doi.org/10.1016/j.desal.2010.03.002.

[16] S.S. Madaeni, Y. Mansourpanah, Chemical cleaning of reverse osmosis membranes fouled by whey, Desalination. 161 (2004) 13–24. https://doi.org/10.1016/S0011-9164(04)90036-7.

[17] S. Lee, M. Elimelech, Salt cleaning of organic-fouled reverse osmosis membranes, Water Res. 41 (2007) 1134–1142. https://doi.org/10.1016/j.watres.2006.11.043.

[18] I. Reviakine, D. Johannsmann, R.P. Richter, Hearing what you cannot see and visualizing what you hear: Interpreting quartz crystal microbalance data from solvated interfaces, Anal. Chem. 83 (2011) 8838–8848. https://doi.org/10.1021/ac201778h.

[19] T. Fujioka, S.J. Khan, J.A. McDonald, L.D. Nghiem, Rejection of trace organic chemicals by a nanofiltration membrane: The role of molecular properties and effects of caustic cleaning, Environ. Sci. Water Res. Technol. 1 (2015) 846–854. https://doi.org/10.1039/c5ew00170f.

[20] B.M. Jun, H.K. Lee, Y.I. Park, Y.N. Kwon, Degradation of full aromatic polyamide NF membrane by sulfuric acid and hydrogen halides: Change of the surface/permeability properties, Polym. Degrad. Stab. 162 (2019) 1–11. https://doi.org/10.1016/j.polymdegradstab.2019.02.008.

[21] Lanxess, The Water Absorption and Conditioning of Molded Parts in Durethan ®, (2010) 1–14.

[22] J. Huang, J. Luo, X. Chen, S. Feng, Y. Wan, How Do Chemical Cleaning Agents Act on Polyamide Nanofiltration Membrane and Fouling Layer?, Ind. Eng. Chem. Res. 59 (2020) 17653–17670. https://doi.org/10.1021/acs.iecr.0c03365.

[23] D.L. Zhao, S. Japip, Y. Zhang, M. Weber, C. Maletzko, T.S. Chung, Emerging thin-film nanocomposite (TFN) membranes for reverse osmosis: A review, Water Res. 173 (2020) 115557. https://doi.org/10.1016/j.watres.2020.115557.

[24] A. Al Mayyahi, Important approaches to enhance reverse osmosis (RO) thin film composite (TFC) membranes performance, Membranes (Basel). 8 (2018). https://doi.org/10.3390/membranes8030068.

[25] H. Sun, J. Liu, X. Luo, Y. Chen, C. Jiang, Z. Zhai, Q.J. Niu, Fabrication of thin-film composite polyamide nanofiltration membrane based on polyphenol intermediate layer with enhanced desalination performance, Desalination. 488 (2020) 114525. https://doi.org/10.1016/j.desal.2020.114525.

[26] C. Procedures, Technical Service Bulletin, (2014) 1–16.

[27] C. Leroy, C. Delbarre, F. Ghillebaert, C. Compere, D. Combes, Effects of commercial enzymes on the adhesion of a marine biofilm-forming bacterium., Biofouling. 24 (2008) 11–22. https://doi.org/10.1080/08927010701784912.

[28] The QCM fundamental frequency – how it matters in measurements, (n.d.). https://www.biolinscientific.com/blog/does-the-qcm-fundamental-frequency-matter (accessed February 21, 2022).

[29] K.K. Kanazawa, J.G. Gordon, Frequency of a Quartz Microbalance in Contact with Liquid, Anal. Chem. 57 (1985) 1770–1771. https://doi.org/10.1021/ac00285a062.

[30] M. Edvardsson, M. Rodahl, B. Kasemo, F. Höök, A dual-frequency QCM-D setup operating at elevated oscillation amplitudes, Anal. Chem. 77 (2005) 4918–4926. https://doi.org/10.1021/ac050116j.

[31] M. Rodal, How are QCM results influenced by the lateral distribution of the measured layer?, (n.d.). https://www.biolinscientific.com/blog/how-are-qcm-results-influenced-by-the-lateral-distribution-of-the-measured-layer.

[32] G. Ohlsson, Overview Why it is useful to use multiple overtones in QCM measurements, (2020) 1–5.

[33] G. Ohlsson, C. Langhammer, I. Zorić, B. Kasemo, A nanocell for quartz crystal microbalance and quartz crystal microbalance with dissipation-monitoring sensing, Rev. Sci. Instrum. 80 (2009). https://doi.org/10.1063/1.3202207.

[34] H. Nagata, Kazuhiro; Handa, Real-Time Analysis of Biomolecular Interactions, Springer International Publishing, 2000.

CHAPTER 6

REAL-TIME MONITORING OF MEMBRANE FOULING AND CLEANING BY QCM-D FROM LAB TO INDUSTRIAL-SCALE: PROOF OF CONCEPT

6.1. Introduction

Although RO is an efficient desalination technology worldwide applied, its efficiency and economics is strongly affected by membrane fouling which is still one of the major process limitations that the field encounters [1]. The direct consequences of membrane fouling are, on the one hand, an increased energy demand, cleaning frequency and consumption of chemicals, and, on the other, a shortened membrane lifetime leading to higher membrane replacement costs [2]. Research in this field has done great effort in order to understand the underlying fouling mechanisms [for example, 3–7] and attempts have been and are being made to develop monitoring protocols that could help the desalination industry in reducing membrane fouling or detect it at an early-stage.

Different approaches are used in order to detect, control and try to mitigate membrane fouling in industrial desalination plants. Fouling propensity of the feedwater is extensively studied by analysing off-line the water quality entering to RO membranes focussing on different standard parameters such as turbidity, pH or total and dissolved organic carbon (TOC and DOC) [2,8]. The most applied measurement as a standard in this sense is the Silt Density Index (SDI) which consists on filtering the pretreated feedwater by a microfiltration (MF) membrane (with 0,45 μm of pore size) at dead-end configuration under constant pressure. The time needed to filtrate a specific and known volume of feedwater is recorded and a SDI percentage is calculated which must be above 5 [2]. However, SDI indexes may not provide reliable information due to the fact that several foulants have a smaller size than the MWCO of the MF membrane and are consequently not rejected by the MF membrane resulting in underestimating the fouling propensity. Furthermore, as the feed water is a dynamic system which can continuously change its composition, occasional SDI measurements may be of limited value. For this reason, it is essential to use techniques that allow monitoring membrane fouling in real-time and in a non-invasive manner.

In the past decades, different more advanced techniques have been investigated in order to monitor and control membrane fouling. Some of the more commonly reported monitoring methods are direct observation trough membrane (DOTM) [9], electrical impedance spectroscopy [10], laser triangulometry [11], fluorescence spectroscopy [12,13] synchrotron IR spectroscopy [14], optical

coherence tomography (OCT) [15], RAMAN spectroscopy [13,16] and FTIR mapping [17]. These methods are indeed very useful to study membrane fouling and all of them provide valuable insights into fouling mechanisms. However, they are not sensitive enough for detecting fouling in a very early-stage and, hence, anticipative way. In order to achieve this, the detection limit should be as low as starting from the very first adsorption layers that are formed in the range of nanometers, roughly three orders of magnitude lower than the detection limit of common detection techniques. In addition, the industrial implementation of some of the aforementioned techniques is limited as they are not robust enough for enduring the sometimes harsh conditions in industrial desalination plants.

Taking the latter into consideration, this Chapter investigates the implementation of the QCM-D equipment into an RO system.

6.2. Results and Discussion

Once it had been verified that combining both QCM-D and MP-SPR offer a promising membrane fouling monitoring tool, a proof-of-concept study was carried out in order to further investigate if the proposed methods were capable of detecting membrane fouling when connected to an RO unit. This section describes first data obtained from an integration of the QCM-D into a bench-scale RO unit and then an implementation in an industrial-scale RO plant installed in a local

multinational manufacturer from the paper sector (see Chapter 2). In order to simplify the integration, only QCM-D was used. The commercial MP-SPR was particularly sensitive to air bubbles and it needed an in-line degasser which made the connection to the RO plant potentially less robust from an industrial application point of view. However, since it was demonstrated in previous chapters that QCM-D and MP-SPR widely coincided in their capacity of membrane fouling detection, the sole use of QCM-D was considered to be a valid proof-of-concept.

6.2.1. Connection of QCM-D equipment with a lab-scale RO unit

The QCM-D equipment was connected to laboratory RO system (Chapter 2) after the pump in order to warrant a constant flux through the sensor module (Figure 6.1). The RO system operated in a recirculation regime. As a consequence, gradual heating of the feed occurred during operation and along time. The temperature control of the QCM-D was therefore disabled as it was observed that with the installed Peltier trying to maintain the temperature constant (the system was set to a default temperature of 23°C) the system would overheat. Besides, as membrane fouling could possibly be affected by the feed temperature, the monitoring should occur under the same conditions.

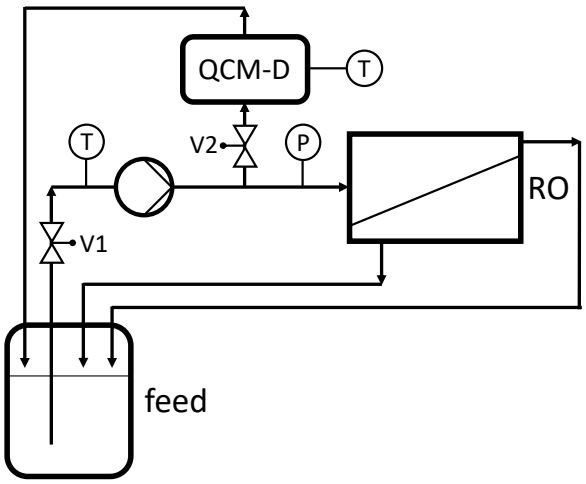

Figure 6.1. Schematic representation of the QCM-D connection to the laboratory RO system. The feed is recirculated via a pump situated after a shut-off valve V1. Retentate and permeate also are returned to the feed tank. The QCM-D was connected via a flow-regulating valve V2 in a bypass mode to the feed line of the RO system and its outflow also returned to the feed. "T" and "P" indicate temperature and pressure measurements, respectively. Other basic technical specifications of the RO system were reported in Chapter 2.

One of the first concerns was to see whether a stable signal could be reached at all when connecting the microfluidic module of QCM-D to the RO system. The water flux that entered the QCM-D module was two orders of magnitude higher than the usual liquid flow applied. In fact, the QCM-D equipment used is designed to operate at low liquid flows (no more than 100 µl/min) and highly controlled and stable laboratory conditions [18]. The operating conditions of the QCM-D where therefore drastically different from experiments reported in previous Chapters.

Indeed, a first trial was unsuccessful due to excessive noise in the signal. Figure 6.2 depicts the change in the frequency and the dissipation measured for two hours and half by QCM-D when connected to the feed stream of the RO system.

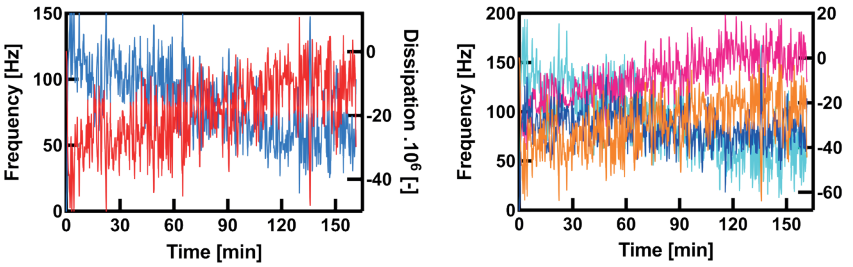

Figure 6.2. Left: Measured change in the frequency (blue) and dissipation (red) for the 5th harmonic when water of RO permeate flowed through a PA-coated QCM-D sensor. Right: measured change in the frequency (turquoise) and dissipation (orange) for the 3rd harmonic; measured change in the frequency (blue) and dissipation (pink) for the 13th harmonic.

As can be observed, the noise in the frequency (ΔF) is around 50 Hz, almost double as high than the change generated by the steady-state adsorption of a model foulant such as BSA protein. In this context, the measured noise was therefore far too high and unacceptable considering that only water was flowing over the PA-coated sensor. The pump of the RO system was identified as the most probable source for the noise. The pump operated at a speed which resulted in a recycling of the whole feed volume in less than a minute. High turbulence could therefore be expected in the feed line which in turn affected the QCM-D signal. QCM-D usually operates at very small Reynolds-numbers (below Re<10).

In order to solve this problem a custom-made flow damper between the RO feed line and QCM-D was installed. As a consequence, the noise in the signal was considerably reduced, as can be seen in Figure 6.3.

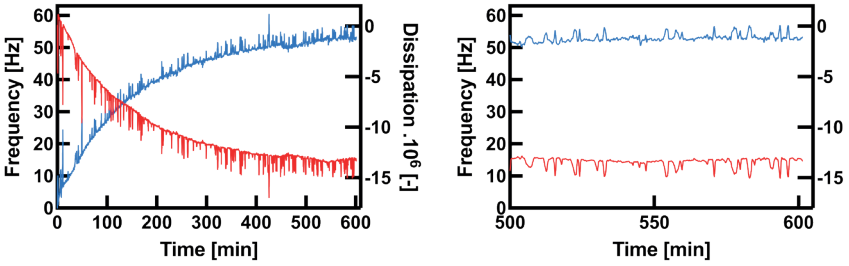

Figure 6.3. Left: Change in the frequency (blue) and dissipation (red) measured for the 5th harmonic due to the contact of RO feedwater with the PA-coated QCM-D sensor after the installation of the custom-made flow damper. The operation time was 10 hours. Right: Amplification of time interval of 10 minutes from the same experiment.

The ΔF obtained for the noise was below 5 Hz which could be considered an acceptable level considering the non-conventional environment to which the QCM-D microfluidic module was subjected.

However, a considerable increase in the frequency of about 55 Hz and corresponding decrease in dissipation occurred during the 10 hours of experimentation as depicted in Figure 6.3 (left). This suggested a partial removal or abrasion of PA deposited on the QCM-D sensor possibly caused by the continuous high water flow coming from the RO feed line. Yet, as Figure 6.4 clearly

demonstrates, the underlying reason was the change of the temperature of the RO feed water.

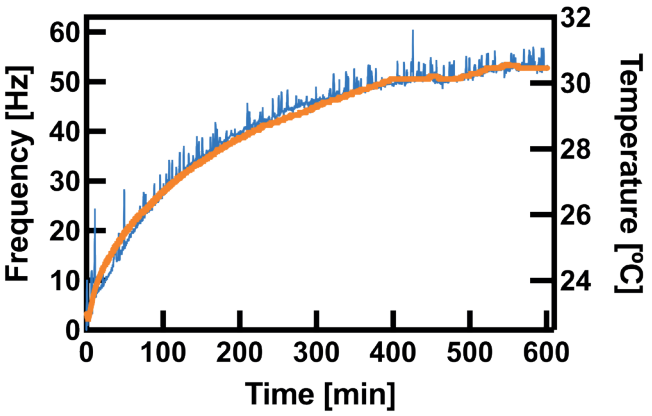

Figure 6.4. Correlation between the measured frequency for the 5th harmonic (blue) and the feed water temperature of the RO (orange).

The frequency increase correlated almost perfectly with the change in of the temperature with a ΔF of about 55 Hz for a ΔT of about 8 °C. The source for this increase in the feed temperature was again the recirculation pump which generated significant heat during operation.

With the aim of being able to disregard the effect of temperature on the measured frequency and therefore be able to obtain a stable baseline as a reference for further fouling experiments, a temperature correction was applied where necessary in subsequent studies. Figure 6.5 (left) illustrates that there existed a linear relationship between the frequency and the feed tempe-

rature. The respective empirical frequency-temperature correlation (Eq. 6.1) allowed to consecutively apply a temperature correction. Figure 6.5 (right) shows that this resulted in diminishing the frequency variation down to less than 5 Hz and that a practically stable signal was achieved.

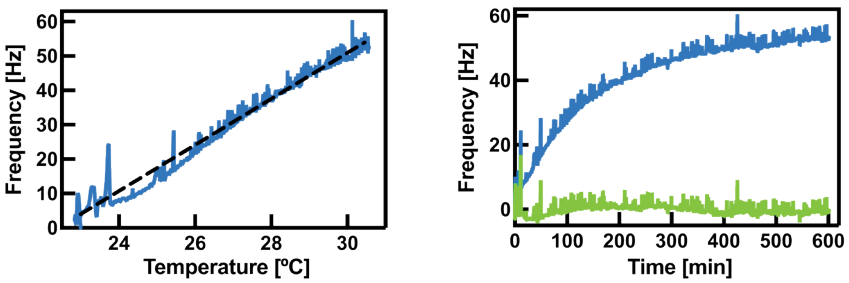

Figure 6.5. Left: Correlation between the measured frequency change for the 5th harmonic (blue) and the temperature of the RO feed. Data were fitted with a linear regression (dashed black line). Right: Original frequency data (blue) and the temperature-corrected frequency (green).

The empirical linear correlation resulted from the fit was

$$F(T)\ [Hz] = 6{,}83[Hz \cdot °C^{-1}] \cdot T[°C] - 154{,}44[\mathrm{Hz}] \qquad \textbf{Equation 6.1}$$

On the other hand, it was observed that when the RO plant had been operated for more than 12 hours, the feed temperature varied only 0,5°C (between 28,9°C and 29,4°C) which did not generate a significant frequency variation within almost 7 hours (Figure 6.6) and was therefore acceptable during following experiments.

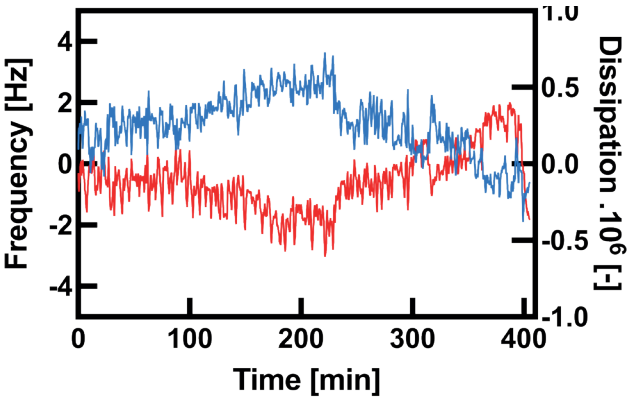

Figure 6.6. Variability of the measured frequency (blue) and dissipation (red) for the 5th harmonic when operating the RO for almost 7 hours. The change in the temperature did not generate a significant instability of the signal in the context of the experiments envisaged.

6.2.2. Proof of concept study: on-line monitoring of the adsorption of a model protein and subsequent cleaning

Once a stable signal was achieved and after proving that the microfluidic QCM-D withheld the high liquid flow over time, a proof of concept study was carried out in order to investigate whether the QCM-D could detect the adsorption of a model foulant on-line. Due to the large feed volume of the RO system, casein protein (CAS) was used as a model foulant instead of BSA because of its significantly lower cost (Chapter 2). For this reason, first off-line measurements with the QCM-D were performed as a reference Figure 6.7 illustrates the initial stabilization of the baseline using PBS buffer, followed by an adsorption of CAS from a solution of 100 ppm (m/m) onto the PA-coated QCM-D sensor surface, a rinsing step with PBS buffer in order to remove reversibly or loosely

bound CAS molecules, a cleaning step using AS2 cleaning detergent as an alkaline cleaning agent (see Chapter 5) and a final rinsing step with PBS buffer. All experimental conditions were identical to those in Chapter 5.

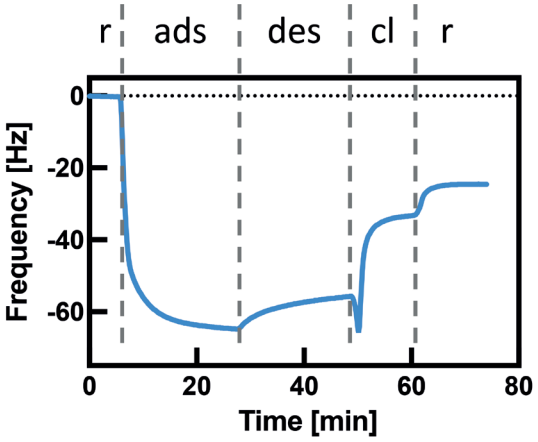

Figure 6.7. CAS adsorption onto PA-coated QCM-D sensor and cleaning; r: reference; ads: adsorption step; des: desorption step under reference conditions; cl: cleaning with detergent AS2; r: flushing under reference conditions.

As can be seen, the overall adsorption of CAS (interval "ads") reached 65 Hz while the irreversible adsorption of CAS on the PA-coated sensor generated a frequency shift of 57 Hz (interval "des") and 24,5 Hz (last interval "r") before and after cleaning, respectively. The calculated cleaning efficiency was 57%.

For on-line measurements, an adequately concentrated CAS stock solution was to be added into the water tank such as to enable rapid mixing. The addition of CAS would require tempo-

rary closing of feed valve V1 (see Figure 6.1) in order to allow for good mixing of feed solution. As this would bring the RO Feed line to a hold, so would the by-pass flow toward the QCM-D. Figure 6.8 shows that upon valve closing (arrow) a sudden frequency decrease of about 35 Hz occurred due to the decrease in flow pressure. However, most importantly, the baseline was recovered afterwards, from which it could concluded that actuating the valve V1 was not limiting the online monitoring.

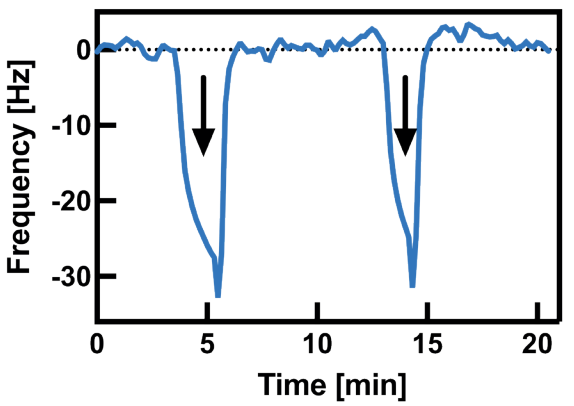

Figure 6.8. Effect of repeated closing/opening the feed valve V1 temporarily (arrow) on the measured QCM-D frequency signal.

Consecutively, an on-line fouling experiment was conducted. An adequately concentrated CAS stock solution was prepared considering both the total volume of the tank and an estimated volume of the liquid circuit such that an approximate final CAS concentration of 100 ppm (m/m) would be obtained.

Figure 6.9 shows raw data of the measured frequency during the on-line measurements of the adsorption of CAS.

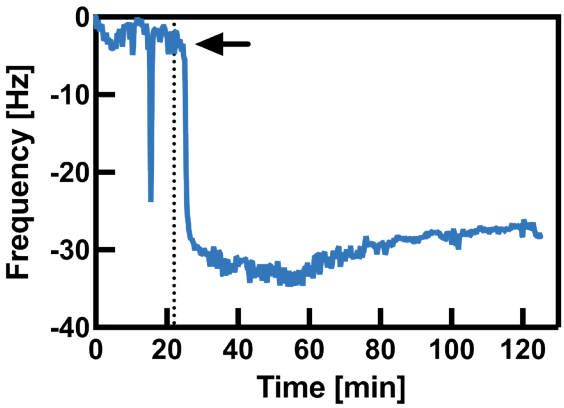

Figure 6.9. Detection by QCM-D of the adsorption of CAS protein (added at the point indicted by arrow and dotted line) in the feed.

As can be observed, shortly after the CAS stock solution had been added to the feed (visible by the short downward peak due to actuation of the valve V1), an adsorption of CAS onto the PA-coated sensor surface was detected. After recirculating the CAS feed solution during about 100 min, the frequency had stabilized at about 28 Hz. The off-line CAS adsorption had yielded about 65 Hz. Thus, QCM-D successfully detected on-line the presence of CAS in the feed but the measured amount adsorbed was 43% of that measured during off-line studies. A possible explanation could be that the total volume of water was underestimated and therefore the final CAS feed concentration was less than 100 ppm (m/m). Additionally, it must be taken into account that although RO membranes were polyamide-based TFC mem-

branes, the polyamide used on the QCM-D sensors and that of the membranes was not identical. It is therefore possible that the CAS adsorbed to slightly different degrees on these both surfaces. For practical applications this would not be a limitation as a simple initial calibration would eliminate this difference.

The recirculation of the CAS feed solution was continued for another 11 hours and concurrently the water permeate flux of the RO unit was measured. As can be seen in Figure 6.10, both the frequency and the permeate flux remained at a stable average value of about 24 Hz and around 1005 g·min^{-1}, respectively, until 8,5 hours.

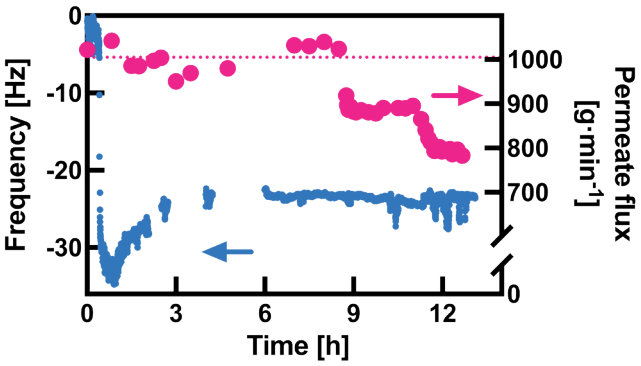

Figure 6.10. Permeate flux measured of RO (pink) and QCM-D frequency data (blue) during a 13 hour-long RO run with CAS fouling.

Only after this period of time, a the permeate flux suddenly decreased in two steps down to 790 g·min^{-1}. Hence, an overall flux decline of about 20% occurred due to the injection of CAS protein into the RO feedwater. There is no obvious explanation for why the permeate flux decreased stepwise. But most important-

ly, as can be seen, QCM-D detected fouling well before permeate flux was apparently affected. This corroborates the early-stage detection of fouling using this system.

On the other hand, frequency remained virtually constant during a subsequent flushing step on a level where the previous experiment had finished (Figure 6.11). Also the permeate flux remained after 15h constant, within a certain degree of variation, at a level equal to the first step decrease at about 11h in Figure 6.10. The second step decrease in Figure 6.10 might therefore not be of chemical origin. In general, QCM-D data and process data agreed satisfactorily.

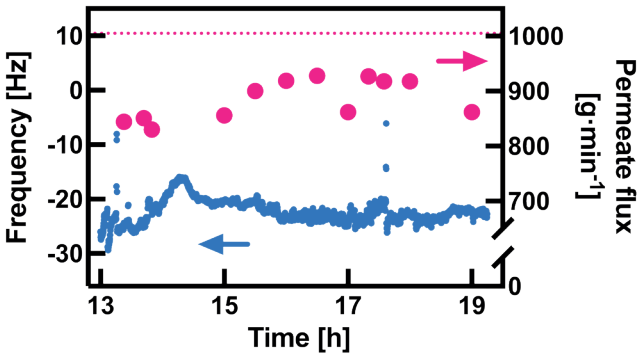

Figure 6.11. Permeate flux measured of RO (pink) and QCM-D frequency data (blue) during another 6 hour-long RO run with water flushing.

Similar to the off-line measurement (Figure 6.7), subsequently an on-line cleaning experiment was performed in order to monitor how the CAS foulant would be removed from the RO membrane surface. The cleaning detergent used in this case was a simple

alkaline solution composed of 0.1% NaOH instead of previously used AS2 which also includes SDS in its formulation (Chapter 2). SDS was not added due to the large feed volume and resulting costs. As is depicted in Figure 6.12, during cleaning step the permeate flux dropped quickly from about 900 g/min to 770 g/min and remained virtually constant at this value. This observation was unexpected because it was anticipated that the cleaning would result in a gradual permeate flux recovery. In fact, as regards the interaction of NaOH with polyamide, it was hypothesized in Chapter 5 (section 5.2.3.1) that NaOH causes a swelling of PA which would result in an increase of the permeate flux. Hence, the reason for the rather constant lower water permeate flux during the cleaning interval remain unclear.

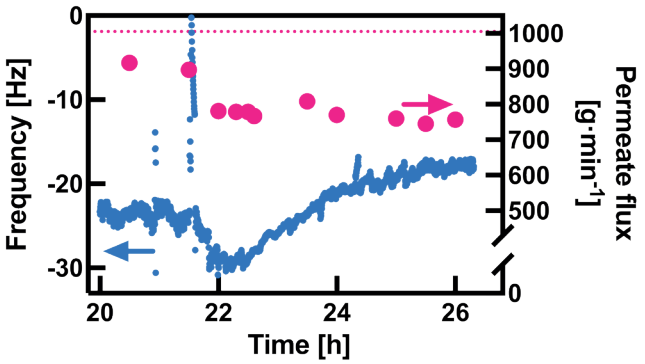

Figure 6.12. Permeate flux measured of RO (pink) and QCM-D frequency data (blue) during 6 hour-long RO run with cleaning with 0.1% NaOH as cleaning detergent.

An important observation is that the response to the NaOH solution had been successfully detected as a change in the QCM-D

signal. As can be seen, the cleaning takes almost 4 hours until reaching steady state. This time was significantly above the time needed in cleaning experiments performed in Chapter 5. Nevertheless, data shown in Figure 6.12 agreed well with those cleaning experiments discussed in Chapter 5 where it was shown off-line that cleaning can be monitored during the bulk response while QCM-D is exposed to the cleaning agent.

The generated bulk signal during cleaning reached in this case about 18 Hz. Hence, it seems from the bulk data that about 6 Hz of 24 Hz CAS irreversible fouling (Figure 6.11) had been removed which would correspond to a cleaning efficiency of only about 25%. However, as was discussed in Chapter 5, during the cleaning cycle the cleaning efficiency is underestimated due to the contribution of the bulk change.

First and foremost, it can clearly be seen how the system was capable of monitoring fouling removal during the cleaning process and determine when exposure to the cleaning agent (here: NaOH) did not have any further effect. This is highly valuable in a process as it allows reducing cleaning times to the absolute necessary. As a consequence, process downtimes and use of cleaning agents can be optimized and membrane life-time will be enhanced to a maximum in view of the general operating conditions.

Finally, after cleaning with 0,1% NaOH solution the RO system was purged with water as a final rinsing step in order to study determine the true cleaning efficiency and in order to verify to what

extent the permeate flux would be recovered after cleaning. For this purpose, the feed solution was changed which required an interruption of the monitoring for about 20 minutes. Figure 6.13 shows the QCM-D monitoring and permeate fluxes after this short break with water flushing through the system in a one-pass mode such as to warrant removal of the NaOH solution.

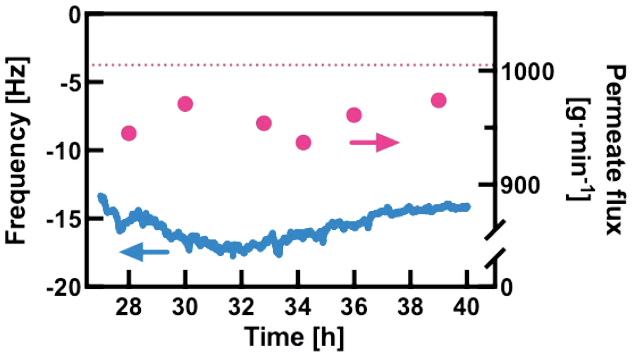

Figure 6.13. Permeate flux measured of RO (pink) and QCM-D frequency data (blue) during about 13 hour-long RO run with rinsing after cleaning with NaOH.

Some variation in both permeate flux and measured frequency could be observed but they were not considered to be significant. This means that the recovery of the permeate flux was almost instantaneous once the NaOH solution had been replaced by water. In fact, permeate flux remained at around 950 g/min which is about 95% of the initial average water flux.

The QCM-D signal remained at about 14 Hz which means that 10 Hz of CAS fouling had been removed from the irreversibly

adsorbed 24 Hz of CAS protein. This corresponded to a cleaning efficiency of about 42%. This value was slightly lower than what was measured off-line (Figure 6.7) but it must be considered that in this case SDS was not present in the cleaning solution. Still, QCM-D data agreed with water permeate flux data: the permeate flux obtained during the rinsing step after CAS adsorption (Figure 6.11) was about 900 g/min, thus being a 10% lower than the initial water flux. The measured frequency was about 24 Hz in these step. During rinsing after cleaning (Figure 6.13), the permeate flux was 5% lower than initial flux while QCM-D gave a frequency of 14 Hz.

6.2.3. Pilot study: Membrane fouling monitoring on an industrial RO plant

A pilot study on a relevant industrial environment was performed in a local multinational manufacturer from the paper sector in collaboration with OTARI Ingeniería del Agua S.L. (Irún, Spain). The principle technical aspects of the industrial RO plant are reported in Chapter 2. The QCM-D microfluidic module was connected using the same configuration as described in Figure 6.1 and the connection was made after the booster pump using additionally a pressure reducer that yielded a final pressure of 1 bar(g). The sensors used were covered with the PA-PEG0 polyamides (Chapter 2) as a membrane model polymer and representative for the RO membranes of the plant.

Figure 6.14 presents the obtained results from the pilot study during an experimentation time of more than one month.

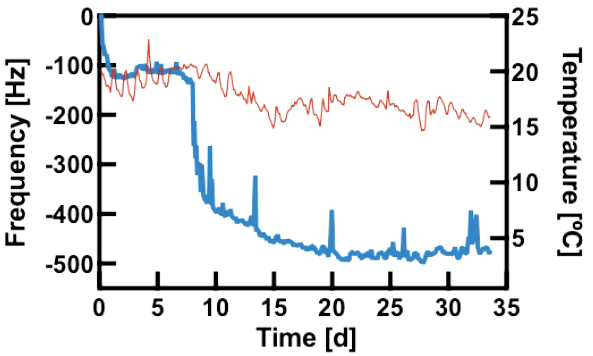

Figure 6.14. QCM-D frequency data (blue) during a pilot study on an industrial RO plant. The duration of the pilot test was of 1 month. The temperature (red) was also monitored during the pilot. Frequency is related to the degree of fouling occurring onto the surface of the RO membrane.

As can be seen, a gradual and clear decrease in the frequency was measured which was indicative for fouling occurring on the RO membranes. The feed water source of the RO system was brackish water which passed through a sand filter prior to the RO. This means that a significant amount of organic foulants should be expected. This is reflected by a frequency shift of 100 Hz reached already during the first day and lasting for the first 7 days of operation. After day 9 an abrupt decrease in the frequency of 300 Hz was observed. After this surprising jump and wondering whether it was a technical problem of the monitoring device or the RO system, the operator of the RO was contacted. He stated that the RO was operating as usual. However, the next

day their permeate flux drastically decreased due to unknown reasons. This corroborated in an industrial environment that the QCM-D can detect at an early stage the fouling of the RO plant and anticipate its detrimental effects.

Figure 6.14 also shows that temperature decreased along the monitoring which would also result in lower frequencies. However, this temperature effect is not enough to explain the measured fouling. In fact, a change of ΔT= -5 °C would result in a frequency change of about ΔF= 30 Hz (Figure 6.5, left) which is far less than the fouling detected.

6.3. Conclusions

The QCM-D microfluidic module was successfully connected to both bench-scale and industrial RO plants. A noise level of the signal was reached which enabled membrane fouling and cleaning monitoring. The experimental set-up allowed a simple plug and play connection to the RO units. QCM-D can therefore be used as a monitoring tool in an industrial environment.

Using a bench-scale RO system, the adsorption of CAS model foulant could be monitored by QCM-D as well as the cleaning step. Cleaning efficiency could be monitored on-line despite of the bulk response of the cleaning agent.

Finally, the successful industrial implementation of the QCM-D equipment opened an opportunity toward the development of

a monitoring device with an hitherto unprecedented sensitivity. Such an early-stage fouling detection device would be expected to contribute, in combination with common conventional analytical techniques, to a more sustainable water production process.

6.4. References

[1] *S. Jiang, Y. Li, B.P. Ladewig, A review of reverse osmosis membrane fouling and control strategies, Sci. Total Environ. 595 (2017) 567–583. https://doi.org/10.1016/j.scitotenv.2017.03.235.*

[2] *L.N. Sim, T.H. Chong, A.H. Taheri, S.T.V. Sim, L. Lai, W.B. Krantz, A.G. Fane, A review of fouling indices and monitoring techniques for reverse osmosis, Desalination. 434 (2018) 169–188. https://doi.org/10.1016/j.desal.2017.12.009.*

[3] *P. Bacchin, D. Si-Hassen, V. Starov, M.J. Clifton, P. Aimar, A unifying model for concentration polarization, gel-layer formation and particle deposition in cross-flow membrane filtration of colloidal suspensions, Chem. Eng. Sci. 57 (2002) 77–91. https://doi.org/10.1016/S0009-2509(01)00316-5.*

[4] *A.G. Pervov, A simplified RO process design based on understanding of fouling mechanisms, Desalination. 126 (1999) 227–247. https://doi.org/10.1016/S0011-9164(99)00179-4.*

[5] *X. Zhu, M. Elimelech, Colloidal fouling of reverse osmosis membranes: Measurements and fouling mechanisms, Environ. Sci. Technol. 31 (1997) 3654–3662. https://doi.org/10.1021/es970400v.*

[6] *J. Kucera, Biofouling of polyamide membranes: Fouling mechanisms, current mitigation and cleaning strategies, and future prospects, Membranes (Basel). 9 (2019). https://doi.org/10.3390/membranes9090111.*

[7] *P. Bacchin, P. Aimar, R.W. Field, Critical and sustainable fluxes: Theory, experiments and applications, J. Memb. Sci. 281 (2006) 42–69. https://doi.org/10.1016/j.memsci.2006.04.014.*

[8] T. Miyoshi, M. Hayashi, K. Shimamura, H. Matsuyama, Important fractions of organic matter causing fouling of seawater reverse osmosis (SWRO) membranes, Desalination. 390 (2016) 72–80. https://doi.org/10.1016/j.desal.2016.03.020.

[9] H. Li, A.G. Fane, H.G.L. Coster, S. Vigneswaran, Direct observation of particle deposition on the membrane surface during crossflow microfiltration, J. Memb. Sci. 149 (1998) 83–97. https://doi.org/10.1016/S0376-7388(98)00181-1.

[10] L. Gaedt, T.C. Chilcott, M. Chan, T. Nantawisarakul, A.G. Fane, H.G.L. Coster, Electrical impedance spectroscopy characterisation of conducting membranes II. Experimental, J. Memb. Sci. 195 (2002) 169–180. https://doi.org/10.1016/S0376-7388(01)00542-7.

[11] J. Altmann, S. Ripperger, Particle deposition and layer formation at the crossflow microfiltration, J. Memb. Sci. 124 (1997) 119–128. https://doi.org/10.1016/S0376-7388(96)00235-9.

[12] G. Wolf, J.G. Crespo, M.A.M. Reis, Optical and spectroscopic methods for biofilm examination and monitoring, Rev. Environ. Sci. Biotechnol. 1 (2002) 227–251. https://doi.org/10.1023/A:1021238630092.

[13] C.F. Galinha, G. Carvalho, C.A.M. Portugal, G. Guglielmi, M.A.M. Reis, J.G. Crespo, Multivariate statistically-based modelling of a membrane bioreactor for wastewater treatment using 2D fluorescence monitoring data, Water Res. 46 (2012) 3623–3636. https://doi.org/10.1016/j.watres.2012.04.010.

[14] M. Xie, W. Luo, S.R. Gray, Synchrotron Fourier transform infrared mapping: A novel approach for membrane fouling characterization, Water Res. 111 (2017) 375–381. https://doi.org/10.1016/j.watres.2017.01.020.

[15] L. Fortunato, A. Qamar, Y. Wang, S. Jeong, T.O. Leiknes, In-situ assessment of biofilm formation in submerged membrane system using optical coherence tomography and computational fluid dynamics, J. Memb. Sci. 521 (2017) 84–94. https://doi.org/10.1016/j.memsci.2016.09.004.

[16] T. Virtanen, S.P. Reinikainen, M. Kögler, M. Mänttäri, T. Viitala, M. Kallioinen, Real-time fouling monitoring with Raman spectroscopy, J. Memb. Sci. 525 (2017) 312–319. https://doi.org/10.1016/j.memsci.2016.12.005.

[17] L. Benavente, C. Coetsier, A. Venault, Y. Chang, C. Causserand, P. Bacchin, P. Aimar, FTIR mapping as a simple and powerful approach to study membrane coating and fouling, J. Memb. Sci. 520 (2016) 477–489. https://doi.org/10.1016/j.memsci.2016.07.061.

[18] QSense Analyzer | QSense | QCM-D, (n.d.). https://www.biolinscientific.com/qsense/instruments/qsense-analyzer#specifications (accessed March 17, 2022).

CHAPTER 7

VALUE PROPOSITION FOR AN EARLY-STAGE FOULING MONITORING DEVICE

Throughout this thesis it has been demonstrated that the combination of both QCM-D and MP-SPR is a strategy to efficiently detect membrane fouling at an early-stage. This chapter analyzes the market need for a monitoring device that helps mitigating membrane fouling and thus potentially increases the RO process efficiency on industrial desalination plants. A perspective of RO-based desalination market will be presented and the implementation of the monitoring device will be critically discussed according to the main lacks and needs of the desalination industry. Finally, the creation of a spin-off company based on this thesis is shortly presented.

7.1. Target market: membrane-based desalination by RO

Desalination of water by RO processes is a well-established market worldwide. Its growth potential is very high due to the fact that water is a basic and essential resource for the development of our society. Growing water scarcity generates a fundamental need to optimize the efficiency of water production and treatment processes [1]. Nowadays 15.906 desalination plants produce 95,37 millions m^3/day [2]. Desalination plants can be classified as large (from 10.000 to 250.000 m^3/day), medium (from 500 to 10.000 m^3/day) and small (from 100 to 500 m^3/day) plants. Large desalination plants comprise a 18% of the total plants worldwide, while medium and small plants represent a 36% and 46%, respectively.

Figure 7.1 shows the geographical distribution of the RO-based desalination market by country as a function of the water volume produced.

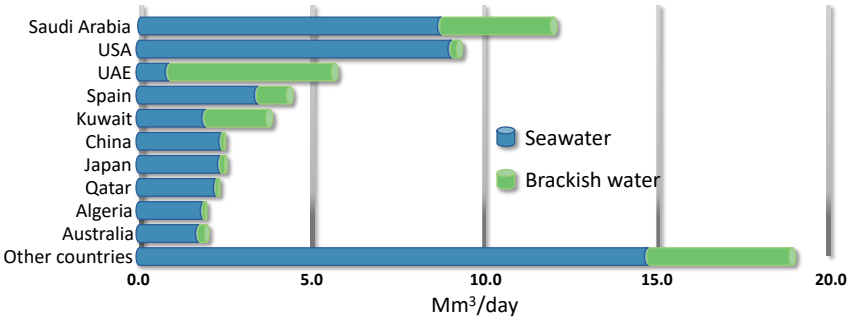

Figure 7.1. Geographical distribution of the desalination market based on RO process [3].

Spain is the fourth largest producer of desalinated water worldwide after the Middle East and USA. It ranks first in European as it manages all the phases of the integral water cycle, including membrane-based water treatment [4]. Moreover, 7 of the 20 largest desalination companies in the world are Spanish and most of them are linked to large construction business groups such as ACCIONA, Ferrovial, FCC and Sacyr, all of which build and manage desalination facilities.

In Spain there are more than 750 desalination plants with a maximum production capacity of 5 million of m^3/day. 13% of the plants are considered large plants (from 10.000 to 250.000 m^3/day), 68% medium-sized plants (from 500 to 10.000 m^3/day) and 32% small plants (from 100 to 500 m^3/day). Currently, the actual production amounts to 3 million of m^3/day. 80% of these production is shouldered by only 50 plants distributed throughout the Mediterranean arc and the Canary Islands. [4].

7.1.1. Evolution of the desalination market and trends

Water treatment industry is growing at an annual rate of 15.3% and the market size reached 6.780 M US$ in 2020. In the case of membrane-based desalination, this growth is explained by fact that water scarcity is continuously increasing [5]. Therefore, there is a strong need to build new plants to increase the production of drinking water.

The growth potential of the desalination market for human consumption is high, especially in those regions which are sensitive to desertification processes as well as in regions where due to

a rapid population growth, in a very few years, the capacity to supply drinking water by natural resources will not be enough.

In the Middle East, where the population is increasing annually up to 8% in some regions [6], intense activity in the construction of new desalination plants is expected in countries such as Saudi Arabia, Oman, the United Arab Emirates and Qatar. On the other hand, in Latin America, specifically in Chile, the total investments in water infrastructure calculated for the next 11 years is estimated to be 1,169 M US$, of which a 62% will be used for the production and distribution of drinking water [7,8]. Another growing market is India where the approximate size of the water market is 3.500 M US$ [9].

Figure 7.2 depicts the growth forecasts for the desalination market at a global level from the year 2000 to 2030. The data are based on the annual production capacity of desalinated water.

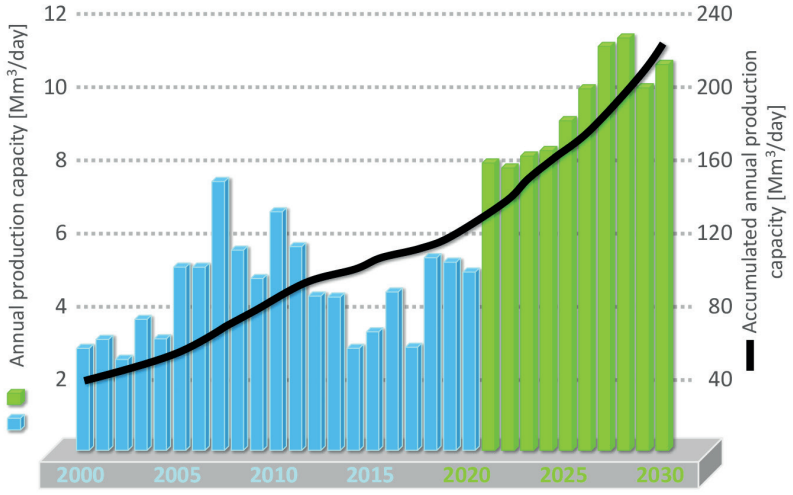

Figure 7.2. Annual growth of desalination market based on the annual production capacity from the year 2000 to 2030.

Planned investments into the desalination market mainly focus on optimizing the operation of existing desalination plants in order to reduce the costs associated to water production and making the desalination process more environmentally friendly [10]. On the other hand, the European legislation regarding the water treatment for discharge and reuse is becoming more and more strict [11,12]. Thus, an exponential growth of new small and medium-sized water treatment facilities which include RO processes can be expected.

7.2. Feedback from the desalination industry

Membrane fouling can seriously affect membrane filtration processes. As fouling cannot be completely avoided, focus lies on optimizing membrane cleaning strategies in order to lengthen membrane lifetime and reduce process downtimes and cleaning-costs. For this purpose, it is crucial to detect membrane fouling at an early-stage. As described in previous Chapters, several methods have been proposed for membrane fouling detection but until today none has proven to be sensitive enough to handle membrane fouling in an anticipative way. In fact, nowadays the fouling is detected in a fairly conventional way: either by a significant drop in the filtered water flux or an increase of the transmembrane pressure (TMP). At this point, the degree of membrane fouling is so high that membranes must be cleaned using protocols which in most cases are based on aggressive chemical detergents. As a consequence of those cleaning protocols, process downtimes are prolonged and

the amount of harmful cleaning agents used increases considerably, which in turns accelerates the membrane deterioration due to the repeated chemical abrasion during cleaning cycles. Therefore, early-stage membrane fouling detection seems to be highly desirable as it would allow reducing these negative effects. Yet, in order to understad the real needs of the industry regarding membrane fouling, interviews were conducted with desalination companies.

7.3. Summary of interviews with desalination plant operators

Four out of the seven most important Spanish desalination companies were interviewed. These interviews were carried out under confidentiallity agreement which is why the names of the companies will be not mentioned. The goal of this section is to describe the feedback obtained from the companies interviewed regarding the relevance of fouling, current applied methods to detect fouling and the needs that a more advanced monitoring device should fulfill in order to be attractive enough to consider its implementation and/or commecialization.

All the interviews revealed that until today operators lack a method sufficiently sensitive for monitoring and predicting critical levels of membrane fouling. All companies claimed that in fact there is a strong need to detect membrane fouling early enough in order to optimize membrane cleaning cycles, increase membrane durability and improve the process performance in terms of efficiency and sustainability.

7.3.1. The relevance of membrane fouling from a process point of view

All the companies agreed that membrane fouling is an undesirable phenomenon which results in frequent membrane cleaning procedures and in the most serious cases in membrane replacement. It was stated that although membrane fouling is a problem of highly variable caracteristics, the quality of the water feeding into the RO is key to the extent of the fouling problem. Indeed, the cleaning costs were reported to be directly related to the initial water quality and resulting the degree of fouling.

Company 1 stated that in general water quality in Europe is of a high standard. Across its plants located in Europe the pretreatment step is usually efficient enough to mitigate fouling thus causing lower membrane cleaning and replacement costs. They revealed that severe fouling mainly occurs in plants located outside Europe, especially in those countries of Latin America and Asia where the water sources are of poorer quality. As an example they mentioned a water treatment plant located in the Philippines where membrane cleaning is performed biweekly resulting in cleaning costs of around a hundred thousand euros per month.

All companies agreed that membrane fouling clearly has a seasonal behaviour. Company 3 suffered most from this: during the winter season, some of their RO plants do not need cleaning for two months. In this situation their cleaning costs are the 3% of the total water production costs which they stated range from 0,2

to 0,6 €/(m^3 produced water). However, these costs soar during the summer season due to the need of a weekly cleaning of the membranes. This confirms that water composition and quality is decisive for how fouling develops. During the summer season, they have tested many different cleaning detergents to fight membrane fouling but unfortunately the water flux was never successfully recovered. This confirms our laboratory data presented in Chapter 5. This company uses up to 100 kg of chemical products for membrane cleaning to make between 15 and 20 cleaning procedures per RO rack in one year. Therefore, they are interested on reducing the generated residues as nowadays the focus is to move towards a circular economy.

Company 4 mentioned that one of their most common problem is membrane scaling caused by some salts such as aluminum silicate. The inability of detecting these compounds results on a membrane disabled to operate correctly. In this sense, they considered an on-line monitoring device to be very useful.

7.3.2. Current applied strategy to deal with membrane fouling in the industry

All the companies interviewed determine when the membranes should be cleaned using in-line presure sensors in order to detect pressure drops in the system. When this pressure drop reaches a preset value, the membrane is cleaned.

From the point of view of Company 2, the most negative effect of membrane fouling may be the increase in the energy consumption that occurs prior to membrane cleaning as the pumps work harder to maintain the transmembrane pressure. In some cases they clean the membranes preventively before the pressure drops. They reckon that pressure-drop measurements are very conventional and rudimentary as they are not capable of predicting membrane fouling in an effective way. Therefore, Company 2 stated that it would be very beneficial to have a monitoring device that allows monitoring fouling in advance in order to prolong membrane cleaning intervals.

All companies claimed that nowadays the most applied method to deal with membrane fouling is the corrective method (Figure 7.3). The latter means that fouling is detected by measuring changes in the filtered water flux (a common limit is a decrease of around 15%) or by measuring pressure drops. However, at this stage process efficiency is already detrimentally affected and membrane fouling has already developed to a stage that it will be more difficult to completely recover the membrane surface after the cleaning step.

Some companies are trying to apply preventive methods based on the knowledge they have about the process. They continuously measure different parameters related to feed water quality (temperature, pH, conductivity, TOC and DOC) and correlate them with membrane fouling using a plant management software (Figure 7.3). The main limitation of this type of solutions is that the

water parameters measured may not be representative for what how fouling will develop on the membrane. All of these methods are based on indirect measurements in water although it would be essential to measure directly on the membrane surface.

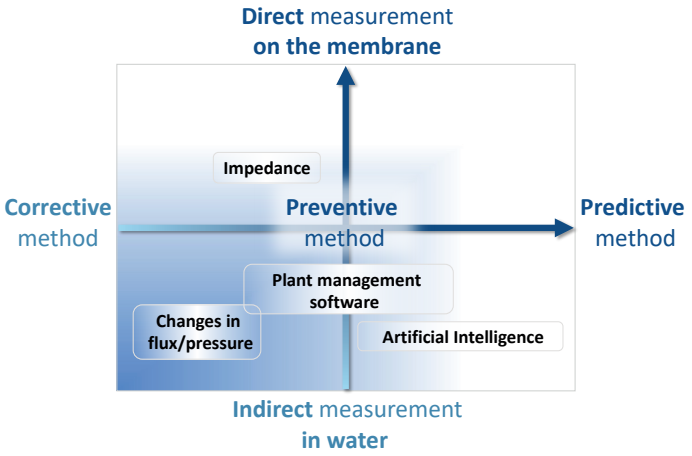

Figure 7.3. Industrial trends regarding the existing methods for detecting membrane fouling and the Gartner´s magic cuadrant (upper right) where new technologies should focus on.

One commercially more advanced technique seems to be spectroscopic impedance [8,9] but its industrial implementation does not seem to be straightforward and very limited today.

As for predictive methods, artificial intelligence (AI) is increasingly used in order to maximize plant efficiency and possibly forecast fouling detection by feeding different process parameters into an optimization algorithm. As data used in AI systems are based on indirect measurements in the feed water, and tak-

ing into account that the composition of feedwater could suddenly change, even these more advanced predictive methods are prone to fail. Thus, Gartner´s magic quadrant in Figure 7.3 is defined by being able to measure fouling on the membrane surface where it actually occurs, and by using a system sensitive enough to allow a high-confidence prediction of damaging fouling levels.

7.3.3. Needs which the fouling monitoring device should fulfill

The companies showed great interest when they were proposed to install a new sensoric device in their plants that monitors and detects fouling at early-stage. However, they made recommendations that were carefully to be taken into account before starting to design the mentioned device and implement it on an industrial scale.

First, as for the economic aspect, the savings provided by the device should exceed the investment in a reasonable period of time (2-3 years). Second, the device should be easy to use because some RO plants are already maintenance-intensive such that plant operators do not wish to increase this burden even further. Specifically Company 4 mentioned that the device could eliminate operation variability due to the human factor which they had determined to be the reason why similar facilities can run differently. Third, the device should be integrable into plant management as all companies were very interested on completely automating their desalination plants in the future.

The only critical comment received was from Company 1 who was afraid of losing the membrane warranty established by membrane manufacturers as they are the ones who recommend when and how the cleaning protocols should be carried out.

7.4. Toward a QCM-D/MP-SPR based fouling monitoring

Based on the results of this thesis and feedback from industry, a minimum viable product (MVP) of a fouling monitoring device was designed to solves the lack of sensitivity on detecting early-stage fouling by combining a surface-sensitive sensor system with ultra-thin membrane material films. The device is connected by a by-pass configuration to the feed-water inlet (“1”, Figure 7.4) such that it does not interfere with the process and can be easily installed also in existing plants. Using a by-pass configuration, it is warranted that the device is exposed at any time to the same feed water as the RO process, including during the cleaning cycles. In this way, it truly mimics the fate of membranes along their lifetime.

Data are acquired and sent by 2G/3G to a cloud where they are processed (“3”, Figure 7.4) and correlated with data provided by the plant operator, e.g. from pressure sensors. After an initial data training, operators of the RO plant can in this way receive an anticipative alarm when critical fouling conditions are approaching.

Figure 7.4. Schematic of the instalation and concept of the fouling monitoring device. 1: RO unit; 2: monitoring sensorial device (schematic); 3: software for data acquisition and visualization.

7.5. Spin-off SURPHASE

The entrepreneurial idea of producing a commercial fouling monitoring device dates back to 2016 when a Proof-of-Concept Grant of the European Research Council validated the general technical viability of the concept. Based on the research conducted during this thesis, SURPHASE, a spin-off of the University of the Basque Country (UPV/EHU) and the Basque Excellence Research Centre for Macromolecular Design and Engineering (POLYMAT) was founded (initially under the name INGENIOUS MEMBRANES S.L.) in 2018. In 2020, the company was selected by the Spanish NEOTEC programme of the National Centre for

Technical and Industrial Development (CDTI, Spain) for funding. This programme generously finances the creation of technology-based companies. The funding obtained was crucial for the design and fabrication of the first prototypes of the device and also allowed the incorporation of two more staff. In 2021, a business angel from the agri-food sector joined the company as a business partner which made it possible to produce a number of devices for the first industrial field tests.

Currently, an industrial test (TRL 9) is so far successfully being conducted in one of the biggest desalination plants of Spain located in the South of the country.

7.6. References

[1] *N.C. Darre, G.S. Toor, Desalination of Water : a Review, (2018) 104–111.*

[2] *E. Jones, M. Qadir, M.T.H. van Vliet, V. Smakhtin, S. mu Kang, The state of desalination and brine production: A global outlook, Sci. Total Environ. 657 (2019) 1343–1356. https://doi.org/10.1016/j.scitotenv.2018.12.076.*

[3] *M. Nair, D. Kumar, Water desalination and challenges: The Middle East perspective: A review, Desalin. Water Treat. 51 (2013) 2030–2040. https://doi.org/10.1080/19443994.2013.734483.*

[4] *Cifras de desalación en España - Aedyr, 1. Cifras Desalación En España - Aedyr. Available Https//Aedyr.Com/Cifras-Desalacion-Espana/. (Accessed 26th December 2021). (n.d.). https://aedyr.com/cifras-desalacion-espana/ (accessed December 26, 2021).*

[5] *S.F. Anis, R. Hashaikeh, N. Hilal, Reverse osmosis pretreatment technologies and future trends: A comprehensive review, Desalination. 452 (2019) 159–195. https://doi.org/10.1016/j.desal.2018.11.006.*

[6] *R. Lee, The outlook for population growth, Science (80-.). 333 (2011) 569–573. https://doi.org/10.1126/science.1208859.*

[7] *S. Herrera-León, C. Cruz, A. Kraslawski, L.A. Cisternas, Current situation and major challenges of desalination in chile, Desalin. Water Treat. 171 (2019) 93–104. https://doi.org/10.5004/dwt.2019.24863.*

[8] *A. Saavedra, H. Valdés, A. Mahn, O. Acosta, Comparative analysis of conventional and emerging technologies for seawater desalination: Northern chile as a case study, Membranes (Basel). 11 (2021). https://doi.org/10.3390/membranes11030180.*

[9] *U. Caldera, C. Breyer, Learning Curve for Seawater Reverse Osmosis Desalination Plants: Capital Cost Trend of the Past, Present, and Future, Water Resour. Res. 53 (2017) 10523–10538. https://doi.org/10.1002/2017WR021402.*

[10] *F. Berenguel-felices, A. Lara-galera, Requirements for the Construction of New Desalination Plants into a Framework of Sustainability, (2020).*

[11] *R. Of, T.H.E. European, O.F.T.H.E. Council, Minimum requirement for water reuse, Eur. Commision. 0169 (2018) 1689–1699.*

[12] *Country profiles on urban waste water treatment, (n.d.). https://water.europa.eu/freshwater/countries/uwwt (accessed March 8, 2022).*

[13] *M.T. Darestani, T.C. Chilcott, H.G.L. Coster, Electrical impedance spectroscopy study of piezoelectric PVDF membranes, J. Solid State Electrochem. 18 (2014) 595–605. https://doi.org/10.1007/s10008-013-2286-x.*

[14] *CMS Innovations – Water Treatment Plant Optimisation Specialists, (n.d.). http://cmsinnovations.com/ (accessed March 8, 2022).*

CHAPTER 8

GENERAL CONCLUSIONS AND OUTLOOK

The main propose of this thesis was to demonstrate that QCM-D and MP-SPR are complementary and feasible techniques for characterizing the build-up of the very first fouling layers at the nanoscale, and that their combination is a powerful and disruptive monitoring tool capable of detecting membrane fouling at an early-stage.

Considering the general objective of this thesis, the following main conclusions can be drawn:

1. The combination of QCM-D and MP-SPR allowed measuring the adsorption of BSA on PA-PEG membrane polymers accurately and data obtained could be correlated with fouling phenomena in the respective filtration process.

2. Although fouling layer thickness can be obtained by both techniques, multiple wavelength MP-SPR provided more reliable results than QCM-D.
3. QCM-D and MP-SPR are complementary for measuring and elucidating the adsorption of common foulants such as BSA, ALG and HA on a PA membrane polymer model.
4. Although the dissipation parameter of QCM-D provides useful information on the viscoelasticity of the adsorbed layers which can subsequently be correlated with the density of the membrane fouling layer, experimental data of dissipation for the adsorption of BSA, ALG and HA on the aromatic PA-coated sensors did not reveal any significant information. MP-SPR/QCM-D mass ratios were more meaningful in this sense.
5. QCM-D and MP-SPR are fast screening techniques for elucidating the cleaning efficiency of different detergents. They yielded also information on whether detergents damaged the PA membrane model polymer.
6. A proof-of-concept study performed for predictive cleaning demonstrated and confirmed that early-stage detection of fouling and resulting optimization of the cleaning strategy can keep fouling at significantly lower levels than during conventional operation.

7. The QCM-D microfluidic module was successfully connected to both bench-scale and industrial RO plants, demonstrating that it can be used as a monitoring tool in an industrial environment.
8. Using a bench-scale RO system, the adsorption of CAS model foulant could be monitored by QCM-D as well as the cleaning step. Cleaning efficiency could be monitored on-line despite of the bulk response of the cleaning agent.
9. The successful industrial implementation of the QCM-D equipment opened an opportunity toward the development of a monitoring device with a hitherto unprecedented sensitivity.
10. During this thesis and based on the results presented, the spin-off company SURPHASE was founded and a minimum viable product (MVP) of a membrane fouling monitoring device produced. The prototype is currently operating in one of the biggest Spanish desalination plants.

As an outlook and future work, the studies presented in this thesis will continue to be deepened in order to optimize the design and operation of the monitoring device with the ultimate goal of commercializing it and achieving a consolidation in the RO-based desalination market.